universiteit hasselt
KNOWLEDGE IN ACTION

2015 | Faculty of Sciences

DOCTORAL DISSERTATION

Exploration of graphene addition and boron doped nanocrystalline diamond transparent electrodes for charge transport enhancement in polymer-based solar cells and light emitting diodes

Doctoral dissertation submitted to obtain the degree of
Doctor of Science: Physics, to be defended by

Pieter Robaeys

Promoter: Prof. Dr Milos Nesladek
Co-promoter: Prof. Dr Jean V. Manca

D/2015/2451/12

universiteit hasselt | imec
IMO - IMOMEC
INSTITUUT VOOR MATERIAALONDERZOEK

Chairman	Prof. Dr. Karin Coninx, UHasselt
Promoter	Prof. Dr Milos Nesladek, UHasselt
Copromoter	Prof. Dr. Jean V. Manca, UHasselt
Members of the jury	Prof. Dr. Hans-Gerhard Boyen, UHasselt
	Prof. dr. Ken Haenen, UHasselt
	Prof. dr. Wim Deferme, UHasselt
	Prof. dr. Etienne Goovaerts, Universiteit Antwerpen
	Dr. Emilie Bourgeois, UHasselt/IMO-IMOMEC
	Dr. Laurence Lutsen, UHasselt/IMO-IMOMEC
	Prof. dr. Ladislav Kavan, Heyrovsky Institute, Czech Academy of Science of Prague, Czech Republic

Dankwoord

Als de nacht gevallen is overvliegt de uil de dag

Een mens, een filosoof, een wetenschapper is als die uil

Hij overdenkt wat er is gebeurd, misschien de afgelopen dag, of net iets langer geleden

Het is eindelijk zover, ik leg mijn doctoraat af! Graag wil ik van de gelegenheid gebruik maken om iedereen te danken die heeft bijgedragen tot dit werk!

Allereerst wil ik mijn promotor, Prof. Dr. Milos Nesladek, bedanken. Beste Milos, bedankt om me 4 jaar geleden aan te hebben genomen om in deze mooie uitdaging mee te groeien. Ook bedankt om bij tijd en stond klaar te staan voor vragen en problemen te bespreken. Je hebt me de vrijheid gegeven om zelf op verkenning te gaan, eigen ideeën te creëren, en hier heb ik ontzettend veel uit geleerd. Bedankt voor alle kansen die ik gekregen heb.

Als tweede wil ik, Prof. Dr. Jean V. Manca bedanken. Beste Jean, door jou ben ik in deze wonderbaarlijke wereld van organische elektronica getrokken. U heeft me altijd gestimuleerd om verder te doen. Het is een eer om u nu als jurylid in mijn jury te mogen terugzien. Ook Wim Deferme en Koen Gilissen wil ik graag bedanken voor hun enthousiasme en doorzetting om onze ontwikkelde electroden in OLED toepassingen te gebruiken.

Ook heel veel dank aan de andere leden van de beoordelingscommissie, Prof. Dr. Ken Haenen, Prof. Dr. Hansgerd Boyen, Dr. Emilie Bourgeois, Dr. Laurance Lutsen, Prof. Dr. Etienne Govaerts en Prof. Dr. Ladislav Kavan voor het beoordelen van mijn proefschrift.

Dank je wel aan alle collega's in het Instituut voor Materiaal Onderzoek, en het allermeest aan de mensen van de "Wide Bandgap Material Group" en de "Organic Nano-Electronics Group". Jullie hebben er een leuke en stimulerende werkomgeving van gemaakt. Allereerst wil ik de oude garde met Wouter Moons, Koen Vandewal, Ludwig Goris en Sabine Berto, bedanken om mij te introduceren in de praktische eigenschappen van organische zonnecellen. Ook Donato Spoltore en Fortunato Piersimoni wil ik bedanken voor de discussies over de werkingsmechanismen in zonnecellen. Bert Conings en Stoffel Jannsen wil ik graag bedanken voor de kritische blik op resultaten en de stimulans om modellen op te zetten om de resultaten in te situeren. Tim Vangerven wil ik graag bedanken voor het steeds terugkerende enthousiasme dat je op het hele labo doet neerstralen. Jeroen Drijkoningen wil ik bedanken voor de simulaties van de zonnecel karakteristieken en Wouter Dierckx wil ik bedanken voor de introductie tot de OFET structuren. Ook Jeroen Strykers en Glen Vandevenne wil ik bedanken om me de mogelijkheden voor het printen van elektronica te laten zien. Tim Cluckers en Michael Daenen wil ik bedanken voor het tonen van de mogelijkheden van warmtetransporten in diamantlagen.

In addition, I would like to especially thank Matthew McDonald for the growth of diamond layers which were used as transparent electrodes. I want to thank also Wim Dexters for AFM characterisation and Sien and Wiebke for helpful input on the possibilities of diamond growth with a variety of dopants. I want to thank Farnoosh and Yaso for introducing me to the world of photolithography, and Quang for the introduction of deposition of boron nitride. I also want to thank Rajesh for the inspiring new diamond applications and Paulius for the introduction to Aluminum Nitride and diamond interactions with other materials.

Ik wil hiernaast ook Christel en Hilde bedanken voor de technische labo ondersteuningen en de goede zorgen over de labo-regulaties en het goede sturen van de aankopen. Johnny, ik wil u bedanken voor het maken van ontwerpen voor diverse sample houders en het mogelijk maken van allerhande metingen. Jan en Lieven wil ik ook heel graag bedanken voor de elektronische bijstand. Jan d'Haen en Bart Ruttens wil ik bedanken voor het maken van heel mooie SEM en TEM beeldjes.

Hiernaast zou ik ook alle medewerkers van het secretariaat willen bedanken voor het regelen van de administratie die het praktische werk in het labo mogelijk gemaakt hebben.

I also want to thank Prof. Dr. Francesco Bonacorso and Prof. Dr. Andrea Ferrari of Cambridge University for the help in preparation of graphene solutions which were used to study the graphene-polymer composites described in this work.

Wouter, Pière en Matthi, bedankt voor de nodige ontspanning tijdens onze eerste doctoraatsjaren in ons huisje in Hasselt. Het was een fijne tijd die we daar beleefd hebben.

I also want to thank our 'Lunch Club' Wiebke, Illaria, Farnoosh, Emilie, Matthew, Philip and Elena for the nice times we had during lunch and during the ice-cream shop visits.

Ook zou ik mijn familie willen bedanken voor de ondersteuning die dit werk heeft mogelijk gemaakt. Ik hoop dat jullie nu een beetje een beeld hebben gekregen van wat ik de laatste jaren allemaal gedaan heb. Ook wil ik mijn liefste ouders bedanken. Woorden schieten te kort voor het beschrijven van de onvoorwaardelijke steun die jullie mij sinds mijn jeugd gegeven hebben.

Ten slotte wil ik mijn lieve vriendinnetje Isabelle bedanken voor het ondersteunen van mijn werk door dik en dun. De juiste tegenbalans te brengen tussen mijn werk en ontspanning, wat zeker noodzakelijk was om deze thesis tot een mooi resultaat te brengen.

Table of Contents

Nederlandse samenvatting

Organische zonnecellen vormen een opkomende technologie in het domein van fotovoltaïsche energie-conversie en onderscheiden zich van klassieke Silicium-zonnecellen door o.a. volgende kenmerken: mechanische flexibiliteit ('plooibare' zonnecellen), esthetische mogelijkheden (vrijheid van vormgeving en kleur), betere respons bij indoor verlichting en diffuus licht (interessant voor indoor energievoorziening voor mobiele elektronische applicaties) en eenvoudige, low-cost verwerkingsmogelijkheden (e.g. printbare zonnecellen). Deze unieke eigenschappen maken organische zonnecellen interessant voor bepaalde niche-applicaties (vb. BIPV-Building Integrated Photovoltaics). Tot nog toe zijn er slechts enkele commerciële toepassingen verschenen en is een commerciële doorbraak van specifieke niche-applicaties nog niet aan de orde omwille van de relatief lage efficiëntie en stabiliteit. Wereldwijd wordt er dan ook veel onderzoek verricht naar het verhogen van de efficiëntie en levensduur en de ontwikkeling van groene en robuuste productieprocessen. Bij organische zonnecellen bestaat de actieve laag doorgaans uit twee type organische materialen en wordt voor de transparante elektrode gebruik gemaakt van het relatief dure en schaarse Indium Tin Oxide (ITO). De innovatieve routes die in dit werk geëxploreerd worden zijn : (I) het gebruik van grafeen als 3de component in de foto-actieve laag en (II) het gebruik van diamant als elektrode-materiaal ter vervanging van ITO.

De bijhorende onderzoeksvragen zijn:

a) *Wat zijn de effecten van grafeen in dunne polymer:fullereen zonnecellen wanneer grafeen gebruikt is als ternaire component in de actieve laag bij dichtheden onder de percolatiedichtheid?*
b) *Is het mogelijk om een transparante elektrode te maken gebaseerd op diamant om Indium tin oxide (ITO) te vervangen en wat zijn de fysische karakteristieken van deze diamant elektrode? Is het mogelijk om deze diamant gebaseerde elektrodes te gebruiken in Polymeer Licht Emitterende Dioden (PLED) en Organische Fotovoltaïsche (OPV) cellen?*

Grafeen als derde component in donor:acceptor organische zonnecel

In organische zonnecellen maakt men doorgaans gebruik van een combinatie van twee materialen in de foto-actieve laag: een donor materiaal (bv. geconjugeerd polymeer) en een acceptor materiaal (bv. een fullereen derivaat). In dit werk wordt de invloed onderzocht van een derde component: grafeen. In het bijzonder is het effect van grafeen op de regulatie van het transport in de actieve laag bestudeerd.

In hoofdstuk 2 hebben we de drempelconcentratie voor grafeen in dunne film polymeer zonnecellen opgespoord en hebben we de effecten van grafeen onder deze concentratie onderzocht. Wanneer grafeen toegevoegd wordt boven de drempel concentratie, beginnen de grafeen blaadjes te klusteren. Dit verhoogt donker lekstromen welke een verminderde device werking induceert. Licht-geïnduceerde lekstromen zijn minder prominent aanwezig in deze studie. Dit is door het feit dat de PEDOT:PSS lagen niet betrokken zijn in de oorsprong van de lekstromen. De toevoeging van lage grafeenconcentratie in P3HT:PCBM

zonnecellen induceert een elektron- en holtetransport met gebalanceerde mobiliteiten. Dit resulteert in een efficiëntere ladingsextractie van de fotogegenereerde ladingen uit de preparaten. De verminderde elektronenmobiliteit is waarschijnlijk te wijten aan het grafeen dat werkt als een 'elektron trapping center'. De verhoogde holtemobiliteit is verkregen door verbetering van de P3HT kristalliniteit na grafeen toevoeging. Deze twee effecten resulteren in een lagere samengestelde ladingsmobiliteit terwijl de elektron- en holtemobiliteit beter uitgebalanceerd zijn. Dit resulteert op zijn beurt in een efficiëntere ladingsextractie en uiteindelijk in efficiëntere zonnecellen.

BNCD:Cr/Au als transparante electrode voor organische elektronische toepassingen

Een belangrijke uitdaging voor toekomstige opto-elektronische applicaties is het vervangen van het dure en schaarse ITO door nieuwe hoog stabiele en transparante electroden. In hoofdstuk 3 is een alternatief ontwikkeld waarbij een goud-netwerk werd geïncorporeerd in transparante Boron gedopeerde nanokristallijne diamant (BNCD)-lagen. Hierbij werd gebruik gemaakt van lithografie, metaalafzettingen alsook natte en droge etstechnieken. Deze procedure leidt tot een dunne en hoog transparante elektrode met weerstanden onder 20 Ω per vierkant. Deze elektroden zijn bruikbaar in toepassingen gerelateerd aan ladingsinjectie, zoals licht-emitterende dioden en aan ladingsextractie zoals organisch zonnecellen. Hier werken zij met een gelijkaardige en zelfs betere kwaliteit dan hun ITO tegenhangers.

De zonnecellen zijn verder bestudeerd in hoofdstuk 4. Hier is een procedure beschreven over hoe de effecten van donker- en licht-geïnduceerde lekstromen uit JV-karakteristieken geanalyseerd kunnen worden. Op deze manier zien we dat wanneer BNCD:Cr/Au elektrodes gebruikt worden, er hoge lekstromen zichtbaar worden in vergelijking met de ITO-gebaseerde referentiepreparaten. Kelvin probe metingen van de BNCD:Cr/Au elektroden, bedekt met PEDOT:PSS, laten zien hoe PEDOT:PSS de werkfunctie van de onderliggende Cr/Au electrode beïnvloedt. Op plaatsen waar de donkere lekstromen hoog zijn, is de PEDOT:PSS-laag beschadigd. Hierdoor ontstaan er lokaal verhoogde lekstromen van de Au elektrode in de actieve laag. Bij hoog ingebouwde elektrische veldsterkten of bij de kortsluitstroom, neutraliseren de 'lekkende' elektronen uit het Au-netwerk, de door licht gegenereerde vrije holten op een bimoleculaire manier. Op deze manier wordt de driftlengte en de gerelateerde collectie-efficiëntie van de foto-gegenereerde ladingen verminderd en wordt een licht-geïnduceerde lekstroom gegenereerd. Hiernaast wordt ook de ladingsoverdrachtenergie, gemeten met FTPS vanuit de kortsluitstroom, aangetast. Bij de openketen spanning zullen de lekkende ladingen in 'trap'-niveaus in de bandgap van de actieve lagen gevangen worden, waardoor een 'trap'-geassisteerde recombinatie geïnduceerd wordt. Op basis hiervan kunnen we dus benadrukken dat in de ontwikkeling van hybride transparante elektroden, de effecten van lekstromen zo veel mogelijk vermeden moeten worden. Een goed elektronen blokkerend materiaal met hoge affiniteit voor de Au-netwerk is eveneens van groot belang om de aanwezigheid van elektronen in het holte extractiegebied van de actieve laag zo laag mogelijk te houden. Hoge adhesie-eigenschappen van de elektron blokkerende laag voor het BNCD kan

langs de andere kant ook handig zijn om de werkfunctie te verbeteren. Dit leidt op zijn beurt tot een verbetering van de open keten spanning en device efficiëntie.

English summary

Organic solar cells are an upcoming technology in the area of photovoltaic energy conversion. It distinguishes itself from classical silicon based solar cells according to the following characteristics: Mechanical flexibility ('flexible' solar cells), esthetic possibilities (freedom in design and color), improved response for indoor and diffuse light (interesting for indoor energy supply for mobile applications) and simple low cost processing possibilities (e.g. printable solar cells). These unique properties make organic solar cells interesting for certain niche applications (such as building integrated photovoltaics (BIPV)). Due to low efficiency and stability, currently only a few commercial applications are available and a major breakthrough is waiting. Research is performed all over the world for increasing the device efficiency and lifetime. Also environmentally green and robust production processes are being developed.

In organic solar cells, a combination of two components is normally used in the photo-active layer and the rare and expensive material Indium Tin Oxide (ITO) is used as transparent electrodes. The innovative routes explored in this work are: (I) the use of graphene as a 3rd component in the active layer and (II) the use of diamond as an electrode material in order to replace ITO.

The following research questions were investigated in this work:

1. *What effect will graphene have on thin polymer:fullerene solar cell devices when the graphene is used as a ternary component in the active layer at densities below percolation densities?*
2. *Is it possible to replace Indium Tin oxide (ITO) by constructing transparent electrodes based on diamond and what are the physical characteristics of diamond electrodes? Is it possible to use these diamond based electrodes for Polymer Light Emitting Diodes (PLED) and Organic Photovoltaic (OPV) devices?*

Graphene as a third component in donor:acceptor organic solar cells

In organic solar cells, a combination of two components is normally used in the photo-active layer: an electron donating material (e.g. conjugated polymer) and an electron accepting material (e.g. a fullerene derivate). In this work, the influence of the addition of a third component, graphene, is investigated. In particular, the effect of graphene for the regulation of the charge transport is explored.

In Chapter 2 we identified the threshold concentration for graphene in thin film solar cells and investigated the effects of graphene below this threshold voltage. When graphene is used above the threshold fraction, where graphene flakes start to cluster, this results in increased dark leakage currents, which finally degrade device performances. Light induced leakage currents are less prominent in this study. This is due to the fact that PEDOT:PSS layers remained passive with respect to the origin of the leakage currents. The addition of low concentrations of graphene in P3HT:PCBM solar cell devices induces a balance in hole- and electron transport mobilities. This induces increased efficient photocurrent escape from devices. The reduction of electron mobility is due to

trapping of electrons from PCBM in graphene induced electron trapping centers. The enhancement of hole mobility results from enhanced P3HT crystallinity in the active layer after graphene addition. These two effects result in lower ambipolar charge mobility while electron and hole mobilities are balancing out. This results in turn to higher charge extraction efficiencies and ultimately to improved solar cell device performance.

BNCD:Cr/Au as transparent electrode for organic electrical applications

A key challenge for future opto-electronic applications is the replacement of expensive and scarce Indium Tin Oxide (ITO) with highly stable and transparent electrodes. In chapter 3, an alternative is developed for the integration of a gold metal grid within transparent BNCD layers. This is carried out with a procedure involving lithography, metal depositions and wet and dry etching. This procedure results in thin, highly transparent electrodes with sheet resistance values below 20 Ω/sqr. These new electrodes are usable in applications involving charge injection, such as PLEDs, and charge extraction, such as organic solar cells. Here, they show the possibility to work with similar or even higher performance qualities compared to their ITO alternatives.

Solar cell properties are further investigated in Chapter 4. Here we describe a procedure using JV-characteristics for analyzing effects of dark and light induced leakage currents. We see that higher leakage currents are present in devices where BNCD/Cr:Au electrodes are used compared to their ITO counterparts. Kelvin probe measurements on BNCD:Cr/Au electrodes, covered with PEDOT:PSS show how PEDOT:PSS manipulates the work function of the underlying BNCD:Cr/Au layer. At positions where dark leakage currents are high, the PEDOT:PSS layers might be damaged. This causes increased local electron leakage from the Au electrode in the active layer. Under high internal electrical fields or at short circuit current, leaking electrons from the Cr/Au grid recombine with photo generated free holes in a bimolecular fashion. Therefore, drift lengths and related collection efficiency of photo-generated charge carriers are reduced, resulting in a light induced leakage current. Also the charge transfer energy, as measured with FTPS at short circuit current conditions, is affected. At open circuit voltage, leaking electrons reside in trapped states inside the band gap of the active layer inducing trap assisted recombination. Therefore, it must be emphasized that for the development of hybrid transparent electrodes, the effects of leakage currents should be reduced as much as possible. Also an electron blocking material, with high affinity to the metal grid of the electrode, should be used in order to reduce electron leakage from the Au-grid in the hole extraction region of the active layer. Good adhesion of the electron blocking layer to the BNCD-electrode can be useful in order to increase its work function, enhancing the open circuit voltage and device efficiency.

List of abbreviations and symbols

Abbreviation	Full word
R_{sh}^{Au}	Sheet resistance of gold layer
R_{sh}^{BNCD}	Sheet resistance of BNCD layer
μ	Mobility
A	Absorbance
A_{Au}	Absorbance of gold layer
A_{BNCD}	Absorbance of BNCD layer
AFM	Atomic force microscopy
Au	Gold
b	Width of unit cell of hybrid electrode
BHJ	Bulk heterojunction
BNCD	Boron doped nanocrystalline diamond
CELIV	Charge Extraction by Linearly Increasing Voltage
Cr	Chromium
Cu	Copper
d	Width of BNCD part of hybrid electrode
DC	Direct current
DCB	1,2 Dichlorobenzene
Disp	Dispersion
DMA	N,N dimethyl acetate
DR	Double resonance
E	Electrical field
e/q	Unit charge
E_{ct}	Charge transfer energy
E_{ct}	Charge transfer energy
EL	Electroluminance
E_t	Trapping energy
eV	Electron volt
FET	Field effect transistor
FLG	Few layered graphene
FTO	Fluorine tin Oxide
FTPS	Fourier Transform Photocurrent Spectroscopy
FWHM	Full Width at half maximum
G	Charge carrier generation rate
GB	Graphene centrifuged at 25 krpm
GBL	γ-butyrol acetone
GO	Graphene oxide
GS	Graphene centrifuged at 35 krpm
i	Complex number
ITO	Indium Tin Oxide
J_{max}	Current density at maximal power point
Jo	Dark saturation current
J_{ph}	Photocurrent

J_{rec}	Leakage current
J_{sc}	Short circuit current density
JV-characteristic	Current denisyt-voltage characteristic
k	Imaginary part of the refractive index
Krpm	1000 revolutions per minute
L	Active layer thickness
l_c	Charge collection length
LOR	Lift off resist
MoO_3	Molybdenium trioxide
N	Charge carrier density
n	Real part of the refractive index
NCD	Nanocrystalline diamond
n_{ideal}	Ideality factor
NMP	N-Methyl-2- Pyrollidone
OAS	Optical Absorption spectroscopy
ODCB	Ortho-dichlolrobenzene
OLED	Organic light emitting diode
OPV	Organic photovoltaics
P	Power
P3HT	Poly(3-hexylthiophene-2,5-diyl)
PBASE	perylene bytanoic acid succidymidyl ester
PCBM	(6,6)-Phenyl C61 butyric acid methyl ester
PCE	Power conversion efficiency
PD	Position detector
PDMS	Polydimethylsiloxane
PDS	Photo thermal deflection spectroscopy
PEDOT:PSS	Poly(3,4-ethylenedioxythiophene) Polystyrene sulfonate
PET	Polyethyleentereftalaat
PLED	Polymer light emitting diode
P_{max}	Maximal power point
Pos	Position
R	Charge carrier recombination rate
$R_{sc(dark)}$	Dark induced short circuit resistance
$R_{sc(light)}$	Light induced short circuit resistance
$R_{sc(tot)}$	Total short circuit resistance
SAED	Selected area electron diffraction
SLG	Single layered graphene
SP	Surface potential
T	Transmittance
T_{Au}	Transmission of full gold layer
T_{BNCD}	Transmission of full BNCD layer
TCO	Transparent conductive oxide
TEM	Transmission electron microscopy
Ti	Titanium
TiO_2	Titanium dioxide
TPV	Transient photovoltage

V_{bi}	Built-in voltage
v_d	Drift velocity
V_{max}	Voltage at maximal power point
V_{oc}	Open circuit voltage
$V_{oc/corr}$	V_{oc} corrected for the light induced short circuit resistance
$V_{oc/uncorr}$	V_{oc} not corrected for the light induced short circuit resistance
W	Tungsten
WF	Work function
wt%	Weight percentage
ZnO	Zink oxide
ΔV_{oc}	V_{oc} difference due to correction of the light induced short circuit resistance
Φ	Luminance flux
Ω	Ohm
Ω/sqr	Ohm per square
α	Slope J_{sc} in function of light power
η	Charge collection efficiency
η_P	Power conversion efficiency
λ	Wavelength
λ	Reorganization energy
σ	Conductivity
τ	Lifetime

List of presentations

Conference posters

1. **P. Robaeys**, L. Goris, J. V. Manca, K. Haenen, K.P. Loh, M. Nesladek: Study of charge transfer in novel generation solar cells with grafted organic molecules. Diamond conference Garmish Partenkirchen 2011.
2. **P. Robaeys**, E. Bourgeois, K. Haenen, K. Kimura, K.P. Loh, M. Nesladek, J. V. Manca: New ways for the mediation of the charge transfer mechanism in P3HT:PCBM bulk heterojunction solar cells. MRS Boston 2012.
3. **P. Robaeys**, E. Bourgeois, K. Haenen, K. Kimura, K.P. Loh, M. Nesladek, J. V. Manca: New ways for the mediation of the charge transfer mechanism in P3HT:PCBM bulk heterojunction solar cells. SBDD Hasselt workshop 2012.
4. **P. Robaeys**, E. Bourgeois, D. Spoltore, W. Dierckx, J. D'Haen, K. P. Loh, F. Bonaccorso, A. C. Ferrari, K. Haenen, J. V. Manca, M. Nesladek. Enhancement of photocurrent in P3HT:PCBM bulk heterojunction solar cells by the use of graphene. SBDD Hasselt workshop 2013.
5. **P. Robaeys,** E. Bourgeois, M. McDonald, F. Vahidpour, K. Haenen, J. V. Manca, M. Nesládek.Transparent B-doped NCD electrodes for organic solar cells enabled by
   buried metal grids. SBDD Hasselt workshop 2014.

Conference talks

1. **P. Robaeys**, E. Bourgeois, J. Manca, K. Haenen, K. Kimura, M. Nesladek and K.P. Loh; Charge Transfer Mediation in P3HT PCBM bulk heterojunction solar cells by the use of Graphene. MRS Boston 2012
2. **P. Robaeys**, W. Dexters, E. Bourgeois, J. D'Haen, Jean Manca, K. Haenen, F. Bonaccorso, K.P. Loh,M. Nesladek; Mechanisms of the short circuit current enhancement in P3HT:PCBM bulk heterojunction solar cells upon graphene addition. Diamond Conference Granada 2013
3. **P. Robaeys** AND K. Gilissen, M. McDonnald, E. Bourgeois, J. D'Haen, Z. Remes, K. Haenen, J.V. Manca, W. Deferme AND M. Nesladek; Boron doped diamond as a successful replacement for ITO in organic electronics applications SBDD Hasselt workshop 2015

List of publications

1. **P. Robaeys**, F. Bonaccorso, E. Bourgeois, J. D'Haen, W. Dierckx, W. Dexters, D. Spoltore, J. Drijkoningen, J. Liesenborgs, A. Lombardo, A. C. Ferrari, F. Van Reeth, K. Haenen, J.V. Manca, and M. Nesladek(2014). 'Enhanced performance of polymer:fullerene bulk heterojunction solar cells upon graphene addition.' *Applied Physics Letters*, *105*(8), 083306. doi:10.1063/1.4893777
2. M. Peeters, K. Jiménez-Monroy, Y. Libert, C. Eurlings, W. Cuypers, G. Wackers, S. Duchateau, **P. Robaeys**, M. Nesládek, B. van Grinsven, E. Pérez-Ruiz, J. Lammertyn, P. Losada-Pérez, and P. Wagner (2014) 'Real-time monitoring of Ara h 1 aptamer functionalization and detection of the peanut allergen Ara h 1 by electrochemical impedance spectroscopy and

dissipation-mode quartz crystal microbalance'. *Journal of Biosensors & Bioelectronics 5:155*. doi: 10.4172/2167-7719.1000155

Publications in preparation

1. **P. Robaeys** and K. Gilissen, M. McDonald, E. Bourgeois, J. d'Haen, M. Daenen, K. Haenen, J. V. Manca, W. Deferme and M. Nesladek. 'Build-in metal grid structures in BNCD as transparent electrodes for organic electronic applications' (under preparation)
2. **P. Robaeys**, M. McDonald, E. Bourgeois, K. Haenen, J. V. Manca, M. Nesladek. 'BNCD transparent electrodes for organic solar cells' (under preparation)
3. S. Gielis, M. Ivanov, J. Peys, N. van den Ham, N. Pavlovic, **P. Robaeys**, M. Nesladek, J. Banys, A. Hardy, M. K. Van Bael. 'Aqueous chemical solution deposition of LuFeO3 ultra high-k films' (under preparation)

Chapter 1 Introduction

1.1. Structure of the thesis

In this introductory chapter a brief overview is given of the key subjects addressed in this thesis. In section 2, organic solar cell concepts are introduced. After a general introduction, we focus on properties of transparent electrodes in section 3 where an overview of different materials used for transparent electrodes is given. Further on, we discuss the advantages of carbon based materials. Section 4 describes how ternary components, used for the active layer, can alter the device performance in organic solar cell devices.

The structure of the thesis is devised as follows:

In **Chapter 2,** the study of graphene, at fractions below the percolation threshold, as a ternary component in P3HT:PCBM active layers is described. Firstly, the optimal centrifugal condition for graphene solutions and graphene fraction in the active blend have been determined. Optimized devices have then been prepared and their performances have been compared to the performances of classical P3HT:PCBM BHJ solar cells. The morphology of layers has been investigated by optical-, transmission electron- and atomic force microscopy. The impact of graphene addition on charge mobilities has been characterized by charge extraction by linearly increasing voltage (CELIV) and field effect transistor (FET) measurements. Selected area electron diffraction (SAED) has been used to demonstrate the relationship between variations in hole-mobility in the active layer and evolutions of P3HT crystallinity with graphene content.

Chapter 3 describes the development of a hybrid electrode consisting of BNCD layers and a gold-grid in order to obtain highly transparent and low resistive electrodes which are compatible with OPV and PLED devices. In this section the PLED characterization is discussed while in chapter 4 the application in combination with organic solar cells is described.

Chapter 4 shows a detailed description of electrode effects on P3HT:PCBM solar cell parameters. The study is performed in order to obtain information on the reproducibility of solar cell parameters of P3HT:PCBM solar cells with BNCD/Cr:Au electrodes compared to ITO electrodes. A consistent study of JV-characterization and Fourier transform photocurrent spectroscopy (FTPS) is used in order to probe the origin of the behavior of BNCD electrodes in solar cell applications and to give a framework for device optimization.

Chapter 5 lists general conclusions and the possibilities for future work

In the materials & methods appendix section an overview is given of the methods used to process carbon based materials into applicable forms, along with an overview description of the experimental measurement methods used in this work.

1.1.1. Allotropic forms of carbon

In this introduction chapter a short overview is given on the various carbon based materials and their application in solar cells. A short description regarding the general working mechanisms of organic solar cells is provided and the possibilities of carbon based materials in this context are presented.

Besides the fact that carbon is the base of all organic materials, several important materials are constructed from carbon atoms, such as graphite, graphene and diamond. The difference in electronic properties of these materials lies in the type of binding by which carbon atoms are connected in the crystalline lattice and the lattice dimensions. In the carbon electron shell, 6 electrons are present and 4 of them, the valence electrons, can be used to form chemical bonds with other atoms to form molecules [1].
The main bonding types in carbon are sp^2- and sp^3- hybridizations. In sp^2-hybridization, carbon binds with 3 other carbon atoms in 1 plane with an even angular distribution of 120°. These solid bonds are called σ-bonds. One valence electron is left to form a π-bond. This electron is more delocalized than the σ-bond and can switch between the 3 other σ-bonds as a double bond [1]. The sp^2 allotropic forms of carbon plane structures can occur in long conjugated polymer chains, 0D buckyball form, 1D carbon nanotube form and 2D graphene like forms (Figure 1-I) [2].

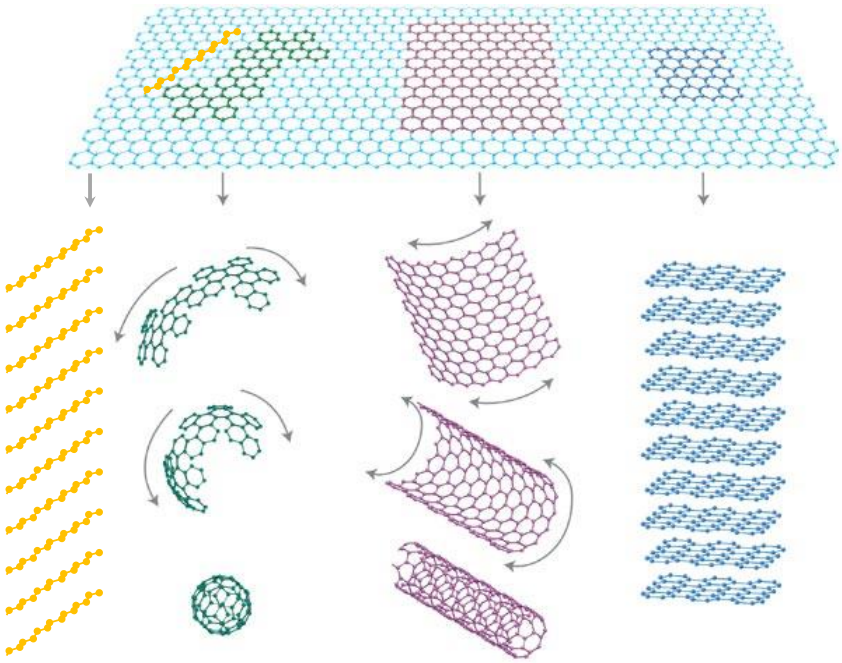

Figure 1-I: Overview of the sp^2 allotropic forms of carbon. On the left, conjugated polymers are shown. In the center left, the formation of OD buckyballs is represented. In the center right, 1D carbon nanotubes are shown and on the right, multilayer graphite sheets are shown. The original figure can be found in ref. [2].

Graphene is a material which has been investigated intensively in recent years for its superior thermal, mechanical, optical and electrical properties. Graphene is, by any measure, a story of extremes. Consisting of a few sheets of carbon

atoms, it is the strongest material ever measured, it has a thermal conductivity more than double that of diamond and has a charge mobility that is among the highest of any semiconductor [3]. Although these properties are studied in pure graphene form, their use is also interesting in graphene-polymer composites. In these composites, the main studied property is the percolation path of graphene in polymers towards high conductive materials [4]. In addition, mechanical properties are interesting since it can be used in order to interact with the polymers, inducing enhanced strength of the composite materials [5].

The fourth allotropic form of carbon, diamond, consists of 4 σ-bonds (Figure 1-II). This forms a tetrahedral framework extending throughout the solid. This structure accounts for the high hardness value of single crystal diamond. It is also an excellent heat conductor and has been used intensively in integrated circuits to protect them from overheating. The vibration of the atoms in a hot part of the crystal is rapidly transmitted to distant, cooler parts through covalent bonds [1]. The differences in the carbon binding enables fundamentally different electronic properties of these carbon materials, which enable different applications in electronics. The main goal of this thesis is to explore the use of these materials for organic solar cells and light emitting diamond applications.

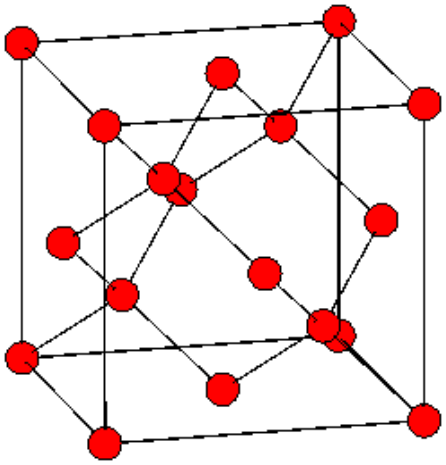

Figure 1-II: Diamond as sp^3-allotropic form of carbon.

Diamond is a carbon-based material with 4 valence electrons (Group IV in Mendeleev's table) in a sp^3 binding. It is possible to dope diamond. The elements used for diamond doping can have 1 valence electron more than carbon, such as phosphorus [6] (Group V in Mendeleev's table). This introduces an excess of electrons in the material causing n-type conductivity. When elements with less electrons than carbon, such as boron, are introduced (Group III in Mendeleev's table), an excess of holes in the material leads to p-type conductivity [7]. An overview of the activation energies of electrical conductivity in p-type boron doped diamond and n-type phosphorus doped diamond are shown in Figure 1-III.

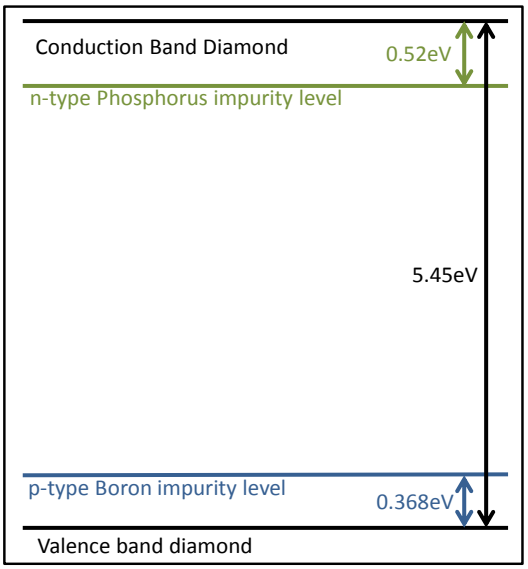

Figure 1-III: Schematic overview of the activation energies of n-type phosphorus and p-type boron impurities inside the bandgap of diamond.

A fifth allotropic form of carbon exists in the form of carbines. In this form carbon atoms are attached to each other by triple bonds. These materials were investigated in the 1950's for their interesting stiffness properties.
Conjugated polymers are polymers which are able to conduct electricity. The conduction originates from a repetition of alternating σ- and π- bonds along the polymer chain. By doping these materials the conductivity of these conjugated layers can be tuned from semiconducting (such as Poly(3-hexylthiophene-2,5-diyl) (P3HT)) to highly conductive Poly(3,4-ethylenedioxythiophene) Polystyrene sulfonate (PEDOT:PSS). The ability of these materials to absorb light is very high compared with inorganic semiconductors. Therefore, much thinner films (~100nm) of these materials are needed to absorb all the photons with energies higher than the energy gap of the polymer.
In the next sections we detail the use of these materials in relation to organic solar cell applications.

1.1.2. Organic solar cells

Polymer bulk heterojunction solar cells (BHJ) present promising commercial advantages compared to classical Si-based solar cells, such as low cost, mechanical flexibility and easy processing [8]–[10]. High efficiencies have been reached by improvements in materials, solar cell design and manufacturing [11]. The active layer of BHJ solar cells is made from a blend of an electron donating material and an electron accepting material. P3HT, a conjugated polymer, is a well-known electron donor, while (6,6)-Phenyl C61 butyric acid methyl ester (PCBM), a fullerene derivative, is often used as an electron acceptor. This active

layer is sandwiched between two electrodes of which at least one is transparent. Also at least one charge blocking layer such as PEDOT:PSS is used in order to reduce interfacial charge recombination at the interface between the electrode and active layer.

1.1.3. Graphene versus diamond for solar cell applications

One of the research aims is to prepare from carbon-based materials, thin film transparent conducting layers as electrodes for photovoltaics. In the last few years the use of graphene and its derivatives has been investigated to improve the performances of various organic electronic devices. Graphene has been successfully applied as transparent electrodes in solar cells instead of the commonly used ITO- and Fluorine tin oxide (FTO) electrodes [12]. It has been proven that graphene oxide (GO) can replace PEDOT:PSS as an electron blocking layer [13]. It has also been determined theoretically that when graphene is added to the active layer, a power conversion efficiency (PCE) as high as 12% can be reached, due to electrical charge carrier mobility enhancement [14]. Experimentally, it has also been observed that graphene electronic states can overlap with the electronic states of attached molecules. Therefore, it can act as an electron sink causing quenching of the fluorescence of P3HT, which indicates charge generation transfer at the interface between P3HT and graphene [15]. It has been observed that in organic field effect transistors, the charge mobility is enhanced when reduced graphene oxide was deposited at the interface between P3HT and SiO_2 [16] therefore improving the charge transport. Reduced graphene oxide has been introduced in the active layer of bulk heterojunction (BHJ) solar cells as an electron acceptor combined with P3HT, leading to PCE up to 1.4% [17]. For performance improvement, efforts have been made to chemically functionalize reduced graphene oxide with P3HT and PCBM molecules, which has led to PCEs of 1.22% [18], [19]. In this thesis we investigate graphene as a ternary component in P3HT:PCBM blend solar cells. We study the effects of graphene on the active layer at concentrations below the percolation threshold. We also investigate the origins of this effect via morphological and electrical studies.

In recent years, alternative materials have been investigated for their use as transparent electrodes to replace ITO. Substantial research was performed on the use of graphene [20]–[23], but also the potential of diamond has been investigated towards its use as a transparent electrode [24]–[26]. Diamond's advantage over metal oxides and printable p-type materials such as PEDOT:PSS can be found in its high chemical and thermal stability up to 450-600°C in air [27] and its high thermal conductivity [28]. This can be useful for improvement in the reduction in degradation of OLED device performance [29] since during operation temperatures over 80°C [30] can be reached in the device. From an electric point of view, nanocrystalline diamond (NCD), i.e. diamond films containing grains of size ~ 10- 100nm, has a low intrinsic conductivity in itself, but doping can increase the conductivity up to metallic behavior [31], [32]. Depending on the type of dopant, this conductivity can vary from n-type (as in phosphorus (P) doped diamond [31]) to p-type (as in boron (B) doped diamond [32]). B-doped diamond was also recently used for photo-anodes [24]–[26]. Electrical properties in freestanding BNCD films were investigated [33], which can be useful towards their use for conductive electrodes, as has been described

in Ref. [34]. Also the high refractive index of BNCD films [35] can be useful for construction of antireflection coatings for organic light emitting diode (OLED) devices [36].
Even though highly B-doped diamond is a disordered semimetal which is conducting, it still has a high sheet resistance compared to metal oxide electrodes. For similar problems, the use of a low resistant metal mesh has been proposed to decrease the electric resistance of electrodes [37], [38]. The conductivity is then limited by the metal grid conductivity which can be improved by increasing the thickness of the metal layer.

1.2. Solar cells

1.2.1. Solar cell parameters

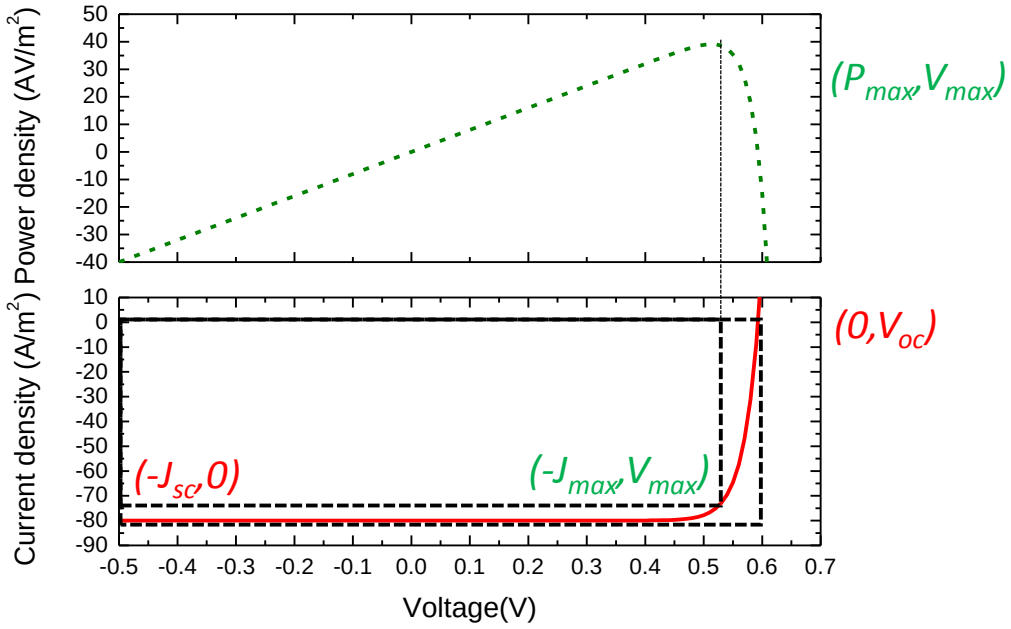

Figure 1-IV: Schematic representation of solar cell parameters as extracted from JV-curves under illumination (figure below). Also the power density as a function of the light intensity is given (upper figure).

Solar cells are devices designed for the purpose of converting solar power into electrical power. The JV-characteristics of organic solar cells are the main technique used to quantify their performance. This is measured under solar light air mass 1.5 conditions [39]. A typical characteristic is shown in Figure 1-IV. The device under illumination is characterized by the current density generated by the device in the absence of an external voltage, the short circuit current (J_{sc}) and the external voltage needed to eliminate the photo generated current completely is the open circuit voltage (V_{oc}). These two parameters determine the maximal output of the device.

The solar cell output is determined by its current generation and built-in voltage. The power is determined by the product of the current generated at a certain voltage.

$$P = JV \qquad \textbf{1-1}$$

This power is maximal at the maximal power point voltage defined as

$$P_{\max} = J_{\max}V_{\max} \qquad \textbf{1-2}$$

The comparison of voltage V_{max} and current J_{max} product at maximal power point, $P_{\max}$, with the maximal generated current and voltage at J_{sc} and V_{oc} gives a determination of the diode quality of the JV-curve: the fill factor FF is characterized by the following relation:

$$FF = \frac{J_{\max}V_{\max}}{J_{sc}V_{oc}} \qquad \textbf{1-3}$$

The device efficiency, η_p, on the other hand is a measure of the maximal amount of power generated in the device compared to the power of the incident light(P_{light}). This relation is given below:

$$\eta_P = \frac{J_{max}V_{max}}{P_{light}} \qquad \textbf{1-4}$$

1.2.2. OPV-devices

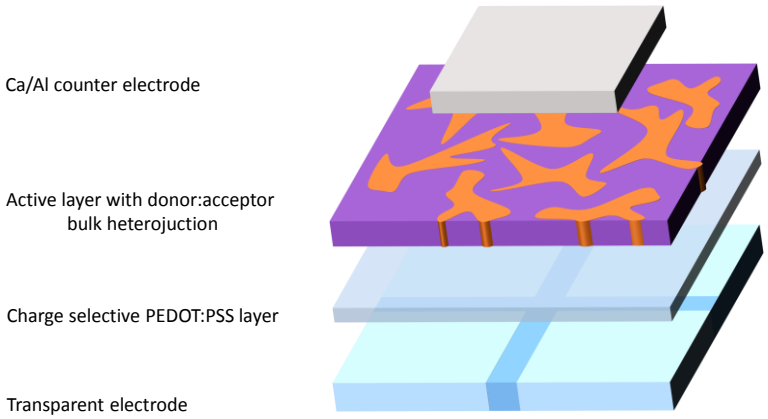

Figure 1-V: Device setup of an organic solar cell.

Organic solar cells are devices with the potential to convert light power into electrical power. The active layer consists of an intermixed network of organic electron-donating, and electron –accepting materials.

In a standard device setup (Figure 1-V), organic solar cells consist of a transparent electrode, a hole transporting layer or electron blocking layer, an active layer and a metal counter electrode.

The transparent electrodes used currently are mainly made of metal oxides such as indium tin oxide (ITO) or FTO. ITO is a rare-earth material and their resources are limited. To solve this problem, highly conductive polymers can be used as a promising alternative to ITO, however their thermal stability and conductivity is low. In recent years, carbon-based materials such as BNCD have gained a lot of interest as a viable alternative to previous materials due to their low cost and stability.

The active layer of solar cells is constructed from a polymer layer with thicknesses in the range of 100-300 nm. In this layer, free electric charge carriers can be generated and they are extracted by the electrode system. The active layer consists of an electron donating- and an electron accepting material [40]. Polymers have been used as electron donating materials due to their high absorption coefficients, a conjugated polymer backbone is also necessary for the hole transport in the organic device. Carbon-based materials such as fullerenes have been used in the last decade as an electron accepting material for their efficient electron reception [41].

The charge selective PEDOT:PSS layer is often used in solar cell devices. In order to diminish the electron recombination at the solar cell interface, the diffusion of electrons towards the electrode should be blocked by the use of an electron blocking layer [42]. This layer can be inorganic, polymeric, organic or carbon based. Inorganic materials such as TiO_2 [43] and MoO_3 [44] are examples of a good electron- and hole blocker which can be used in organic solar cells. A common polymer variant of an electron blocking layers is PEDOT:PSS [42]. Also graphene oxide has shown charge selective transport properties [45].

1.2.3. General working mechanism of organic solar cell devices

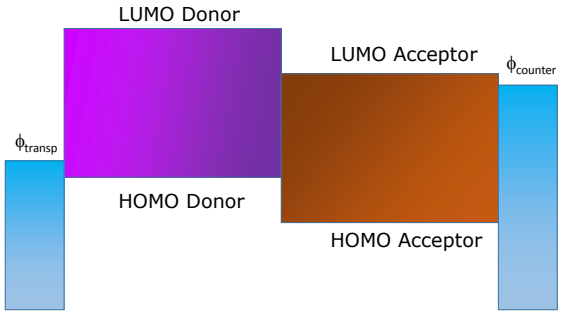

Figure 1-VI: Schematic representation of energy levels in organic solar cells.

Polymers are characterized by their highest occupied molecular orbitals and lowest unoccupied molecular orbitals. Organic solar cells band structure consist of aligned electronic bands of donor and acceptor materials sandwiched between a transparent electrode with work function ϕ_{transp} and a counter electrode with work function $\phi_{counter}$ (Figure 1-VI). When these materials are in contact with each other, the Fermi-levels of these materials will align and an internal electrical field will form. The slope of the electric field is defined as:

$$E = \frac{V_{bi}}{L} \qquad \textbf{1-5}$$

Where L is the thickness of the active layer and V_{bi} the built-in voltage (Figure 1-VII).

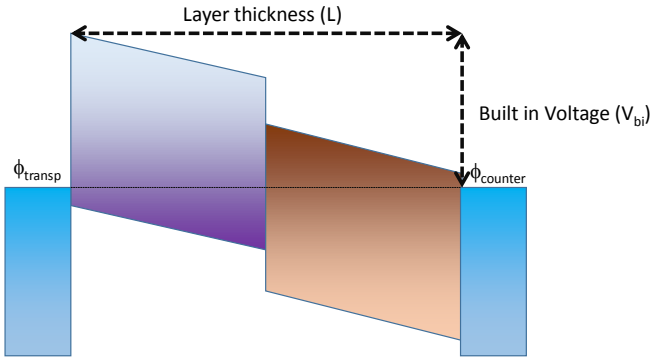

Figure 1-VII: Effect of work function alignment on the origin of the built-in voltage.

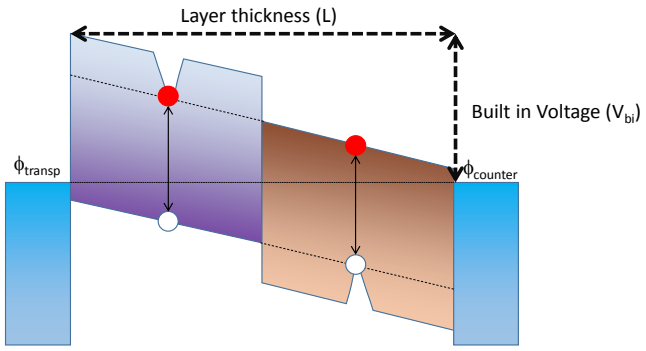

Figure 1-VIII: After light absorption, excited electrons and holes are not free but bond to each other in excitons. These neutral excitons diffuse into the bulk material before they reach a donor/acceptor interface or recombine again to a neutral state.

When light is absorbed in the donor material, excitons are formed (Figure 1-VIII). Excitons then diffuse through the OPV structure reaching the donor acceptor interface, where the charge transfer and subsequent charge separation occurs. This happens by the formation of an intermediate state: the charge transfer (CT) complex (Figure 1-IX). Charge carriers in this state have the possibility to recombine to the ground state by radiative recombination or to be separated under the influence of the interfacial and internal electrical fields [46]. The relation between the CT-state, charge generation and radiative recombination is described in the work of Vandewal et al. [47]. Effects of the active layer composition and morphology on the CT-properties were investigated by Vandewal et al. [48] and Piersimoni et al. [49].

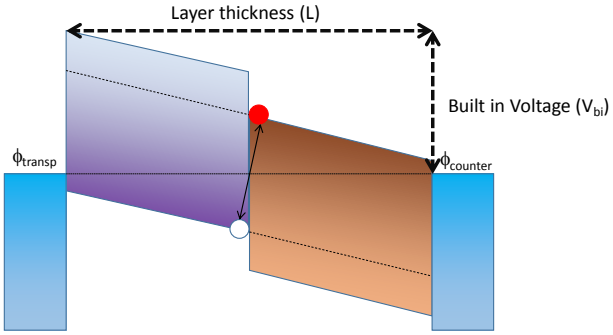

Figure 1-IX: Charge transfer state at the interface between electron donating and accepting materials.

After charge separation, electrons and holes are transported in the electron accepting and electron donating materials respectively under the influence of the internal electric field. Since this process occurs throughout the active layer it can thus be represented as described in Figure 1-X:

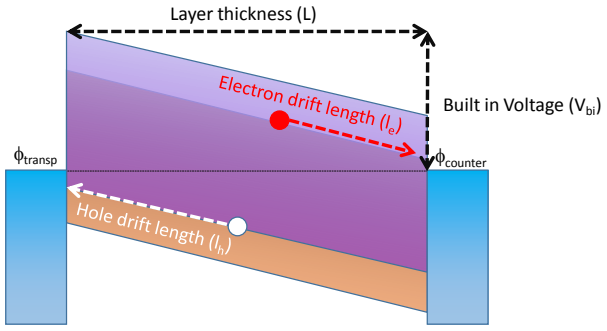

Figure 1-X: Charge transport under J_{sc} conditions after CT-state splitting.

Under the electric field generated by the built-in voltage, free electrical charge carriers are transported to the collecting electrode (Figure 1-X). Some of the free charge carriers will reach the electrode and generate a measurable current. Other charge carriers will recombine. The transport distance before

recombination should thus be as large as possible. This transport distance is called the drift collection length l_{drift}. The drift collection length can be determined from the drift velocity v_d by the following relation [50]:

$$v_d = \frac{l_{drift}}{\Delta t} \qquad \textbf{1-6}$$

Where Δt can be defined as the time needed to be transported through the device. Charge mobility is related to the drift velocity according to:

$$\mu = v_d E = \frac{l_{drift}}{\Delta t} E \qquad \textbf{1-7}$$

Since the electrical field in a device can be defined as the voltage built-in between a layer with thickness L, this relation can be transformed to:

$$\mu = v_d E = \frac{l_{drift}}{\Delta t} \frac{V_{bi}}{L} \qquad \textbf{1-8}$$

Where Δt is equal to the time needed to escape the device. If the lifetime τ of the generated charge is larger then Δt, the $\mu\tau$ -product can be defined as:

$$\mu\tau = \frac{l_{drift} V_{bi}}{L} \qquad \textbf{1-9}$$

When the drift length is higher than the device thickness, charge carriers are extracted and a photocurrent is generated related to a charge carrier generation rate (G). Charge carriers also have the possibility to recombine with a recombination rate (R).

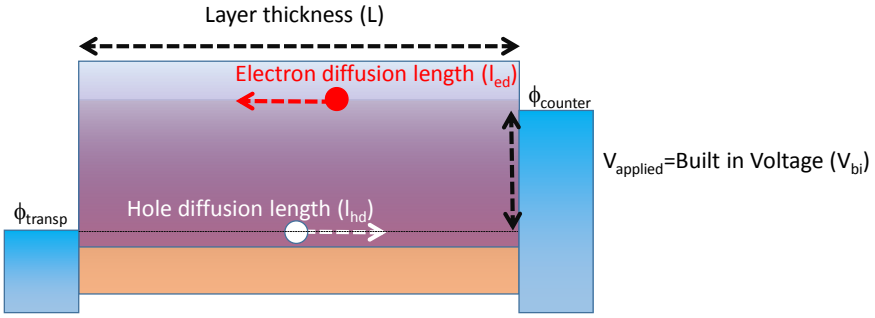

Figure 1-XI: Under V_{oc} conditions the internal electrical fields are neutralized. The movement of charge carriers under these conditions consists of thermally activated diffusion currents.

At open circuit voltage, the rate of charge carrier generation is equal to the rate of charge recombination carrier R and the built-in voltage is canceled. This makes the diffusion character of the charge carrier more important.

1.3. Transparent electrodes

Transparent electrodes are an indispensable part of the majority of solar cell structures (See Figure 1-V). The crucial requirements for thin film transparent electrodes are conductivity and transparency [51].
The conductivity σ of a material is determined by the following relation:

$$\sigma = Ne\mu \qquad \textbf{1-10}$$

Here, e is the elementary charge, N is the charge carrier concentration and μ is the charge carrier mobility, which is a measure of the velocity of the charge carriers in the presence of an electric field.

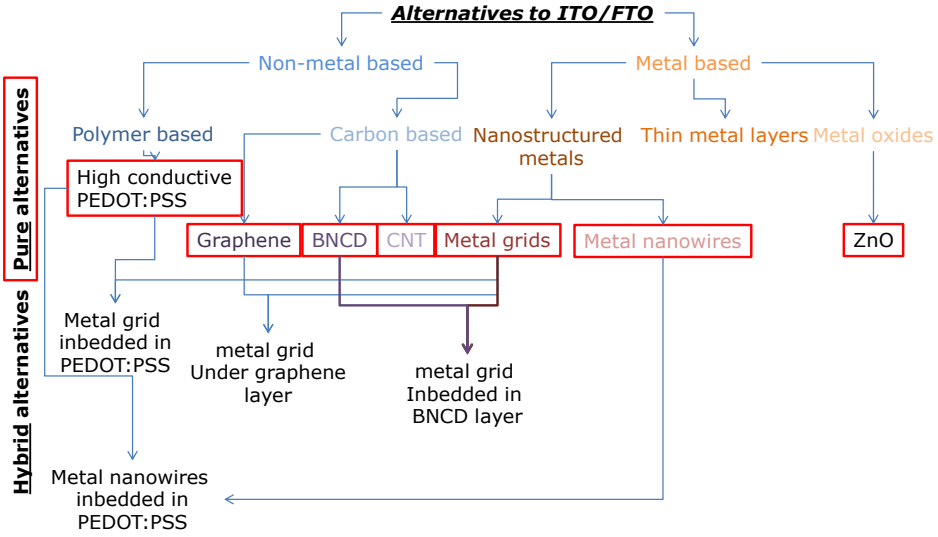

Figure 1-XII: Overview of transparent electrodes.

The group of conductive electrodes can be subdivided into 5 subgroups (Figure 1-XII) [52], [53]: metals in the form of thin metal layers and nanostructures, metal oxides, polymers and carbon-based materials. Metals are characterized by high carrier concentrations corresponding to high conductivity but also high optical absorption with resonant plasma frequencies in the UV-part of the spectrum[51]. Semiconductors have intrinsically low free charge carrier concentrations but higher transparency. By doping semiconductors the intrinsic conductivity can be enhanced, but this leads to a decrease in their transparency [54]. Graphene can be used as conducting layers absorbing ~ 2% of the light per monolayer, however intrinsic graphene conductivity is still lower compared to that of TCO electrodes used currently, due to graphene's carrier mobility [51]. Boron doped diamond is another perspective thin film conducting material, however it has not yet been explored intensively for thin conducting electrode applications.

1.3.1. Transparent conductive oxides (TCO)

Tin oxides started to gain popularity during the Second World War for their use as heated windscreens for cockpit windows and antistatic windows. Broad industrial use of Tin oxides began at the end of the 1960's, when scientists used infrared light filters composed of Tin or In_2O_3 in low-pressure sodium discharge lamps to increase lamp efficiencies by reducing heat losses. After the oil crisis in the 1970's, the main application of ITO was as a heat mirror on window glass, for saving energy. But due to the costs of indium, its use in this application was quickly abandoned and replaced by the use of more abundant materials [51].
The use of TCO's as transparent electrodes started to emerge shortly after the start of the Second World War for their use in front electrodes in selenium rectifier photocells [51]. TCOs are interesting due to their wide optical bandgap of >3eV making them optical transparent in the visible range. TCOs electrical conductivity can be increased by doping without any loss in transparency. TCOs deposition is mainly based on physical- and chemical vapor deposition, which makes them less interesting for upscaling. Sol-gel methods have also been investigated for TCO preparation, but sol gel TCOs conductivity is lower compared to vapor deposition alternatives. TCOs transparencies (90%) and low resistivity (1E-4 Ω/cm) [55] make them useable for transparent electrodes in optoelectronic applications such as flat panel displays and inorganic solar cells [53].

1.3.2. Conductive polymers: PEDOT:PSS

An alternative to TCOs are conductive polymers. The most important advantage of these polymeric transparent conductors is the solution process preparation technology [56], [57]. Poly(3,4-ethylenedioxythiophene):poly(styrenesulfonate) or PEDOT:PSS are the most widely used for application as transparent electrodes. PSS is a polymer with deprotonated sulfonyl groups carrying negative charge. This is added to the PEDOT during polymerization as a charge balancing counter ion. It also improves the solubility of PEDOT in aqueous medium [58],[53]. Initially, PEDOT:PSS was used as an antistatic coating with σ of 1-10 S cm^{-1} [59]. The PEDOT:PSS conductivity can be enhanced by increasing layer thickness, but this decreases the optical transparency [60]. The use of highly conductive PEDOT:PSS as a transparent electrode has resulted in comparable performances compared to ITO-based control devices [60]. Compared to metal oxides, PEDOT:PSS electrodes have improved mechanical flexibility.

1.3.3. Graphene & BNCD

Graphene has already been used as transparent electrodes in photovoltaics, however, boron doped diamond has not. Therefore, the use of BNCD in this application has been systematically explored in this thesis.

1.3.3.1. Graphene as transparent electrode

The ease of movement of electrons in the π-states is responsible for the extraordinary electrical properties of graphene [61]. In principle, a monolayer of graphene possesses ballistic transport. Doping of graphene can result in sheet resistances in the order of 130 Ω/sqr [62].

Graphene exhibits a reflectance of less than 0.1% and an absorption of 2.3% resulting in a theoretical transmission limit of 97.7% [2], [63]. CVD-graphene has been investigated as a transparent electrode material. In practice, defects are introduced during growth and processing of graphene. These defects, such as grain boundaries and oxidative traps result in high sheet resistance. Wettability of graphene is an important parameter for solar cell fabrication, it can be improved by covalent and non-covalent surface functionalization. This can be achieved by employing self-assembly of perylene bytanoic acid succidymidyl ester (PBASE). Also the deposition of MoO_3 on the graphene can be used to improve the graphene wetting towards that of PEDOT:PSS [12], [20].
The high transparency and conductivity in graphene sheets and the ease of deposition of graphene solutions on large surfaces makes it an interesting material for large area electrodes for solar cell applications, as shown in Figure 1-XIII (a). Although the electrical transport inside the graphene flakes is high, the transport of charge carriers between different graphene flakes is more difficult. This is due to high contact resistances between different graphene flakes. As the size of individual graphene flakes is in the micrometer range, inter-flake transport limits the ultimate electrode performance. Also the wettability of graphene with electron blocking materials should be tuned in order to make the material compatible with the other components of OPV-devices [22].
Currently, high quality graphene is obtained commonly by micromechanically cleaving or by CVD growth. Both technologies are not yet fully optimized.

1.3.3.2. BNCD as transparent electrode

An important research aim of this thesis, was to answer if diamond thin films could be used as transparent conductive electrodes and compete with state of the art of graphene research. Diamond is the sp^3 form of carbon with high chemical resistance, high bulk thermal conductivity and with its bandgap at 5.45 eV, has a wide optical window from UV to IR [64]. Diamond in its purest form is an insulator but can be doped by boron (IIb diamond) becoming semiconducting or even semimetal.
Natural diamond and single crystal diamond are created at high pressure/high temperature (HPHT) conditions [65]. From the 1950's, the study of diamond growth at low-pressure conditions started with the aim to grow high-quality diamond for device applications [66]. In the 1980's, low pressure CVD-growth of diamond was developed, paving the way for electrical applications [67]. During the CVD-process a substrate, covered in diamond seeds, is placed in a CVD-reactor. During deposition a carbon containing gas, typically CH_4, is cracked into radicals by the use of a plasma. These radicals in the gas phase react with the diamond surface of the seeds on the substrate, adding new carbon species to the surface till the film covers the whole substrate. The film can be single crystal, polycrystalline or nanocrystalline diamond (NCD)
In this work, diamond is doped by the use of the group III element boron. When diamond's electrons occupy the excess hole states created by boron dopants, free holes are able to travel in the valence band of diamond. Therefore, boron doped nanocrystalline diamond (BNCD) can be used as a p-type hole conducting material. BNCD growth conditions were determined by the work of Janssen et al. [68].
In order to use BNCD as a transparent electrode, it should be deposited on a transparent substrate. In the literature, quartz [69] as well as borosilicate glass

[70] and sapphire [71] can be used. The substrate restriction is due to the fact that for the growth of BNCD, temperatures of above 500°C are needed. A good substrate adhesion and thermal expansion match and high melting points of the substrate are thus needed in order to obtain good deposition conditions for BNCD diamond.
The potential of diamond has been investigated for its use as a transparent electrode [24]–[26]. It has been demonstrated that B-doped diamond can be used in photo-anodes[24]–[26]. Recently large area deposition of BNCD diamond has been demonstrated [33], and electrical properties in freestanding BNCD films, which can be useful towards their use in flexible electrodes, has been described in Ref. [34]. Also the high refractive index of BNCD films [35] can be useful for regulating the light out coupling out of OLED devices [36].
Recently, it was shown in the work of Lim et al. [25] and Yeap et al. [26] that BNCD could be functionalized with organic dye molecules and used as a transparent conductive electrode. However, the sheet resistance of BNCD (~200 Ω/sqr) is relatively high compared to ITO devices (~20 Ω/sqr). In order to compete with current transparent electrodes, the electrode should have sheet resistances below 20 Ω/sqr in combination with transparencies of above 70%. It is thus necessary to create a hybrid structure in order to obtain lower sheet resistances in combination with high transparencies as discussed in the section on hybrid transparent electrodes.

1.3.4. Metallic nanostructures

Metal layers are lacking the transparency necessary to compete with metal oxides and carbon-based materials, however they can be used in the form of thin metal grids. In metal grids, the electrode is formed from a network of metal lines which are spaced at a regular distance (pitch). The transparency of these electrodes is determined by the line width and the pitch between them, while the sheet resistance is mainly determined by the grid thickness [72]. Its upscaling can be realized by nanoimprinting lithography [73]. In this technique, a negative of a grid pattern in photoresist is prepared by photolithography. From this photoresist pattern, a grid pattern is subsequently molded in a polydimethylsiloxane (PDMS) elastomer stamp. This PDMS stamp is used to transfer the desired grid pattern to a metal. The grid itself can then be obtained by etching of the pattern.
Additionally, low resistive metal based electrodes can also be obtained by the formation of a network of metal nanowires on a transparent substrate. In this concept, silver nanowires are processed to form a dispersed random network of metal nanowires. This can lead to transmissions and conductivities superior to ITO [74]. Like the regular metal grid patterns, the sheet resistance of the random networks of nanowires is related to the wire length, wire resistance, wire to wire contact resistance and wire density [74].
Deposition on large surfaces is easily performed by low cost techniques such as spray coating [75]. Direct-write pulse laser sintering and high intensity pulse light sintering is used to reduce contact resistances in the network at temperatures (<140°C). This is necessary when the network of silver nanowires are deposited on flexible substrates (such as polyethyleentereftalaat (PET)) which have low melting temperatures [76].

The major drawback of metal networks is a very high surface roughness, leading to interpenetration of the active layer towards the counter electrode. This leads to short circuiting of the devices.

1.3.5. Hybrid transparent electrodes

1.3.5.1. Metallic/PEDOT:PSS hybrid electrode

Despite the development of highly conductive formulations of conductive polymers such as PEDOT:PSS, their sheet resistance value still remains significantly higher than ITO. Therefore, the use of built-in silver structures has been proposed to form a metallic/PEDOT:PSS hybrid electrode. The challenge for using a hybrid electrode is the optimization required for shadow losses due to the metal grids and resistive losses due to the resistance of the combined PEDOT:PSS/metal electrode.

One way to obtain a hybrid electrode is by embedding a silver nanowire network in a PEDOT:PSS layer. The surface roughness can be decreased dramatically by pressing a deposited silver nanowire network into a PEDOT:PSS layer [77]. After preparing solar cells, efficiencies of 3.8% were obtained [77]. In the work of Galegan et al. a silver mesh structure was printed together with a PEDOT:PSS layer [78]. Different mesh shapes were attempted and optimized [79], [80].

Hybrid electrode based on metal grids and PEDOT:PSS transparent conductor layers have been constructed, resulting in performances comparable to ITO-based solar cells in both normal and inverted device geometries. Lab scale patterning can be performed by lithography, thermal evaporation by the use of shadow masks, sputtering in combination with photolithography, microfluidic deposition and nano-imprinting. Scale up can be performed by printing methods such as screen printing and inkjet printing. These techniques have proven their use to prepare electrodes for organic solar cells with superior properties compared to their ITO counterparts [81].

1.3.5.2. Metallic/carbon-based hybrid electrode

Recently, also hybrids of metal grids and carbon-based materials such as graphene have been studied. In this instance transparent electrodes were fabricated with a sheet resistance of 3 Ω/sqr and a transmission of ~80%. At 90% transmittance a sheet resistance of ~20 Ω/sqr was obtained [82].

1.4. Graphene doping of organic solar cell devices

In this thesis the use of solution processed graphene in solar cell devices is studied for the enhancement of performances of ternary OBHJ solar cells by addition of graphene to active photovoltaic organic polymers layers.

Solution processing of graphene is a scalable technology and has the possibility to generate graphene sheets of a few μm in diameter [83]. Solution processed graphene is obtained by the use of solvents to dissolve graphite and splitting it into graphene sheets. This happens due to the well-matched surface free energies of the solvent and the graphene. The solvents which are mainly used are N-Methyl-2- Pyrollidone (NMP), N,N dimethyl acetate (DMA), γ-butyrol acetone (GBL) and 1,2 Dichlorobenzene (DCB). Exfoliation is facilitated by the

use of ultrasonic bath treatment. Almost all material is exfoliated into layers with a thickness of 5 monolayers or less [84]. The use of solution processed graphene has found a well-established applicability in the world of solar cell devices. In the first part an overview is given of how solution processed graphene can be used in these devices. In the second part, we focus further on the state of the art of ternary solar cells. This description is an introduction towards the use of graphene as a ternary component in organic solar cell devices, which is further described in chapter 2.

1.4.1. Graphene based materials in alloy systems towards solution processed solar cell applications

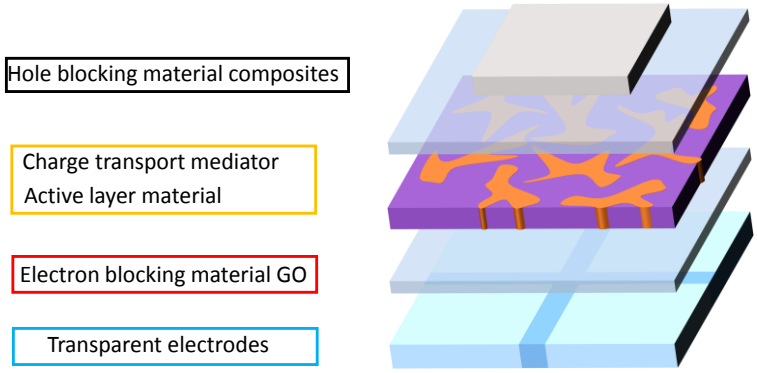

Figure 1-XIII: Different uses of graphene in organic solar cells [13],[22], [85],[86].

In organic solar cells, free electric charge generation after photoexcitation of charge carriers in the active layers is of upmost importance. Graphene in this context is studied in combination with electron donating polymers. Optical investigations have shown that graphene, in the form of flakes, blended with polymer dyes can quench fluorescence of polymer dyes [15]. This is important evidence towards the existence of energy or charge transfer between the polymer phase and the graphene phase. It could thus be used in combination with active layer materials as an electron acceptor [87]. Dispersion of graphene flakes in polymer matrixes is improved with a reduction in size down to the size of graphene quantum dots. These graphene quantum dots have the possibility to open up their band gap as their size is changing, making them a possible electron donating material. In combination with ZnO as an electron accepting material, PCE's of 0.2% were obtained [88]. In combination with P3HT, they have the possibility to act as electron acceptors. Efficiencies up to 1.28% are obtained after thermal annealing [86].
Charge transport in organic electrical devices is of vital importance in order to transport photogenerated charge carriers from their place of generation in the active layer towards the external circuit. During this process, the movement of photo generated electrons and holes should be as efficient as possible. This

means that they should not encounter each other during transport and that it should happen as fast as possible. Solution processed graphene showed improved charge transport in dye sensitized solar cells [89]. In these devices the blended graphene anchors and hybridizes with titanium dioxide (TiO_2) nanoparticles, enabling improved capture and transport of the photo induced electrons. The success of graphene lies in the larger contact area between graphene and TiO_2, which is advantageous in comparison with 1D-transporters such as nanowires and nanotubes and high internal sheet conductivity. The loaded wt% concentration with maximal performance has been found to be around 0.6 wt% increasing the device PCE from 5 to 6.9% [89].
The effects of graphene-TiO_2 material compositions have also been used as selective charge transporting layers. TiO_2 can be used as an electron selective charge transport layer. In order to obtain high performance devices, high temperature sintering of n-type pristine TiO_2 layers is necessary. It has been shown that these sintered TiO_2 compact layers can be replaced by a graphene TiO_2 composite. They can be processed at low temperatures at optimal wt% concentrations of 0.6 wt%. These transporting layers were used in combination with a perovskite based active layer. The resulting devices gave 15% efficiency in comparison with 10% efficient devices, where charge selective transport was governed by a pristine TiO_2 layer [85]. It is also possible to use graphene based materials in order to modulate hole transport in organic solar cells. Composites of graphene-oxide with PEDOT:PSS have also proven to enhance hole transporting layers in organic solar cells [90]. Also pristine graphene oxide films can be used as an efficient electron blocking material [13].
Another use of graphene in solar cell devices is as a ternary component in blended organic solar cell devices. It is known that in solution, graphene-polymer interactions can occur. During the transformation from the solution state to the solid state, crystalline phases at the graphene-organic interface can act as nucleation centers resulting in the formation of organic nucleates with preferred orientations as observed in carbon nanotubes [91].

1.4.2. Ternary solar cells: state of the art

In this next chapter we focus on the use of graphene as a ternary component in P3HT:PCBM solar cells. Ternary solar cells are solar cell devices where the active layer consists of three components, for example from an electron donor and two electron acceptors or one electron acceptor and two electron donors. The use of two electron donors is important to increase the light absorption energy range in order to create increased charge carriers. The use of various electron accepting materials can influence the interfacial band gap and regulate the open circuit voltage. Also the charge transport properties, such as charge mobility, can be modified by the ternary component [92]. These properties are key when regarding short circuit current conditions, where the internal field in the device is high and drift related properties are important.
In polymer based solar cell devices, blends of two electron accepting materials, PCBM and PDI are used in combination with a common electron donor hexaperi-hexabenzocoronene (HBC) or poly[2,6-(4,4-bis-(2-ethylhex-yl)-4H-cyclopenta[2,1-b;3,4-b´]-dithiophene)-alt-4,7-(2,1,3- benzothiadiazole)] (PCPDTBT) in order to increase the absorption window. The charge transport can also be enhanced in a ternary component by selective modulation of electron or hole mobilities. This is for example, demonstrated by the addition of 5',5''-

(9,10-bis((4-hexylphenyl)ethynyl)anthracene-2,6-diyl)bis(5-hexyl-2,2'-bithiophene) (BantHBT) small molecules as a ternary component in poly((5,5- E-alpha-((2-thienyl)methylene)-2-thiopheneacetonitrile)-alt-2,6-[(1,5-didecyloxy)naphthalene])) (PBTADN):PC70BM devices. Here BantHBT induces a mobility balance in the devices resulting in enhanced photocurrents [92].
The effect of the ternary component in active layers is strongly influenced by the interaction of the ternary component with the other materials [93]. The material interaction in solar cell devices has strong effects on the built-in voltage. This is the effect is most visible at open circuit voltage. When strong interactions exist between the ternary component and other materials, the open circuit of the resulting devices adapts even after addition of small fractions of the ternary component. When this is not the case, the open circuit voltage is only changing when the ternary component is only present at very high fractions [94].
In reference [95] P3HTT-DPP-10%: P3HT75-co-EHT25:PC61BM ternary solar cells are investigated to study the effect of the fraction of P3HT75-co-EHT25 on the open circuit voltage of solar cell devices. It is observed that due to the excellent mixing of P3HT75-co-EHT25, the V_{oc} changes in direct correlation with the fraction of P3HT75-co-EHT25 compared to the PCBM fraction in the blend. On the other hand when mixing of the ternary component is poor, as is the case for poly[N-9'-heptadecanyl-2,7-carbazole-alt-5,5-(4',7'-di-2-thienyl-2',1',3'-benzothiadiazole)] (PCDTBT) in poly(3-hexylthiophene-thiophene-diketopyrrolopyrrole) (P3HTT-DPP-10%):PCBM solar cells, the V_{oc} value remains pinned to the original PCBM value until the fraction where PCBM is not present any more in the device [94]. The influence of graphene as a ternary addition to P3HT- PCBM solar cells is investigated in the Chapter 2.

1.5. Research questions and motivations

The key question for this work was the investigation of interfacial behavior of carbon-based materials, in particular graphene and diamond along with polymers and how these carbon materials can be used for organic photovoltaic applications. Understanding of the fundamental properties of these materials is necessary for further commercialization of such devices.

The following research questions were investigated in this work:

1. *What effect will graphene have in thin polymer:fullerene solar cell devices when graphene is used as a ternary component in the active layer at densities below percolation densities?*
2. *Is it possible to construct transparent electrodes based on diamond to replace Indium Tin oxide (ITO) and what are the physical characteristics of diamond electrodes?*
3. *Is it possible to use diamond based electrodes for Polymer Light Emitting Diodes (PLED) and Organic Photovoltaic (OPV) devices?*

References

[1] P. W. Atkins, "Chemical principles," 2008.

[2] A. K. Geim and K. S. Novoselov, "The rise of graphene," *Nat. Mater.*, vol. 6, no. 3, pp. 183–191, Mar. 2007.

[3] M. Segal, "Selling graphene by the ton.," *Nat. Nanotechnol.*, vol. 4, no. 10, pp. 612–4, Oct. 2009.

[4] S. Stankovich, D. a Dikin, G. H. B. Dommett, K. M. Kohlhaas, E. J. Zimney, E. a Stach, R. D. Piner, S. T. Nguyen, and R. S. Ruoff, "Graphene-based composite materials.," *Nature*, vol. 442, no. July, pp. 282–286, 2006.

[5] U. Khan, P. May, H. Porwal, K. Nawaz, and J. N. Coleman, "Improved adhesive strength and toughness of polyvinyl acetate glue on addition of small quantities of graphene," *ACS Appl. Mater. Interfaces*, vol. 5, pp. 1423–1428, 2013.

[6] S. Koizumi, M. Kamo, Y. Sato, H. Ozaki, and T. Inuzuka, "Growth and characterization of phosphorous doped {111} homoepitaxial diamond thin films," *Appl. Phys. Lett.*, vol. 71, no. 8, p. 1065, Aug. 1997.

[7] M. W. Geis and J. C. Angus, "Diamond Film Semiconductors," *Sci. Am.*, vol. 267, no. 4, pp. 84–89, Oct. 1992.

[8] G. Dennler, M. C. Scharber, and C. J. Brabec, "Polymer-Fullerene Bulk-Heterojunction Solar Cells," *Adv. Mater.*, vol. 21, no. 13, pp. 1323–1338, Apr. 2009.

[9] C. Deibel, V. Dyakonov, and C. J. Brabec, "Organic Bulk-Heterojunction Solar Cells," *IEEE J. Sel. Top. Quantum Electron.*, vol. 16, no. 6, pp. 1517–1527, Nov. 2010.

[10] C. Deibel, T. Strobel, and V. Dyakonov, "Role of the charge transfer state in organic donor-acceptor solar cells.," *Adv. Mater.*, vol. 22, no. 37, pp. 4097–111, Oct. 2010.

[11] "Heliatek consolidates its technology leadership by establishing a new world record for organic solar technology with a cell efficiency of 12%," *Heliatek*.

[12] Y. Wang, X. Chen, Y. Zhong, F. Zhu, and K. P. Loh, "Large area, continuous, few-layered graphene as anodes in organic photovoltaic devices," *Appl. Phys. Lett.*, vol. 95, no. 6, p. 63302, Aug. 2009.

[13] S.-S. Li, K.-H. Tu, C.-C. Lin, C.-W. Chen, and M. Chhowalla, "Solution-processable graphene oxide as an efficient hole transport layer in polymer solar cells.," *ACS Nano*, vol. 4, no. 6, pp. 3169–3174, 2010.

[14] V. Yong and J. M. Tour, "Theoretical Efficiency of Nanostructured Graphene-Based Photovoltaics," *Small*, vol. 6, no. 2, pp. 313–318, 2010.

[15] Y. Wang, D. Kurunthu, G. W. Scott, and C. J. Bardeen, "Fluorescence quenching in conjugated polymers blended with reduced graphitic oxide," *J. Phys. Chem. C*, vol. 114, pp. 4153–4159, 2010.

[16] A. Liscio, G. P. Veronese, E. Treossi, F. Suriano, F. Rossella, V. Bellani, R. Rizzoli, P. Samorì, and V. Palermo, "Charge transport in graphene–polythiophene blends as studied by Kelvin Probe Force Microscopy and transistor characterization," *J. Mater. Chem.*, vol. 21, no. 9, pp. 2924–2931, 2011.

[17] Z. Liu, Q. Liu, Y. Huang, Y. Ma, S. Yin, X. Zhang, W. Sun, and Y. Chen, "Organic photovoltaic devices based on a novel acceptor material: Graphene," *Adv. Mater.*, vol. 20, pp. 3924–3930, 2008.

[18] D. Yu, Y. Yang, M. Durstock, J.-B. Baek, and L. Dai, "Soluble P3HT-Grafted Graphene for Efficient Bilayer Heterojunction Photovoltaic Devices," *{ACS} Nano*, vol. 4, no. 10, pp. 5633–5640, Oct. 2010.

[19] D. Yu, K. Park, M. Durstock, and L. Dai, "Fullerene-Grafted Graphene for Efficient Bulk Heterojunction Polymer Photovoltaic Devices," *J. Phys. Chem. Lett.*, vol. 2, no. 10, pp. 1113–1118, 2011.

[20] Y. Wang, S. W. Tong, X. F. Xu, B. Ozyilmaz, and K. P. Loh, "Interface engineering of layer-by-layer stacked graphene anodes for high-performance organic solar cells.," *Adv. Mater.*, vol. 23, no. 13, pp. 1514–8, Apr. 2011.

[21] D. S. Hecht and R. B. Kaner, "Solution-processed transparent electrodes," *MRS Bull.*, vol. 36, no. 10, pp. 749–755, Oct. 2011.

[22] H. Park, S. Chang, M. Smith, S. Gradečak, and J. Kong, "Interface engineering of graphene for universal applications as both anode and cathode in organic photovoltaics.," *Sci. Rep.*, vol. 3, p. 1581, 2013.

[23] Y. A. Akimov, "The Potential of Graphene as an ITO Replacement in Organic Solar Cells: An Optical Perspective," *IEEE J. Sel. Top. Quantum Electron.*, vol. 20, no. 1, pp. 36–42, Jan. 2014.

[24] Y. L. Zhong, A. Midya, Z. Ng, Z.-K. Chen, M. Daenen, M. Nesladek, and K. P. Loh, "Diamond-based molecular platform for photoelectrochemistry.," *J. Am. Chem. Soc.*, vol. 130, no. 51, pp. 17218–9, Dec. 2008.

[25] C. H. Y. X. Lim, Y. L. Zhong, S. Janssens, M. Nesladek, and K. P. Loh, "Oxygen-terminated nanocrystalline diamond film as an efficient anode in photovoltaics," *Adv. Funct. Mater.*, vol. 20, pp. 1313–1318, 2010.

[26] W. S. Yeap, X. Liu, D. Bevk, A. Pasquarelli, L. Lutsen, M. Fahlman, W. Maes, and K. Haenen, "Functionalization of Boron-Doped Nanocrystalline Diamond with N3 Dye Molecules.," *ACS Appl. Mater. Interfaces*, Jun. 2014.

[27] D. R. Tallant, J. E. Parmeter, M. P. Siegal, and R. L. Simpson, "The thermal stability of diamond-like carbon," *Diam. Relat. Mater.*, vol. 4, no. 3, pp. 191–199, Apr. 1995.

[28] S. Rossi, M. Alomari, Y. Zhang, S. Bychikhin, D. Pogany, J. M. R. Weaver, and E. Kohn, "Thermal analysis of submicron nanocrystalline diamond films," *Diam. Relat. Mater.*, vol. 40, pp. 69–74, 2013.

[29] S. Chung, J. H. Lee, J. Jeong, J. J. Kim, and Y. Hong, "Substrate thermal conductivity effect on heat dissipation and lifetime improvement of organic light-emitting diodes," *Appl. Phys. Lett.*, vol. 94, pp. 1–4, 2009.

[30] X. Zhou, J. He, L. S. Liao, M. Lu, X. M. Ding, X. Y. Hou, X. M. Zhang, X. Q. He, and S. T. Lee, "Real-time observation of temperature rise and thermal breakdown processes in organic LEDs using an IR imaging and analysis system," *Adv. Mater.*, vol. 12, pp. 265–269, 2000.

[31] H. Kato, T. Makino, S. Yamasaki, and H. Okushi, "n-type diamond growth by phosphorus doping on (0 0 1)-oriented surface," *J. Phys. D. Appl. Phys.*, vol. 40, no. 20, pp. 6189–6200, Oct. 2007.

[32] W. Gajewski, P. Achatz, O. a. Williams, K. Haenen, E. Bustarret, M. Stutzmann, and J. a. Garrido, "Electronic and optical properties of boron-doped nanocrystalline diamond films," *Phys. Rev. B - Condens. Matter Mater. Phys.*, vol. 79, pp. 1–14, 2009.

[33] A. Taylor, L. Fekete, P. Hubík, A. Jäger, P. Janíček, V. Mortet, J. Mistrík, and J. Vacík, "Large area deposition of boron doped nano-crystalline diamond films at low temperatures using microwave plasma enhanced chemical vapour deposition with linear antenna delivery," *Diam. Relat. Mater.*, vol. 47, pp. 27–34, 2014.

[34] S. D. Janssens, S. Drijkoningen, and K. Haenen, "Ultra-thin nanocrystalline diamond membranes as pressure sensors for harsh environments," *Appl. Phys. Lett.*, vol. 104, no. 7, p. 073107, Feb. 2014.

[35] M. Layani, A. Kamyshny, and S. Magdassi, "Transparent conductors composed of nanomaterials.," *Nanoscale*, vol. 6, no. 11, pp. 5581–91, Jun. 2014.

[36] M. Ma, F. W. Mont, X. Yan, J. Cho, E. F. Schubert, G. B. Kim, and C. Sone, "Effects of the refractive index of the encapsulant on the light-extraction efficiency of light-emitting diodes.," *Opt. Express*, vol. 19 Suppl 5, no. S5, pp. A1135–40, Sep. 2011.

[37] Y. Zhu, Z. Sun, Z. Yan, Z. Jin, and J. M. Tour, "Rational Design of Hybrid Graphene Films for High-Performance," *ACS Nano*, vol. 5, no. 8, pp. 6472–6479, 2011.

[38] J.-S. Yu, I. Kim, J.-S. Kim, J. Jo, T. T. Larsen-Olsen, R. R. Søndergaard, M. Hösel, D. Angmo, M. Jørgensen, and F. C. Krebs, "Silver front electrode grids for ITO-free all printed polymer solar cells with embedded and raised topographies, prepared by thermal imprint, flexographic and inkjet roll-to-roll processes," *Nanoscale*, vol. 4, p. 6032, 2012.

[39] J. Nunzi, "How to model the behaviour of organic photovoltaic cells," vol. 600, no. September 2005, pp. 583–600, 2006.

[40] C. W. Tang, "Two-layer organic photovoltaic cell," *Appl. Phys. Lett.*, vol. 48, no. 2, p. 183, Jan. 1986.

[41] M. M. Wienk, J. M. Kroon, W. J. H. Verhees, J. Knol, J. C. Hummelen, P. A. van Hal, and R. A. J. Janssen, "Efficient methano[70]fullerene/MDMO-PPV bulk heterojunction photovoltaic cells.," *Angew. Chem. Int. Ed. Engl.*, vol. 42, no. 29, pp. 3371–5, Jul. 2003.

[42] E. L. Ratcliff, B. Zacher, and N. R. Armstrong, "Selective interlayers and contacts in organic photovoltaic cells," *J. Phys. Chem. Lett.*, vol. 2, pp. 1337–1350, 2011.

[43] T. Salim, Z. Yin, S. Sun, X. Huang, H. Zhang, and Y. M. Lam, "Solution-processed nanocrystalline TiO2 buffer layer used for improving the performance of organic photovoltaics.," *ACS Appl. Mater. Interfaces*, vol. 3, no. 4, pp. 1063–7, Apr. 2011.

[44] J. Meyer, P. R. Kidambi, B. C. Bayer, C. Weijtens, A. Kuhn, A. Centeno, A. Pesquera, A. Zurutuza, J. Robertson, and S. Hofmann, "Metal oxide induced charge transfer doping and band alignment of graphene electrodes for efficient organic light emitting diodes.," *Sci. Rep.*, vol. 4, p. 5380, Jan. 2014.

[45] S.-S. Li, K.-H. Tu, C.-C. Lin, C.-W. Chen, and M. Chhowalla, "Solution-Processable Graphene Oxide as an Efficient Hole Transport Layer in Polymer Solar Cells," *{ACS} Nano*, vol. 4, no. 6, pp. 3169–3174, 2010.

[46] K. Vandewal, K. Tvingstedt, A. Gadisa, O. Inganäs, and J. V Manca, "On the origin of the open-circuit voltage of polymer–fullerene solar cells," *Nat. Mater.*, vol. 8, no. 11, pp. 904–909, Nov. 2009.

[47] K. Vandewal, K. Tvingstedt, A. Gadisa, O. Inganäs, and J. V. Manca, "Relating the open-circuit voltage to interface molecular properties of donor:acceptor bulk heterojunction solar cells," *Phys. Rev. B*, vol. 81, no. 12, p. 125204, Mar. 2010.

[48] K. Vandewal, A. Gadisa, W. D. Oosterbaan, S. Bertho, F. Banishoeib, I. Van Severen, L. Lutsen, T. J. Cleij, D. Vanderzande, and J. V. Manca, "The Relation Between Open-Circuit Voltage and the Onset of Photocurrent Generation by Charge-Transfer Absorption in Polymer : Fullerene Bulk Heterojunction Solar Cells," *Adv. Funct. Mater.*, vol. 18, no. 14, pp. 2064–2070, Jul. 2008.

[49] F. Piersimoni, S. Chambon, K. Vandewal, R. Mens, T. Boonen, A. Gadisa, M. Izquierdo, S. Filippone, B. Ruttens, J. D'haen, N. Martin, L. Lutsen, D. Vanderzande, P. Adriaensens, and J. V. Manca, "Influence of fullerene ordering on the energy of the charge-transfer state and open-circuit voltage in polymer:fullerene solar cells," *J. Phys. Chem. C*, vol. 115, pp. 10873–10880, 2011.

[50] S. R. Cowan, A. Roy, and A. J. Heeger, "Recombination in polymer-fullerene bulk heterojunction solar cells," no. July, pp. 1–10, 2010.

[51] K. Ellmer, "Past achievements and future challenges in the development of optically transparent electrodes," *Nat. Photonics*, vol. 6, no. 12, pp. 809–817, Nov. 2012.

[52] D. Angmo and F. C. Krebs, "Flexible ITO-free polymer solar cells," *J. Appl. Polym. Sci.*, vol. 129, pp. 1–14, 2013.

[53] M. Ye, M. Lv, C. Chen, J. Iocozzia, C. Lin, and Z. Lin, *Low-cost Nanomaterials*. 2014.

[54] P. P. Edwards, a Porch, M. O. Jones, D. V Morgan, and R. M. Perks, "Basic materials physics of transparent conducting oxides.," *Dalton Trans.*, no. 19, pp. 2995–3002, Oct. 2004.

[55] H. Zhou, D. Yi, Z. Yu, L. Xiao, and J. Li, "Preparation of aluminum doped zinc oxide films and the study of their microstructure, electrical and optical properties," *Thin Solid Films*, vol. 515, no. 17, pp. 6909–6914, Jun. 2007.

[56] R. R. Søndergaard, M. Hösel, and F. C. Krebs, "Roll-to-Roll fabrication of large area functional organic materials," *J. Polym. Sci. Part B Polym. Phys.*, vol. 51, pp. 16–34, 2013.

[57] R. Søndergaard, M. Hösel, D. Angmo, T. T. Larsen-Olsen, and F. C. Krebs, "Roll-to-roll fabrication of polymer solar cells," *Mater. Today*, vol. 15, no. 1–2, pp. 36–49, Jan. 2012.

[58] S. Kirchmeyer and K. Reuter, "Scientific importance, properties and growing applications of poly(3,4-ethylenedioxythiophene)," *J. Mater. Chem.*, vol. 15, no. 21, p. 2077, May 2005.

[59] Y.-H. Ha, N. Nikolov, S. K. Pollack, J. Mastrangelo, B. D. Martin, and R. Shashidhar, "Towards a Transparent, Highly Conductive Poly(3,4-ethylenedioxythiophene)," *Adv. Funct. Mater.*, vol. 14, no. 6, pp. 615–622, Jun. 2004.

[60] J. G. Tait, B. J. Worfolk, S. a. Maloney, T. C. Hauger, A. L. Elias, J. M. Buriak, and K. D. Harris, "Spray coated high-conductivity PEDOT:PSS transparent electrodes for stretchable and mechanically-robust organic solar cells," *Sol. Energy Mater. Sol. Cells*, vol. 110, pp. 98–106, 2013.

[61] H. Tetlow, J. Posthuma de Boer, I. J. Ford, D. D. Vvedensky, J. Coraux, and L. Kantorovich, "Growth of epitaxial graphene: Theory and experiment," *Phys. Rep.*, 2014.

[62] S. Bae, H. Kim, Y. Lee, X. Xu, J. Park, Y. Zheng, J. Balakrishnan, T. Lei, H. R. Kim, Y. Il Song, Y. Kim, and K. S. Kim, "Roll-to-roll production of 30-inch graphene films for transparent electrodes," no. June, 2010.

[63] F. Bonaccorso, Z. Sun, T. Hasan, and A. C. Ferrari, "Graphene photonics and optoelectronics," *Nat. Photonics*, vol. 4, no. 9, pp. 611–622, Aug. 2010.

[64] S. Koizumi, C. Nebel, and M. Nesladek, *Physics and Applications of CVD Diamond*. Wiley-VCH, 2008.

[65] "J. E. Field (ed.). The Properties of Natural and Synthetic Diamond. Academic Press, London 1992. £ 90.00. ISBN 0-12-255352-7," *Cryst. Res. Technol.*, vol. 28, no. 5, pp. 602–602, 1993.

[66] "Synthesis of diamond." Apr-1962.

[67] S. Matsumoto, Y. Sato, M. Kamo, and N. Setaka, "Vapor Deposition of Diamond Particles from Methane," *Jpn. J. Appl. Phys.*, vol. 21, no. Part 2, No. 4, pp. L183–L185, Apr. 1982.

[68] S. D. Janssens, P. Pobedinskas, J. Vacik, V. Petráková, B. Ruttens, J. D'Haen, M. Nesládek, K. Haenen, and P. Wagner, "Separation of intra- and intergranular magnetotransport properties in nanocrystalline diamond films on the metallic side of the metal–insulator transition," *New J. Phys.*, vol. 13, no. 8, p. 083008, Aug. 2011.

[69] W. B. Yang, F. X. Lü, and Z. X. Cao, "Growth of nanocrystalline diamond protective coatings on quartz glass," *J. Appl. Phys.*, vol. 91, no. 12, p. 10068, May 2002.

[70] F. Piazza, J. A. González, R. Velázquez, J. De Jesús, S. A. Rosario, and G. Morell, "Diamond film synthesis at low temperature," *Diam. Relat. Mater.*, vol. 15, no. 1, pp. 109–116, Jan. 2006.

[71] M. Yoshimoto, K. Yoshida, H. Maruta, Y. Hishitani, H. Koinuma, S. Nishio, M. Kakihana, and T. Tachibana, "Epitaxial diamond growth on sapphire in an oxidizing environment," vol. 399, no. 6734, pp. 340–342, May 1999.

[72] J. Van De Groep, P. Spinelli, and A. Polman, "Transparent conducting silver nanowire networks," *Nano Lett.*, vol. 12, pp. 3138–3144, 2012.

[73] M.-G. Kang, M.-S. Kim, J. Kim, and L. J. Guo, "Organic Solar Cells Using Nanoimprinted Transparent Metal Electrodes," *Adv. Mater.*, vol. 20, pp. 4408–4413, 2008.

[74] J. Y. Lee, S. T. Connor, Y. Cui, and P. Peumans, "Solution-processed metal nanowire mesh transparent electrodes," *Nano Lett.*, vol. 8, no. 2, pp. 689–692, 2008.

[75] V. Scardaci, R. Coull, P. E. Lyons, D. Rickard, and J. N. Coleman, "Spray deposition of highly transparent, low-resistance networks of silver nanowires over large areas.," *Small*, vol. 7, no. 18, pp. 2621–8, Sep. 2011.

[76] J. A. Spechler and C. B. Arnold, "Direct-write pulsed laser processed silver nanowire networks for transparent conducting electrodes," *Appl. Phys. A*, vol. 108, no. 1, pp. 25–28, May 2012.

[77] W. Gaynor, G. F. Burkhard, M. D. McGehee, and P. Peumans, "Smooth nanowire/polymer composite transparent electrodes," *Adv. Mater.*, vol. 23, pp. 2905–2910, 2011.

[78] Y. Galagan, E. W. C. Coenen, S. Sabik, H. H. Gorter, M. Barink, S. C. Veenstra, J. M. Kroon, R. Andriessen, and P. W. M. Blom, "Evaluation of ink-jet printed current collecting grids and busbars for ITO-free organic solar cells," *Sol. Energy Mater. Sol. Cells*, vol. 104, pp. 32–38, 2012.

[79] Y. Galagan, "Current Collecting Grids for ITO-Free Solar Cells," *Adv. Energy …*, pp. 103–110, 2012.

[80] Y. Galagan, J. E. J.m. Rubingh, R. Andriessen, C. C. Fan, P. W.m. Blom, S. C. Veenstra, and J. M. Kroon, "ITO-free flexible organic solar cells with

printed current collecting grids," *Sol. Energy Mater. Sol. Cells*, vol. 95, no. 5, pp. 1339–1343, 2011.

[81] D. Angmo, N. Espinosa, and F. Krebs, *Low-cost Nanomaterials*. London: Springer London, 2014.

[82] R. Design, H. G. Films, and H. T. Electrodes, "Rational Design of Hybrid Graphene Films for High-Performance," no. 8, pp. 6472–6479, 2011.

[83] K. R. Paton, E. Varrla, C. Backes, R. J. Smith, U. Khan, A. O'Neill, C. Boland M. Lotya, O. M. Istrate, P. King, T. Higgins, S. Barwich, P. May, P. Puczkarski, I. Ahmed, M. Moebius, H. Pettersson, E. Long, J. Coelho, S. E. O'Brien, E. K. McGuire, B. M. Sanchez, G. S. Duesberg, N. McEvoy, T. J. Pennycook, C. Downing, A. Crossley, V. Nicolosi, and J. N. Coleman, "Scalable production of large quantities of defect-free few-layer graphene by shear exfoliation in liquids.," *Nat. Mater.*, vol. 13, no. June, pp. 624–30, 2014.

[84] Y. Hernandez, V. Nicolosi, M. Lotya, F. Blighe, Z. Sun, S. De, I. T. McGovern, B. Holland M. Byrne, Y. Gunko, J. Boland P. Niraj, G. Duesberg, S. Krishnamurti, R. Goodhue, J. Hutchison, V. Scardaci, a. C. Ferrari, and J. N. Coleman, "High yield production of graphene by liquid phase exfoliation of graphite," 2008.

[85] J. T. W. Wang, J. M. Ball, E. M. Barea, A. Abate, J. a. Alexander-Webber, J. Huang, M. Saliba, I. Mora-Sero, J. Bisquert, H. J. Snaith, and R. J. Nicholas, "Low-temperature processed electron collection layers of graphene/TiO 2 nanocomposites in thin film perovskite solar cells," *Nano Lett.*, vol. 14, pp. 724–730, 2014.

[86] V. Gupta, N. Chaudhary, R. Srivastava, G. D. Sharma, R. Bhardwaj, and S. Chand "Luminscent graphene quantum dots for organic photovoltaic devices.," *J. Am. Chem. Soc.*, vol. 133, no. 26, pp. 9960–3, Jul. 2011.

[87] H. Wang, D. He, Y. Wang, Z. Liu, H. Wu, and J. Wang, "Organic photovoltaic devices based on graphene as an electron-acceptor material and P3OT as a donor material," *Phys. Status Solidi Appl. Mater. Sci.*, vol. 208, no. 10, pp. 2339–2343, 2011.

[88] M. Dutta, S. Sarkar, T. Ghosh, and D. Basak, "ZnO/graphene quantum dot solid-state solar cell," *J. Phys. Chem. C*, vol. 116, pp. 20127–20131, 2012.

[89] N. Yang, J. Zhai, D. Wang, Y. Chen, and L. Jiang, "Two-Dimensional Graphene Bridges Enhanced Photoinduced Charge Transport in Dye-Sensitized Solar Cells," *{ACS} Nano*, vol. 4, no. 2, pp. 887–894, Feb. 2010.

[90] Y. Park, K. Soon Choi, and S. Young Kim, "Graphene oxide/PEDOT:PSS and reduced graphene oxide/PEDOT:PSS hole extraction layers in organic photovoltaic cells," *Phys. Status Solidi*, vol. 209, no. 7, pp. 1363–1368, Jul. 2012.

[91] M. Giulianini and N. Motta, *Polymer Self-assembly on Carbon Nanotubes*, vol. III, no. 00213.

[92] T. Ameri, P. Khoram, J. Min, and C. J. Brabec, "Organic ternary solar cells: A review," *Adv. Mater.*, vol. 25, pp. 4245–4266, 2013.

[93] F. Machui, S. Abbott, D. Waller, M. Koppe, and C. J. Brabec, "Determination of Solubility Parameters for Organic Semiconductor Formulations a," pp. 2159–2165, 2011.

[94] P. P. Khlyabich, A. E. Rudenko, R. a. Street, and B. C. Thompson, "Influence of polymer compatibility on the open-circuit voltage in ternary blend bulk heterojunction solar cells," *ACS Appl. Mater. Interfaces*, vol. 6, pp. 9913–9919, 2014.

[95] P. P. Khlyabich, B. Burkhart, and B. C. Thompson, "Compositional Dependence of the Open-Circuit Voltage in Ternary Blend Bulk Heterojunction Solar Cells Based on Two Donor Polymers Ternary Blend Bulk Heterojunction Solar Cells Based on Two Donor Polymers," 2012.

Chapter 2 Enhanced performance of P3HT:PCBM bulk heterojunction solar cells upon graphene addition

Parts of this chapter are used in the publication:

Pieter Robaeys[*1], Francesco Bonaccorso[2,3], Emilie Bourgeois[1,5], Jan D'Haen[1,5], Wouter Dierckx[1], Wim Dexters[1], Donato Spoltore[1], Jeroen Drijkoningen[1], Jori Liesenborgs[4], Antonio Lombardo[2], Andrea C. Ferrari[2], Frank Van Reeth[4], Ken Haenen[1,5], Jean V. Manca[1,5], and Milos Nesladek[1,5]

[1]Institute for Materials Research (IMO), Hasselt University, Belgium
[2]Cambridge Graphene Centre, University of Cambridge, 9 JJ Thomson Avenue, Cambridge, UK
[3]Instituto Italiano di Tecnologia, Graphene Labs, Via Morego 30, 16163 Genova, Italy
[4]Expertise centre for Digital Media (EDM), Hasselt University, Belgium
[5]IMOMEC, IMEC vzw, Belgium

Enhanced performance of polymer: fullerene bulk heterojunction solar cells upon graphene addition

Published in *Applied Physics Letters:* 105, 083306 (2014)

2.1. Introduction

Normal active layers of organic solar cells consist of binary blends of electron donors and -acceptors. Graphene can be used as a ternary component in the active layer of organic solar cells for regulating the charge transport. This effect has already been investigated for several years [1],[2],[3],[4]. Although graphene can be used as a ternary component in the active layer [5], the power conversion efficiency and fill factor of solar cells based on graphene remained relatively low [6]. However, it was suggested that graphene can be added to OPV solar cells to improve solar cell performance by enhancing the electric charge transport and charge transfer properties. In general, such ternary blends were recently suggested as a smart approach to increase the short circuit current density [7], [8]. Engineering of sub-percolation fractions of graphene in BHJ could be important for charge transfer and collection. In this work we therefore focus on preparation of ternary blends BHJ with graphene by processing graphene sheets by the use of ultracentrifugation to tune the flake diameter below the active layer thickness. Furthermore, we study the influence of the graphene concentration on the solar cell performance. Dispersions of graphene in ortho-dichlolrobenzene (ODCB) aimed for addition to P3HT:PCBM solar cells are examined.

Although graphene has been investigated intensively in solar cell applications little is known about its dispersability in polymeric systems and its influence on the electronic transport and the charge transfer properties when added as a ternary mixture to BHJ solar cells. In this study the BHJ P3HT/PCBM solar cell is used as a model system. Although this system does not yield the highest PCE, it is widely used and cost-effective and easy fabrication makes it a good candidate in various applications. An important factor in OPV BHJ solar cells is the transport of holes, which is often a factor that limits the photo-current as the hole mobility of the electron donating polymer is far lower than the electron mobility of commonly used acceptors. Due to this imbalance, a positive space charge can build up at the transparent anode, leading to trapping of electrons near the counter electrode of the device [9]–[11]. The charge transfer properties of graphene, as well making conductive bridges in the BHJ structure to promote charge collection is the property that it can specifically bring based on its unique material characteristics.

This chapter is subdivided into the following parts

- Experimental section
  - Preparation of graphene
  - Preparation of bulk heterojunction solar cell devices
  - Characterization
- Results and discussion
  - Graphene quality by Raman spectroscopy
  - Influence of graphene on solar cell performances
  - Influence of graphene on the microscopic representations of the active blend
  - A short introduction to charge recombination and its effect on J_{sc} and V_{oc}
  - Influence of graphene on the charge transport in the active layer

- P3HT crystallinity for different graphene contents
- Charge recombination

The originality of this work lies in the study of graphene as a ternary component in P3HT:PCBM active layers, at fractions below the percolation threshold. For this purpose, the optimal centrifugal conditions for graphene solutions and graphene fraction in the active blend have first been determined. Optimized devices have then been prepared and their performances have been compared to the performances of a classical P3HT:PCBM BHJ solar cell. In order to probe the changes in the JV-curves, the morphology of the layers has been investigated by optical-, transmission electron- and atomic force microscopy. The impact of graphene addition on both electron- and hole mobilities has been characterized by CELIV and FET-measurements. SAED has been used to establish the relationship between variations of the hole-mobility in the active layer and evolutions of the P3HT crystallinity with the graphene content.

2.2. Experimental section

2.2.1. Preparation of graphene

100 mg of graphite flakes (Sigma Aldrich Ltd.) were dispersed in 10 ml of 1.2-dichlorobenzene. The solvent was chosen for its compatibility with P3HT:PCBM [12]. Moreover, 1.2-dichlorobenzene has a surface tension of 37 mN/m [13], which is close to that of ideal solvents for the dispersion of exfoliated flakes such as N-Methyl-2-Pyrrolidone [14]. This helps to minimize the interfacial tension between the liquid and graphene flakes [15]. Exploiting sedimentation based techniques, the dispersion was ultrasonicated for 10 hours and then ultracentrifuged (Sorvall WX-100) with a TH-641 swinging bucket at 25000 and 35000 rpm (151000 g) for 30 min [15]–[18]. After ultracentrifugation, the supernatant was extracted by pipetting. Optical absorption spectroscopy (OAS) was used to evaluate the concentration, c, of graphitic material in the dispersion, (a). Using the experimentally derived absorption coefficient of 1390 L/mg at 660 nm[15]–[17], we estimated the concentration of graphene in the solution.

The ultracentrifuged dispersions were diluted with 1,2-dichlorobenzene and drop-cast onto a Si wafer with a 300 nm thermally grown (Silicon dioxide) SiO_2 layer (LDB Technologies Ltd.). These samples were then used for Raman measurements, collected with a Renishaw spectrometer at 488, 514.5, and 633 nm with a 100X objective lens, with an incident power of 1 mW.

2.2.2. Preparation of bulk heterojunction solar cell devices

After determination of the concentration of the graphene supernatant by UV-Vis spectroscopy, suspensions were produced with 10 mg/ml P3HT bought from Rieke and 8 mg/ml PCBM purchased from Solenne b.v. These dispersions were stirred under a nitrogen atmosphere for 24 h at 50 ℃.

Substrates with a 100 nm ITO layer were cleaned for 20 min by ultrasonic treatment in aqueous soap solution (1/20). Afterwards they were treated

ultrasonically in acetone for 15 min, boiled in isopropanol for 15 min and were then dried using a nitrogen flow.

After cleaning, a layer of PEDOT:PSS (Stark) was deposited by spin coating for 40 s at 3000 rpm. The layers were annealed for 20 min at 120 °C. After cooling down, a 100 nm thick layer of the active blend (P3HT:PCBM:graphene) was deposited on top of the PEDOT:PSS layer by spin coating for 40 s at 750 rpm in a N_2 atmosphere. In this text, the notation x:y:z refers to the respective weight fraction of P3HT, PCBM and graphene. After spin coating the layers were annealed by solvent annealing for about 1 hour. Finally a counter electrode of 20 nm of calcium and 60 nm of aluminum was deposited by evaporation.

2.2.3. Characterization

For the morphological measurements, the active blend layers were spin coated on top of a glass substrate. Optical microscopy was performed with a Zeiss Axiovert 40 MAT with 1000x magnification. An estimation of the cluster size was made by the use of ImageJ. Atomic force microscopy was performed in tapping mode with a Veeco multi-mode nanoscope IIIa. Bright field TEM images were produced and combined with SAED by the use of a FEI tecnai spirit at 120 kV.

JV-characterization was established using a solar simulator Newport oriel class A, equipped with a Xenon Short Arc lamp with a power of 150 W. This simulator produces a parallel light beam, with a power of 1 sun at 1.5AM illuminating the solar cell. The current was measured using a home built setup based on a Keithley 2400 source meter.

FET-measurements were performed as described in reference [19]. The inorganic part of the device consists of a heavily n-doped silicon substrate with a silicon oxide layer. The gate dielectric has a gate capacitance per unit area of 16.9 nF/cm^2. On this layer gold contacts were deposited. The Au work function (-5.1 eV) and P3HT highest occupied molecular orbital (-5.1 eV) are very close leading to a small energy barrier for hole injection at zero field applied. The channel is 10 mm wide and 30 µm long.

CELIV measurements were carried out by applying a ramp voltage on the sample (supplied by a function generator (Tektronix AFG 3101)) and monitoring the current transient response using a digital oscilloscope (Tektronix TDS 620B). The ramp amplitude was varied, which allowed the extraction of the charge carrier mobility as a function of electric field [20].

We performed FTPS measurements using the modulated beam of a Thermo Electron Nicolet 8700 FTIR with the solar cell as an external detector, as described in Ref. [21]. For transient photovoltage (TPV) measurements, the devices were kept at open circuit whilst illuminated with a white light bias, used to control V_{oc}. A nitrogen pumped dye laser (λ=500 nm) was used as an optical perturbation, resulting in a voltage transient with an amplitude $\Delta V \sim V_{oc}$.

2.3. Results & discussion

2.3.1. Graphene quality

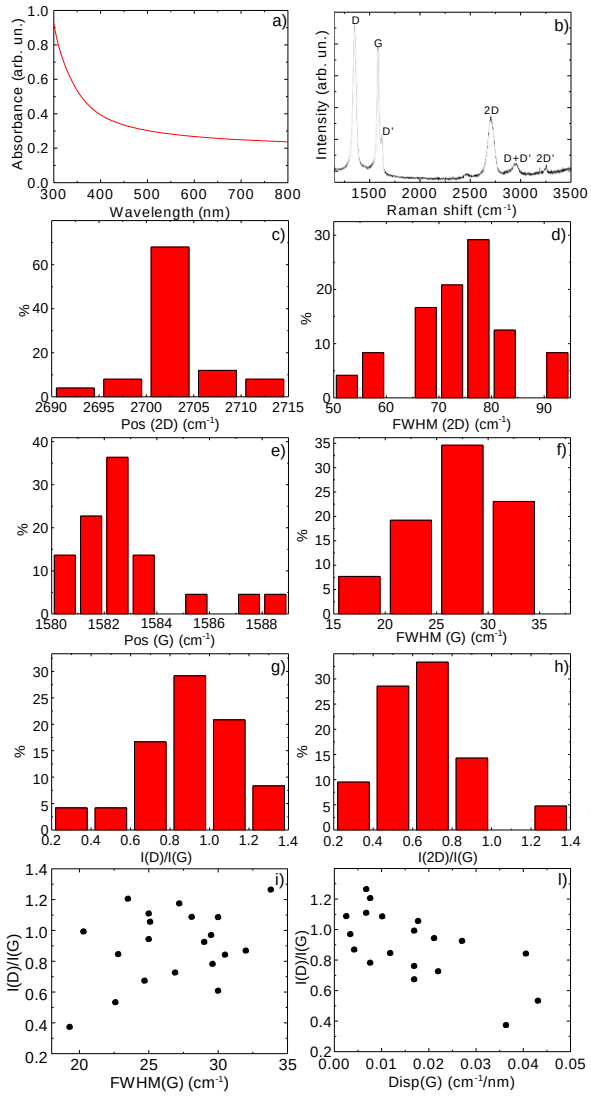

Figure 2-I: (a) Optical absorption spectrum of graphene dispersion (b) Raman spectrum measured with 514.5 nm excitation for a representative flake obtained via LPE of graphite. Distribution of (c) Pos(2D), (d) FWHM(2D), (e) Pos(G), (f) FWHM(G), (g) I(D)/I(G), (h) I(2D)/I(G). (i) Distribution of I(D)/I(G) as a function of FWHM(G), and l) Disp(G).

Figure 2-I (b) shows a typical Raman spectrum of graphene flakes on Si/SiO_2. In addition to the G and 2D peaks, this spectrum also shows significant D and D' intensities, as well as the combination mode D+D'. The G peak corresponds to the E_2g phonon at the Brillouin zone center [18], [22]–[24]. The D peak is due to the breathing modes of sp^2 rings and requires a defect for its activation by double resonance (DR) [18], [22], [23]. The 2D peak is the second order of the D peak; this is a single peak in single layer graphene (SLG), whereas it splits into 4 peaks in bi-layer graphene, reflecting the evolution of the band structure. The 2D peak is always seen, even when no D peak is present, since no defects are required for the activation of two phonons with the same momentum, one backscattered from the other [22]. DR can also occur as an intra-valley process, i.e. connecting two points belonging to the same cone around K or K' [18], [23]; this process gives rise to the D' peak. The 2D' is the second order of the D'. Statistical analysis of the spectra shows that position(2D) peaks at~2702 cm^{-1}(Figure 2-I (c), while FWHM(2D) varies from 50 to 95 cm^{-1}(Figure 2-I (d)). Position(2G) (Figure 2-I (e) and FWHM(G) (Figure 2-I (f)) are~1582 and~27 cm^{-1}. Raman spectra show significant D and D' intensity, with an average intensity ratio I(D)/I(G)~ 0.90 (Figure 2-I (g). This is attributed to the edges of the sub-micrometer flakes [25], rather than to the presence of a large amount of structural defects within the flakes. This observation is supported by the low dispersion of the G peak, position Disp(G)<0.04 cm^{-1} /nm, much lower than what is expected for disordered carbon [26]. Combining I(D)/I(G) with FWHM(G) and Disp(G) allows us to discriminate between disorder localized at the edges and disorder in the bulk. In the latter case, a higher I(D)/I(G) would correspond to higher FWHM(G) and Disp(G). Figure 2-I (i), shows that Disp(G), I(D)/I(G), and FWHM(G) are not correlated, indicating that the major contribution to the D peak comes from the sample edges. The distribution of FWHM(2D) in Figure 2-I (d) has two maxima ~57 and ~77 cm^{-1}, respectively; the latter being the highest. This is consistent with the samples being a combination of SLG and few-layer graphene (FLG) flakes.

2.3.2. Influence of graphene on solar cell performance

2.3.2.1. Determination of the optimal graphene fraction in the active blend

Solar cells have been prepared from active blends containing graphene centrifuged at two different speeds. For each centrifugation speed, the graphene fraction in the active layer has been varied between 0 and the maximal fraction after centrifugation, to investigate the influence of graphene fraction on solar cell performance.

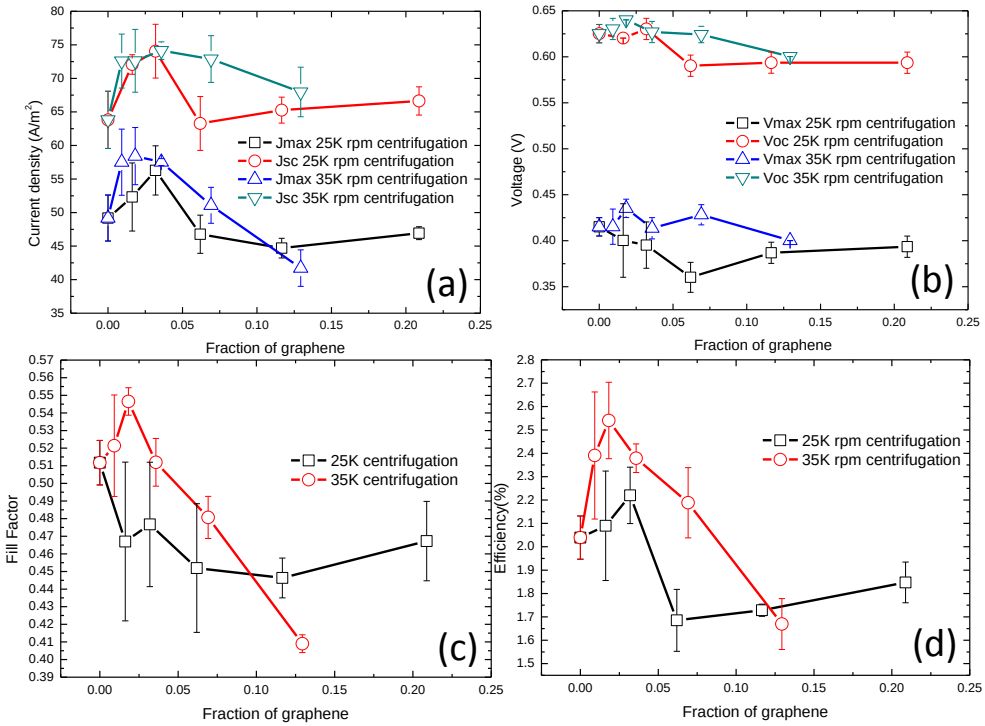

Figure 2-II: Solar cell parameters of P3HT:PCBM:G solar cell devices prepared with different fractions of graphene centrifuged at different speeds. The effects of the graphene contents on the short circuit current, open circuit voltage, fill factor and device efficiency are shown in (a)- (b)- (c)- (d).

With the results shown in Figure 2-II we can observe that for both centrifugation speeds, solar cell performances are optimal for a weight fraction of graphene around 2 wt%. The short circuit current is maximal for a graphene fraction close to 2 wt% (Figure 2-II (a)), while the open circuit voltage drops a little due to graphene addition (Figure 2-II (b)). Moreover, the addition of low concentrations of graphene flakes (centrifugation speed: 35 kilo revolutions per minute (krpm)) leads to improved solar cells fill factors and efficiencies as shown in Figure 2-II (c) and (d). Optimized devices were therefore prepared from an active blend containing 2 wt% of graphene prepared with a 35 krpm centrifugation speed. This condition is defined as GS in this text. The worst performing device, prepared from an active blend containing 21 wt% graphene centrifuged at 25 krpm has also been studied and is defined as GB.

2.3.2.2. Device characteristics

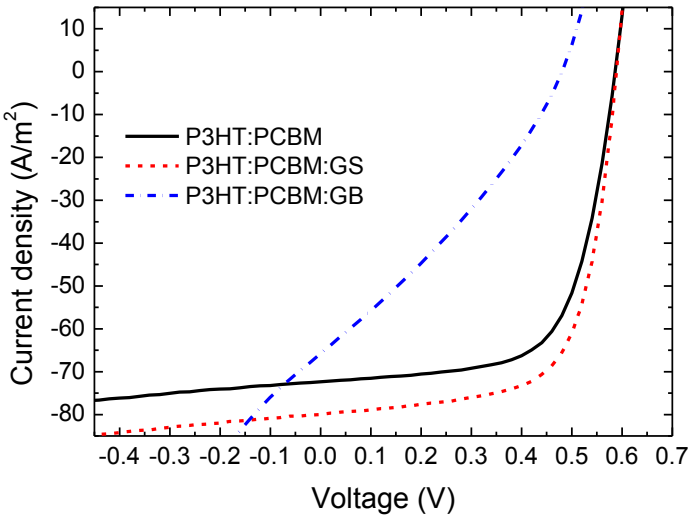

Figure 2-III: Current voltage characteristics of solar cells based on P3HT:PCBM, P3HT:PCBM:GS and P3HT:PCBM:GB blends. The respective compositions of the active layers are P3HT:PCBM (0.56:0.44), P3HT:PCBM:GS (0.55:0.43:0.02), and P3HT:PCBM:GB (0.43:0.35:0.21). For GS, graphene was centrifuged at 35 krpm. For GB, graphene was centrifuged at 25 krpm.

Four solar cells have been prepared from an active blend containing 2 wt% graphene (centrifugation speed: 35 krpm), with an optimized preparation procedure to increase the device efficiency. The performances of these solar cells were compared to performances of reference P3HT:PCBM solar cells and to the performances of solar cells containing a higher graphene fraction (21 wt%) of larger graphene flakes (centrifugation speed: 25 krpm). JV-characteristics established on these three devices are presented on Figure 2-III, while the corresponding J_{sc}, V_{oc}, FF and efficiencies are presented in Table 2-1. For each of the three different active blends, the values presented in Table 2-1 are an average of parameters measured on four different devices.

Table 2-1: Review of device properties. Average values of 4 devices are given with standard deviation. The values of the best performing cells are given between brackets.

Configuration	***weight fractions***	V_{oc} **(V)**	J_{sc} **(A/m²)**	***FF***	η_p
P3HT:PCBM	0.56:0.44	0.59±0.010 (0.6)	73.78±2.74 (73.55)	0.64±0.027 (0.65)	**2.79±0.08 (2.79)**
P3HT:PCBM:GS (35 krpm)	0.55:0.43: 0.02	0.60±3.47E-5 (0.6)	78.33±3.003 (79.11)	0.66E±0.0067 (0.66)	**3.12±0.13 (3.17)**
P3HT:PCBM:GB (25 krpm)	0.44:0.35: 0.21	0.53±0.0258 (0.53)	67.94±4.25 (67.69)	0.36±0.043 (0.37)	**1.32±0.25 (1.37)**

JV-characteristics presented in Figure 2-III show an enhancement of J_{sc} by 10 A/m^2 in the device containing graphene centrifuged with high centrifugal speeds (P3HT:PCBM:GS blend) compared to the P3HT:PCBM reference device. It can also be observed that small amounts of graphene do not reduce the device fill factor. The V_{oc} of the P3HT:PCBM:GS device remains more or less unchanged after addition of different fractions of graphene.

The observed changes in device parameters lead finally to an increase in the solar cell efficiency, from 2,79% for the reference device to 3,17% for the device based on the P3HT:PCBM:GS blend. In Table 2-1 a summary of the results is given. When the graphene flakes in the active layer become larger and the graphene fraction becomes higher (P3HT:PCBM:GB blend) reduced fill factors and efficiencies are observed.

2.3.3. Influence of graphene on morphology of the active blend

The organization of the organic blend at micro- and nanoscales has a determinant impact on the performances of BHJ organic solar cells [27]. The influence of graphene addition on the morphology of the active layer has therefore been investigated by different techniques. Optical microscopy has been used to study the general organization of the layer at the micron scale. The surface topography has been investigated by AFM and the effect of graphene on the microstructure of the active layer has been characterized by transmission electron microscopy in combination with SAED.

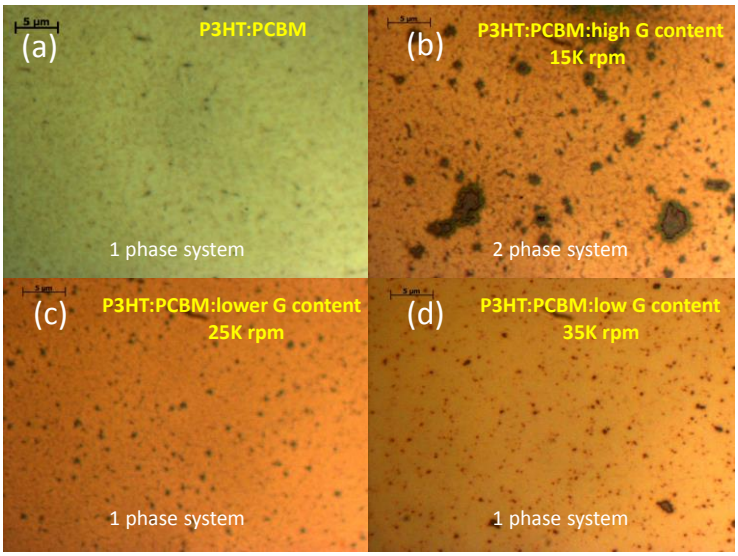

Figure 2-IV: Optical microscopy images of photoactive layers on top of a glass substrate at 1000x magnification. (a) P3HT: PCBM reference layer. (b-c-d) P3HT: PCBM: G layer with graphene centrifuged at a centrifugal speed of 15 krpm- 25 krpm(GB) -35 krpm(GS) respectively.

In this paragraph, both the influence of the centrifugal speed for the graphene centrifugation and graphene fraction in the layer have been investigated. The graphene preparation conditions and the weight fraction in the layers are shown in Table 2-1.

Optical microscopy images are presented in Figure 2-IV. A pure P3HT:PCBM layer is shown on Figure 2-IV (a). Figure 2-IV (b), (c) and (d) show images of P3HT:PCBM:graphene blends, prepared from graphene suspensions centrifuged at different speeds. In Figure 2-IV (a), it can be observed that the P3HT: PCBM blend forms a uniform layer. The darker areas in this image could correspond to PCBM aggregates, as reported in [28]. In Figure 2-IV (b), it can be seen that at low centrifugal speeds (15 krpm), corresponding to large graphene flakes and to a high fraction of graphene in the layer, graphene and P3HT: PCBM give rise to two distinct phases. The size distribution of the graphene clusters is wide and large graphene clusters are observed with a diameter around 3 µm. When the centrifugal speed is increased, i.e. for smaller graphene flakes and a lower graphene fraction in the blend, the graphene clusters in the P3HT: PCBM layer become smaller (diameter around 0.9 µm) and their size more homogeneous (Figure 2-IV (c) & 4 (d)).

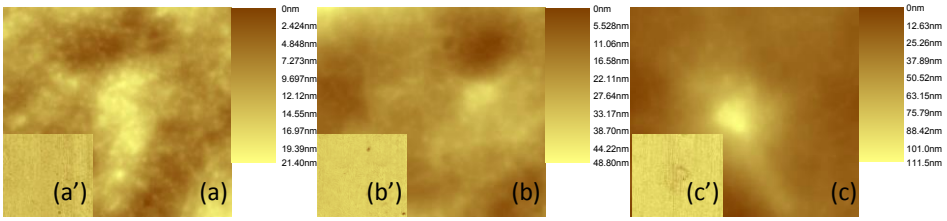

Figure 2-V: AFM images (1.0 µm by 1.0 µm) of photoactive layers deposited on a glass substrate. ((a), (b), (c)) represent the amplitude images of P3HT:PCBM (a) and P3HT:PCBM:Graphene ((b), (c)) centrifuged at 35 krpm and 25 krpm respectively. ((a'), (b'), (c')) represent the phase images corresponding to amplitude images in A, B and C. The layer composition can be found in Table 2-1.

Atomic force microscopy images in Figure 2-V reveal different topographical features in the active layers. Figure 2-V (a) shows a smooth amplitude picture of a pure P3HT: PCBM layer. The phase image in Figure 2-V (a') shows the crystalline organization of the P3HT polymer, as described in [29]. When graphene prepared at high centrifugal speeds is present in the layer, as depicted in Figure 2-V (b), the topographical roughness is increased. The phase image in Figure 2-V (b') shows that the crystalline layout of P3HT is intact. This implies that the aggregated graphene clusters are covered by a P3HT:PCBM layer. When graphene is centrifuged at low centrifugal speeds, as shown in Figure 2-V (c), the topographical roughness becomes very high and the crystal organization of P3HT is disturbed due to puncture of the P3HT:PCBM layer by graphene clusters (Figure 2-V (c')). The lower performances of solar cells prepared from a blend containing a high fraction of large graphene flakes (cf. paragraph Influence of graphene on solar cell performance) can therefore be explained by the

development of short-cuts, due to the puncture of the P3HT:PCBM layer by conductive graphene flakes.

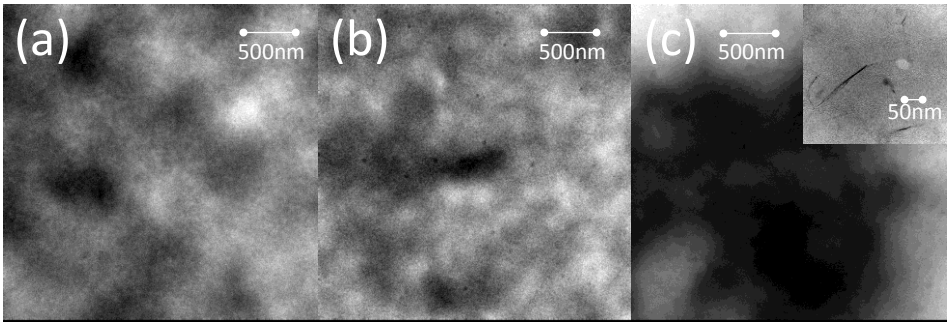

Figure 2-VI: TEM images of the photoactive layers deposited on a glass substrate. ((a), (b), (c)) depicts respectively P3HT:PCBM, P3HT:PCBM:GS and P3HT:PCBM:GB. The layer composition can be found in Table 2-1.The inset in figure C shows a higher magnification.

Figure 2-VI (a), (b) and (c) shows transmission electron microscopy (TEM) images of the active layer. The reference layer in Figure 2-VI (a) shows the typical appearance of a P3HT:PCBM active layer. Several darker and lighter regions are visible due to phase separation between PCBM and P3HT. PCBM appears darker because of the higher electron density of PCBM compared to P3HT [27]. In Figure 2-VI (b), the layer with a low fraction of small graphene flakes shows more black spots. This could correspond to small aggregates of graphene with a very high electron density. When the graphene fraction increases, as depicted in Figure 2-VI (c) the graphene flakes aggregate into bigger clusters. This confirms what was observed in optical microscopy images. Also the appearance of needle like graphene flakes varying in size between 50 and 200 nm are visible. The formation of these electron dense clusters contributes to the formation of short-cuts in solar cells prepared from blends containing a high fraction of big graphene flakes.

2.3.4. Introduction to light intensity dependent measurements and recombination

In this section, a detailed description is provided, to aid understanding of recombination mechanisms and their effects on photovoltaic parameters (e.g. V_{oc} correction). The method, developed in this work, can be considered as an alternative to the classical description of recombination which also includes the effects of leakage currents.

2.3.4.1. Device under influence of internal electrical field: light intensity dependence in a short circuit current

Interface related recombination can significantly alter solar cell behavior, both in short circuit current and open circuit conditions [30].

2.3.4.1.1. J_{sc} as a function of light intensity

Bimolecular recombination originates from collisions of 2 particle types e.g. free electrons and holes. Bimolecular recombination is intrinsically present in organic materials [31]. The recombination rate is determined by the concentration of both types of charge carriers. The recombination rate is given by:

$$R_{bi}\left(I(L)\right) = k_{bi} N\left(I(L)\right) h\left(I(L)\right) \qquad \textbf{2-1}$$

$R_{bi}\left(I(L)\right)$ relates to the product of free electron $N\left(I(L)\right)$- and hole $h\left(I(L)\right)$ densities by introducing a bimolecular rate constant k_{bi} .

If we consider the concentration of electrons and holes generated by light of a certain intensity, this relation is transformed to:

$$R_{bi}\left(I(L)\right) = k_{bi} N\left(I(L)\right)^2 \qquad \textbf{2-2}$$

The charge transport in the device is described by the continuity equation as given below:

$$\frac{dn}{dt} = G - R_{bi}\left(I(L)\right) \qquad \textbf{2-3}$$

Steady state conditions read $\frac{dn}{dt} = 0$. The previous equation can be reduced to:

$$\frac{dn}{dt} = 0 = G - R_{bi}\left(I(L)\right) \qquad \textbf{2-4}$$
$$G = k_{bi} N\left(I(L)\right)^2$$

The dependence of the light power P on the J_{sc} is superlinear, as given in the equation below:

$$J_{sc} = qGL \propto P^{\alpha} \qquad \textbf{2-5}$$

Where G is the generation rate, q is the charge and L the thickness of the device. If bimolecular recombination is the dominant recombination behavior cell, $G \propto k_{bi} N(I(L))^2$ and thus $\sqrt{G} \propto N\left(I(L)\right)$ and $\sqrt{G} \propto J_{sc}$. This will result in α equal to 0.5 [32]–[34].

If the current is in space charge mode, α can reduce to 0.75. Recent experiments have shown that this effect becomes important if the imbalance between hole and electron mobility is higher than 2 orders of magnitude [9], [10].

2.3.4.1.2. Short circuit resistance and collection length

Collection length changes under illumination, due to light dependent distribution of free electrons and holes in the charge extraction region [35], [36]. The gradient in electron and hole concentration causes diffusion currents near the collecting electrodes.

In general, the transport of charge carriers in organic solar cells are well described by the use of drift-diffusion models in combination with continuity

equations [37]. In the work of Crandall et al. [37] and Voz et al. [38], the drift dependent solar cell behavior is described by:

$$J = J_{ph}\left(1 - exp\left(\frac{-L}{l_c}\right)\right) \qquad \textbf{2-6}$$

At high internal electrical fields, the drift lengths for electrons and holes are larger than the thickness of the device. In other words, $l_c \gg L$. This means that all the charge carriers generated in the device are extracted.

Under illumination and low applied voltages, the last equation can be approximated by [38]:

$$J \approx J_{ph}\left(1 - \left(\frac{L/2}{l_c}\right)\right) \qquad \textbf{2-7}$$

Where the charge collection efficiency can be determined by:

$$\eta = 1 - \frac{L/2}{l_{co}} \qquad \textbf{2-8}$$

The light induced leakage current can be defined from the previous equations as

$$J_{rec} \approx J_{ph}\left(\frac{L/2}{l_c}\right) \qquad \textbf{2-9}$$

The leakage current is related to a leakage resistance R_{sc} as:

$$R_{sc} = \frac{V_{BI}}{J_{rec}} = \frac{V_{BI}}{J_{ph}}\frac{l_c}{L/2} \qquad \textbf{2-10}$$

2.3.4.2. No electrical field: open circuit voltages as a function of light intensity

In this thesis, we developed a method to differentiate between different types of short circuit resistances by the use of light intensity dependent measurements. Besides the effects of leakage of charge carriers, free charge carrier concentration can decrease by recombination of charge carriers by trap assisted recombination mechanisms. This induces a deviation from the normal charge behavior, included in the ideality factor [39]. In this work we developed a method to deconvolute the effects of short circuit resistance from those of the ideality factor and dark saturation current. The effects of light intensity on the open circuit voltage are discussed below.

In trap assisted recombination mechanisms, free charge carriers recombine with trapped charge carriers.

The diffusion character of an open circuit voltage is based on the diode equation as described by [39],[40]

$$J = -J_{sc} + J_0\left(exp\left(\frac{eV}{n_{ideal}kT}\right) - 1\right) \qquad \textbf{2-11}$$

With the addition of a light intensity dependent leakage current, this relation is transformed to:

$$J = -J_{sc} + J_0\left(exp\left(\frac{eV}{n_{ideal}kT}\right) - 1\right) - \frac{V}{R_{sc}} \qquad \textbf{2-12}$$

The dark shunt resistance and dark leakage current is in competition with the light intensity dependent shunt resistance and –leakage current in order to influence the total shunt resistance. This competitive behavior can be described as:

$$\frac{1}{R_{sc(tot)}} = \frac{1}{R_{sc(dark)}} + \frac{1}{R_{sc(light)}} \qquad \textbf{2-13}$$

Where $R_{sc(light)}$ is dependent on the light intensity as follows:

$$R_{sc(light)} = \exp(C\ln(J_{sc}) + DD) = \exp(DD)J_{sc}{}^{C} \qquad \textbf{2-14}$$

Where C determines the slope of the light intensity dependence of $R_{sc(light)}$ and DD determines the intercept with the J_{sc} axis. This leads to the following relationship:

$$J = -J_{sc} + J_0\left(\exp\left(\frac{eV}{n_{ideal}kT}\right) - 1\right) - \frac{V}{R_{sc(tot)}} \qquad \textbf{2-15}$$

When the shunt resistance of the device is infinitely high, the open circuit voltage is mainly determined by the ideality factor and dark saturation current. The relation is determined from the following equation:

$$eV_{oc} = n_{ideal}kT\ln\left(\frac{J_{sc}}{J_0} + 1\right) \qquad \textbf{2-16}$$

The ideality factor of the device is mainly determined by the slope of the V_{oc} as a function of $\ln\left(\frac{J_{sc}}{J_0}\right)$ given by $n_{ideal}kT$, while the dark saturation current is mainly determining the intercept b by $J_0 = \exp\left(\frac{-eb}{n_{ideal}kT}\right)$. This is represented in Figure 2-VII.

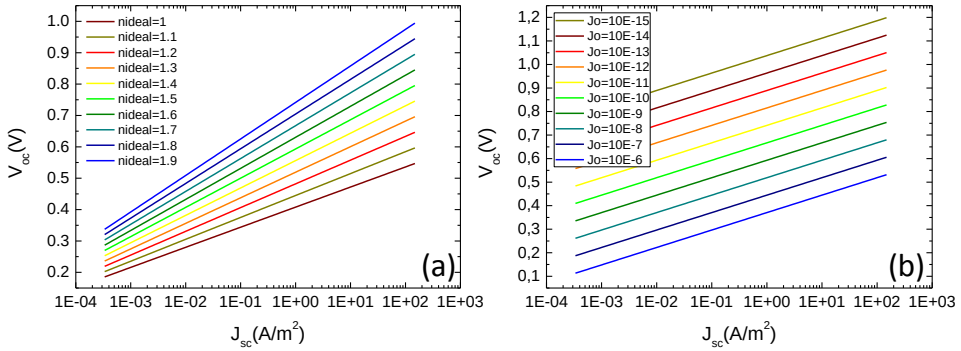

Figure 2-VII: Effects of ideality factor (J_0 =4.25E-7) (a) and dark saturation currents (n_{ideal} = 1.27)(b) on the slopes and intercepts of V_{oc} plots as a function of J_{sc} when short circuit resistance R_{sc} is infinitely high. A colored version of the figure can be found in the electronic version of the thesis.

The effect of R_{sc} on the open circuit voltage for different light intensity is modeled according to the equation below.

$$V_{oc} = J_{sc}R_{sc} - \frac{nkT}{q} LambertW\left(\frac{qJ_0R_{sc}}{nkT} exp\left(\frac{qR_{sc}(J_{sc}+J_0)}{nkT}\right)\right) \qquad \textbf{2-17}$$

Where LambertW is defined as follows: $x = y.\exp(y) \Leftrightarrow y = LambertW(x)$.

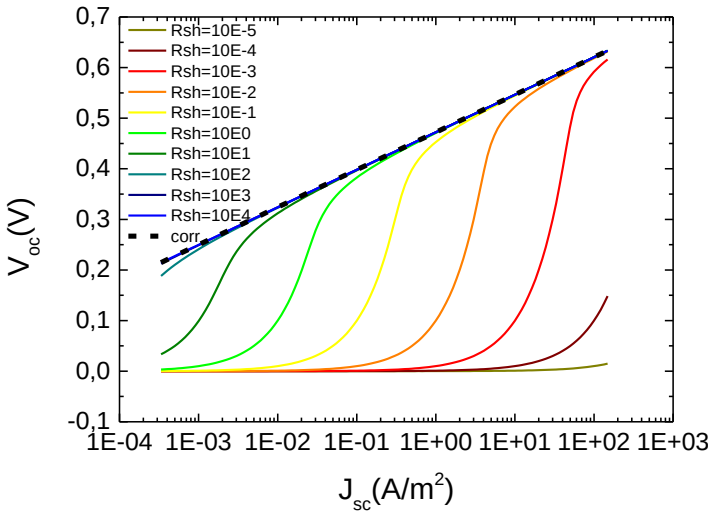

Figure 2-VIII: Effects of dark shunt resistance, or dark short circuit resistance on the relation of V_{oc} plots as a function of J_{sc}. The dashed line represents the relation of V_{oc} plots as a function of J_{sc} after correction for short circuit

resistance. (J_0 =4.25E-7, n_{ideal}= 1.27). A colored version of the figure can be found in the electronic version of the thesis.

Short circuit- or shunt resistances tend to become lower with increased light intensity. The JV-curves should thus be corrected for short circuit resistance before any ideality factor or dark saturation current determination is performed. The short circuit resistance is determined from the slope of the JV-curve around 0V:

$$J(V)_{corr} = J(V)_{uncorr} - \frac{V}{R_{sc(tot)}} \qquad \textbf{2-18}$$

The curves corrected for short circuit resistance are given by the black dotted line.

Due to the correction, a shift in open circuit voltage can be observed given by the following relation:

$$\Delta V_{oc} = V_{oc/corr} - V_{oc/uncorr} \qquad \textbf{2-19}$$

In Figure 2-IX, the effect of the light induced short circuiting on the measured open circuit voltage is shown.

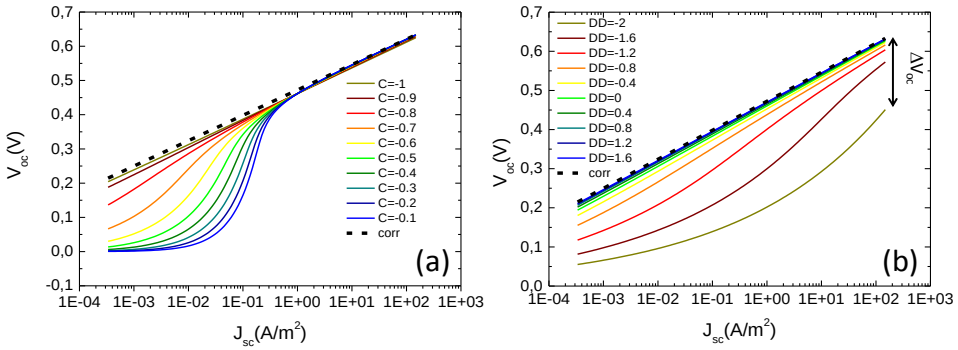

Figure 2-IX: Effects of light intensity dependent shunt resistance parameters on the relation of V_{oc} plots as a function of J_{sc} (Conditions for (a): J_0 =4.25E-7, n_{ideal}= 1.27, R_{sh}=infinite, DD=0.5. Conditions for (b): J_0 =4.25E-7, n_{ideal}= 1.27, R_{sh}=infinite, C=-0.83). The dashed line represents the relation of V_{oc} plots as a function of J_{sc} after correction for short circuit resistance. A colored version of the figure can be found in the electronic version of the thesis.

2.3.5. Charge transport

2.3.5.1. Absence of regional space charge and excessive bimolecular recombination

It has been reported that the imbalance between hole and electron mobilities causes the formation of regional space charge in solar cells [9]. Regional space charge occurs when charge carriers in the device get trapped due to large

imbalances between hole and electron mobilities. This effect becomes very significant if the carrier drift length of holes or electrons becomes smaller than the effective thickness of the device, leading to accumulation of one type of charge carrier in the layer [9]. To study if a space charge is builds up in devices it is possible to investigate the effect of light power P on J_{sc}, which is related to the rate of free charge generation in the device. The relation between the light power P and J_{sc} can be described by a power law, $J_{sc} \propto P^{\alpha}$, where α is a constant. The absence of significant space charge results in α equal to 1. In space charge mode, α can drop down to 0.75. Recent experiments have shown that this effect becomes important if the imbalance between hole and electron mobility is higher than 2 orders of magnitude [9], [10].

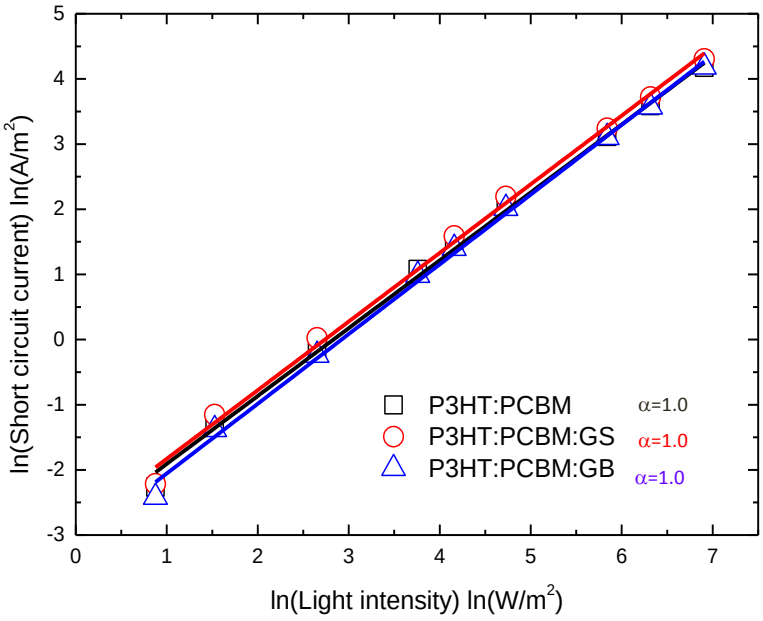

Figure 2-X: J_{sc} as a function of light intensity. The layer composition can be found in Table 2-1.

As can be seen in Figure 2-X, short circuit current increases linearly with light intensity, for the P3HT:PCBM reference cell, as well as for the P3HT:PCBM cell containing graphene centrifuged at low and high centrifugal speeds. The α values measured for the three cells are presented in Table 2-1. Values very close to 1 are measured for all three solar cells, which proves that no significant space charge was formed, and indicates that in none of the devices the ratio between electron and hole mobility was higher than 100. The effect remains the same, even when short circuit resistance was low. Nevertheless, a more limited imbalance between electron and hole mobilities, too low to induce regional space charge, can have a detrimental effect on the solar cells performances due to enhanced charge trapping of electrons at the transparent electrode. To determine if graphene has an impact on the balance between electron and hole

mobilities, charge mobilities have been determined by CELIV and FET-measurements.

2.3.5.2. Electric Charge mobility measurements

Information about electric charge mobility through the layer and in plane of the layer has been obtained by the respective use of CELIV and FET-measurements. Furthermore, drift diffusion simulations were used in order to look into the effects of charge mobility balance on the solar cell parameters.

The basic principle of CELIV is that one applies a linearly increasing voltage. Subsequently one follows electric current transients related to the extraction of charge carriers. The CELIV-data in Figure 2-XI show a decrease of approximately 1 order of magnitude in the ambipolar charge mobility after the addition of graphene flakes centrifuged at high centrifugal speed to the P3HT:PCBM blend [41]. To obtain more information about the cause of this decrease in electric charge carrier mobility, the respective mobilities of electrons and holes should be determined. The field effect transistor electron and hole mobilities have therefore been measured.

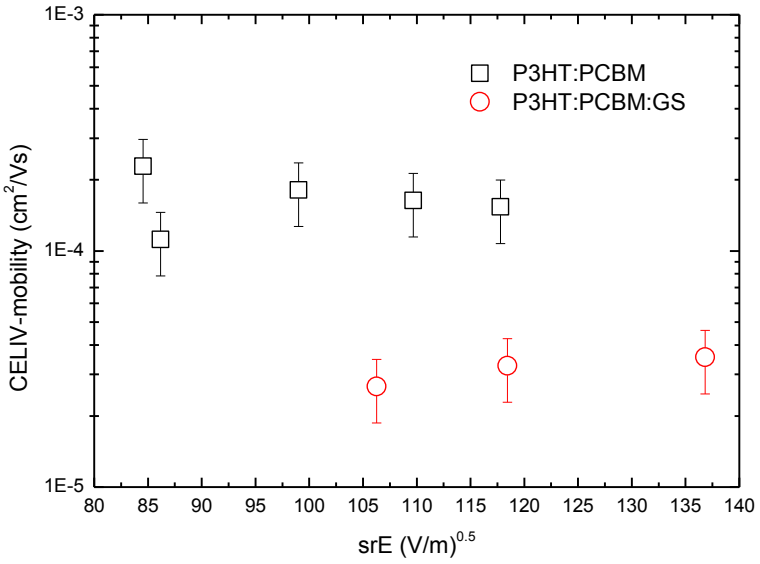

Figure 2-XI: CELIV-mobilities of P3HT:PCBM- and P3HT:PCBM:GS device. The layer composition can be found in Table 2-1.

The results of the FET-measurements are presented in Figure 2-XII. It can be observed that for the reference P3HT:PCBM layer the electron mobility is approximately double than the hole mobility. The addition of small graphene flakes enhances the hole mobility by 30% and reduces the electron mobility by 50%, leading to more balanced hole and electron mobilities. Addition of a higher fraction of larger graphene flakes causes a recovery to the original hole mobility, but the electron mobility remains low compared to the reference layer. The lowest charge mobility in the layer with low graphene fraction (electron mobility) is still higher than the lowest mobility in the reference layer (hole mobility),

which explains why the reduced electron mobility does not lead to deteriorated solar cells performance. A possible explanation for the reduction in electron mobility is that graphene induces disorder in the high efficient electron transport network of PCBM. To understand the evolution of hole mobility with the graphene fraction in the layer, the influence of graphene on crystallinity of P3HT has been investigated by selective area electron diffraction (SAED).

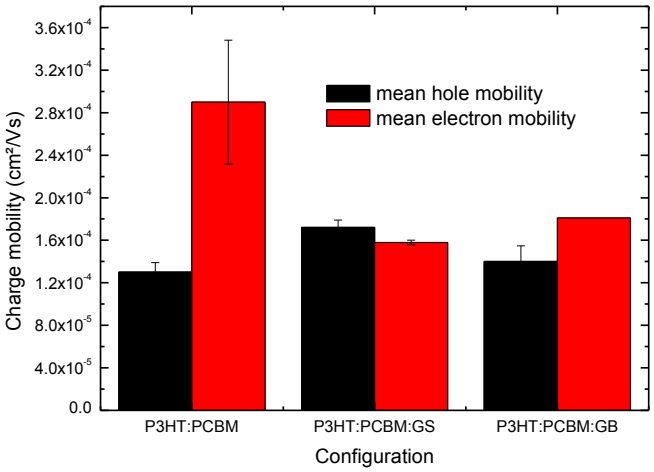

Figure 2-XII: Field effect mobilities for 3 different conditions. The layer composition can be found in Table 2-1.

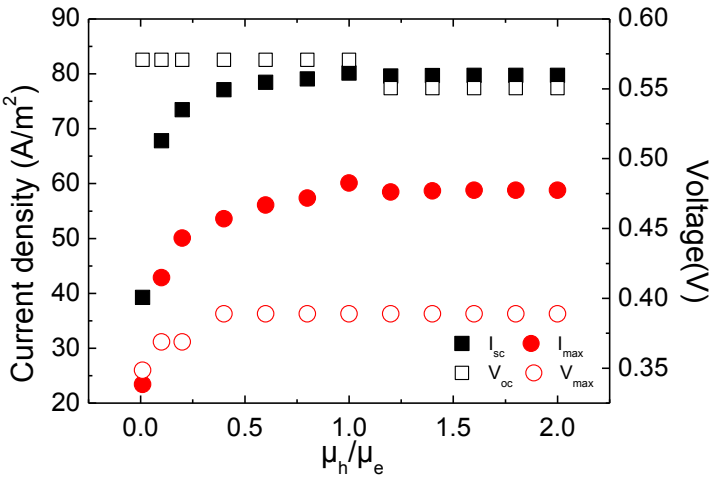

Figure 2-XIII: Effect of solar cell parameters on changing hole mobility compared to the electron mobility. The simulation parameters are: Temperature 300K, Work function Ca/Al 3.41 eV, PEDOT 5.17 eV, LUMO acceptor level 4.1 eV, HOMO donor level 5.15 eV, Generation rate 0.55E28 $cm^{-2}s^{-1}$, Relative permittivity 3.6, Thickness 110 nm.

To support the experimental findings, we carried out simulations based on the two dimensional mathematical grid for charge generation and recombination as for Ref.[42]. We used a direct recombination with the assumption that the charge carrier generation is field independent. The basic bi-molecular recombination type, as described by the Langevin expression [32], [43], was used to describe the recombination kinetics. To show the effect of unbalanced mobility on the current voltage characteristics of P3HT:PCBM solar cells, μ_h was varied between 5*10−5 and 1*10−3 cm2/Vs, while keeping the μ_e constant at 5*10−4 cm2/Vs (see Figure 2-XIII). The most noticeable feature is the increase of J_{sc} and J_{max} (Figure 2-XIII), while μh is below μe. When $\mu_h = \mu_e$, J_{sc} is stable even when μ_h becomes larger than μ_e. The effect of the mobility imbalance on both V_{oc} and V_{max} is less pronounced (Figure 2-XIII) with respect to J_{sc} and J_{max}. These simulations are in good agreement with experimental data.

2.3.6. P3HT crystallinity for different graphene contents

After exciton dissociation, holes percolate in the donor material (P3HT) to the collecting electrode. The crystallinity of P3HT molecules therefore has a strong influence on the hole carrier transport. To get an insight into the influence of graphene on P3HT crystallinity, SAED has been performed on layers with different graphene fractions (Figure 2-XIV). The diffraction ring indicated with the red arrow on each image corresponds to the diffraction pattern of P3HT. It can be seen in Figure 2-XIV (P3HT:PCBM:GS) that when high speed centrifugation graphene is added, this ring is more intense and becomes thinner, indicating a higher crystallinity of P3HT inside the layer. The enhanced crystallinity of P3HT could originate from the organization of P3HT molecules around graphene. This hypothesis is supported by observations made in reference [44], which show the existence of interactions between graphene structures and P3HT molecules. The crystallization of P3HT around molecules presenting a carbon structure close to graphene has also been reported in [45]. The higher crystallinity of P3HT explains the enhancement of hole mobility in layers containing a low fraction of graphene flakes.

When graphene centrifuged at lower centrifugal speeds was added to the blend, the ring becomes more diffuse Figure 2-XIV (P3HT:PCBM:GB)). This is evidence of lower crystallization of P3HT inside the layer. This observation is consistent with results from FET mobility measurements, which have shown a lower hole mobility in the presence of large graphene flakes.

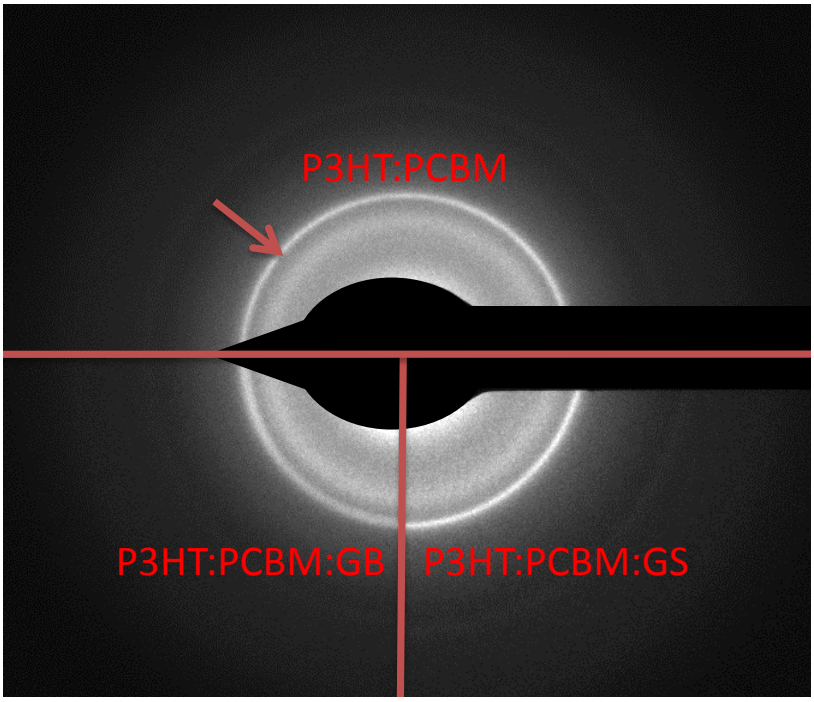

Figure 2-XIV: SAED images for P3HT:PCBM, P3HT:PCBM:GS and P3HT:PCBM:GB. The layer composition can be found in Table 2-1.

2.3.7. Charge carrier recombination

Under open circuit conditions, all photogenerated charge carriers are recombined within the cell. The evolution of the open circuit voltage (V_{oc}) as a function of light intensity gives information about the electric charge carrier recombination mechanism. Electric charge recombination mechanisms can be subdivided into geminate and non-geminate recombination. Geminate recombination occurs when free electric charge carriers recombine before they are trapped in states in a Langevin type fashion, where free electrons and holes are attracted to each other by coulomb forces. When they meet, the electron-hole pair is annihilated. On the other hand trap assisted recombination occurs when free electrons or holes are recombining with counter charge carriers trapped in so called recombination centers. This type of recombination is described by Shokley Reed Hall relations [46].

To investigate the type of recombination in the cell, one can plot the open circuit voltage as a function of the natural logarithm of different light intensities as depicted in Figure 2-XV. The slope of this curve has a universal value of $\frac{n_{ideal} k_b T}{e} ln\left(\frac{J_{sc}}{J_0}\right)$, where n_{ideal} is the ideality factor, J_{sc} is the short circuit current density, J_o the dark saturation current density, k_b is the Boltzmann constant, T is the absolute temperature and e is the unit charge.

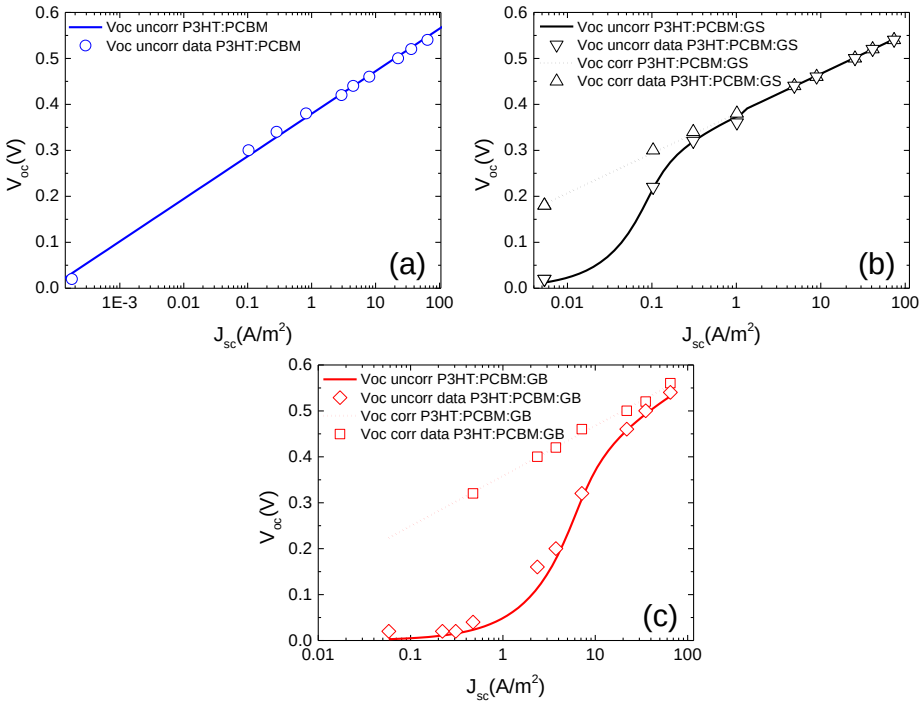

Figure 2-XV: V_{oc} as a function of J_{sc} before (full line) and after (dashed line) correction for short circuit resistance. The layer composition can be found in Table 2-1. For P3HT:PCBM, J_0 =3.81E-5 A/m², n_{ideal}=1.43. For P3HT:PCBM:GS, J_0 =1.67E-5 A/m², n_{ideal}=1.36 and $R_{sc\ (dark)}$=5.2 Ω. For P3HT:PCBM:GB J_0 =0.0012 A/m², n_{ideal}=1.98 and $R_{sc\ (dark)}$=1.6 Ω.

It has been suggested in reference[46] that the type of recombination can be determined using the ideality factor n_{ideal}. This ideality factor can vary from n_{ideal}=1, when the transport is completely determined by bimolecular recombination, to n_{ideal}=2, when the transport is determined by the recombination of free charge carriers with trapped counterparts. In Figure 2-XV it can been seen that for the case of the P3HT:PCBM reference device, the ideality factor is 1.43 and the dark leakage current is close to zero. After addition of low concentrations of small graphene flakes, the ideality factor reduces to 1.36, implying a reduction in the relative importance of trap assisted recombination although the $R_{sc(dark)}$ reduces to values of 5.2Ω. This could be explained by improved balanced charge transport, which reduces the probability of electron trapping, and the higher crystallinity of P3HT, which reduces the probability of holes being trapped by crystal defects during their transport to electrodes. When larger graphene flakes are added to the layer, the ideality factor increases to a value of 1.98, which can be attributed to the lower P3HT crystallinity due to graphene clustering. Further trapping can be caused due to high leakage currents in the device when large graphene clusters are formed (

$R_{sc(dark)}$ =1.6Ω). The procedure for the deconvolution of the different parameters is further explained in chapter 4.

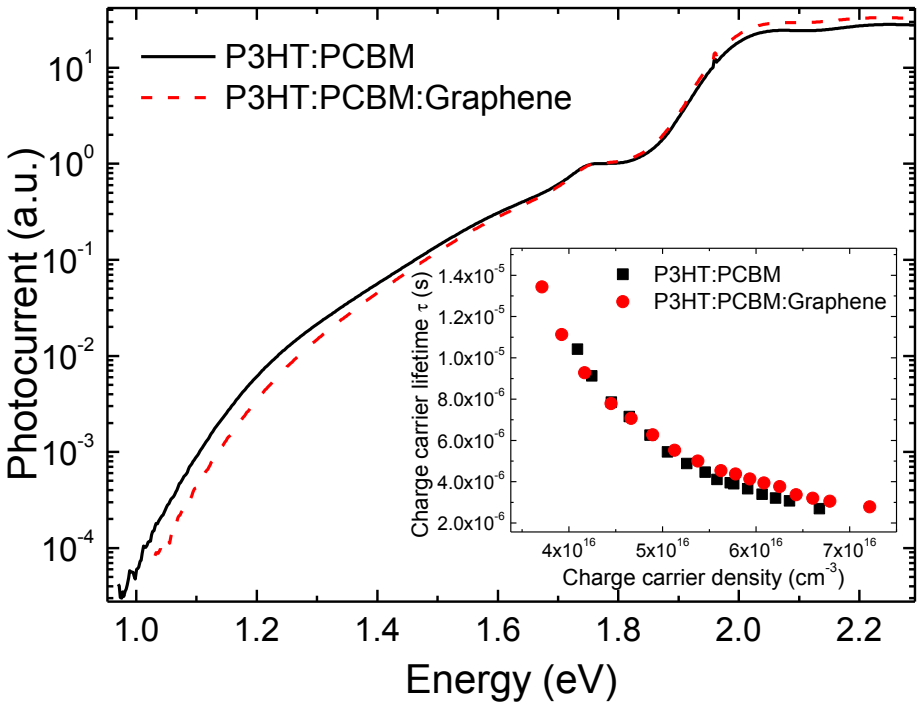

Figure 2-XVI: Photocurrent spectra of solar cells (see Table 2-1) measured by FTPS. The inset shows carrier lifetime as a function of the number of charge carriers extracted from TPV data.

FTPS can be used as a probe for charge transfer occurring in P3HT:PCBM solar cells [47], as depicted in Figure 2-XVI. The photocurrent generation in PCBM (band to band transition) is 1.75 eV, while the onset for free photo carrier generation in P3HT is 1.9 eV [47]. The wide feature in the gap states (see Figure 2-XVI), called the CT-band is ascribed to transitions between the lowest unoccupied molecular orbital (LUMO) of the acceptor and the highest occupied molecular orbital (HOMO) of the donor [47]. After addition of 2 wt% graphene, the FTPS spectra show a blue shift of the CT band by ΔE ~0.1 eV. The gap state reduction might be a reason for the observed change of the electron and hole trapping/recombination kinetics and the μ_h/μ_e ratio.

To investigate charge recombination effects [48], transient photo voltage measurements (TPV) are performed, probing the recombination currents. Figure 2-XVI (inset) shows the recombination lifetime as a function of the charge carrier density. Although a CT blue-shift is seen in the FTPS-spectra (Figure 2-XVI) while V_{oc} remains constant, there is no significant change in the ambipolar charge density or the carrier lifetime [49]. From this data, the recombination coefficient, i.e. the ratio between the number of charge carriers and the recombination lifetime, does not change significantly. This explains the

reduction of the recombination currents. Our data indicates that graphene, as a ternary component, does not decrease the charge carrier density and lifetime, thus keeping V_{oc} unchanged. However, the ideality factors measured in devices are not 1 as seen in Table 2-1, effects of the rate of monomolecular recombination on V_{oc} should be taken into account together with bimolecular recombination effects of the charge transfer energy in order to get a good measure of the charge recombination on V_{oc} .

2.4. Conclusion

In this work we demonstrated that the percolation threshold of graphene in 100 nm P3HT:PCBM layers are achieved at fractions up to 2 wt% centrifuged at 35 krpm causing conductive bridges. Below this percolation fraction graphene leads to an increased photocurrent of ~10 A/m^2 and to an enhanced efficiency from 2,79% for P3HT:PCBM to 3,17% for P3HT:PCBM:Graphene. The main contribution to this increase is due to the balancing of electron and hole mobilities in solar cell devices as demonstrated by FET mobility measurements. Graphene, due to its high electrical conductivity also can act as a bridge structure in BHJs to help avoid charging. The amount and type of the charge transported via graphene bridges depends primarily on the characteristics of the graphene/P3HT interface and graphene doping. The enhancement of hole carrier mobility might be induced by improved P3HT crystallization in the presence of graphene The enhancement in P3HT crystallization was confirmed by SAED patterns of the layer. Optical, atomic force and transmission electron microscopy images have shown that when a limited amount of small graphene flakes was blended into the active layer, small graphene clusters form, which were completely encapsulated and homogeneously spread in the P3HT:PCBM layer. In the case of high fractions of large graphene flakes, big graphene clusters tended to form and puncture the active layer causing higher shunt leakage currents in the devices. Finally, the analysis of V_{oc} dependence on light intensity and TPV measurements has indicated a small decrease of monomolecular recombination in solar cells containing small graphene flakes. Further study of the effects of ternary component materials on the open circuit voltage is necessary for improved understanding of this property in ternary blend solar cells.

References

[1] S.-S. Li, K.-H. Tu, C.-C. Lin, C.-W. Chen, and M. Chhowalla, "Solution-processable graphene oxide as an efficient hole transport layer in polymer solar cells.," *ACS Nano*, vol. 4, no. 6, pp. 3169–3174, 2010.

[2] H. Park, S. Chang, M. Smith, S. Gradečak, and J. Kong, "Interface engineering of graphene for universal applications as both anode and cathode in organic photovoltaics.," *Sci. Rep.*, vol. 3, p. 1581, 2013.

[3] J. T. W. Wang, J. M. Ball, E. M. Barea, A. Abate, J. a. Alexander-Webber, J. Huang, M. Saliba, I. Mora-Sero, J. Bisquert, H. J. Snaith, and R. J. Nicholas, "Low-temperature processed electron collection layers of

graphene/TiO 2 nanocomposites in thin film perovskite solar cells," *Nano Lett.*, vol. 14, pp. 724–730, 2014.

[4] V. Gupta, N. Chaudhary, R. Srivastava, G. D. Sharma, R. Bhardwaj, and S. Chand "Luminscent graphene quantum dots for organic photovoltaic devices.," *J. Am. Chem. Soc.*, vol. 133, no. 26, pp. 9960–3, Jul. 2011.

[5] Y. Li, Y. Hu, Y. Zhao, G. Shi, L. Deng, Y. Hou, and L. Qu, "An electrochemical avenue to green-luminescent graphene quantum dots as potential electron-acceptors for photovoltaics," *Adv. Mater.*, vol. 23, pp. 776–780, 2011.

[6] F. Li, L. Kou, W. Chen, C. Wu, and T. Guo, "Enhancing the short-circuit current and power conversion efficiency of polymer solar cells with graphene quantum dots derived from double-walled carbon nanotubes," *NPG Asia Mater.*, vol. 5, no. 8, p. e60, 2013.

[7] T. Ameri, P. Khoram, J. Min, and C. J. Brabec, "Organic ternary solar cells: A review," *Adv. Mater.*, vol. 25, pp. 4245–4266, 2013.

[8] G. Li, V. Shrotriya, J. Huang, Y. Yao, T. Moriarty, K. Emery, and Y. Yang, "High-efficiency solution processable polymer photovoltaic cells by self-organization of polymer blends," *Nat. Mater.*, vol. 4, no. November, pp. 864–868, 2005.

[9] P. W. M. Blom, V. D. Mihailetchi, L. J. A. Koster, and D. E. Markov, "Device Physics of {Polymer:Fullerene} Bulk Heterojunction Solar Cells," *Adv. Mater.*, vol. 19, no. 12, pp. 1551–1566, 2007.

[10] M. Morana, P. Koers, C. Waldauf, M. Koppe, D. Muehlbacher, P. Denk, M. Scharber, D. Waller, and C. Brabec, "Organic Field-Effect Devices as Tool to Characterize the Bipolar Transport in Polymer-Fullerene Blends: The Case of {P3HT-PCBM}," *Adv. Funct. Mater.*, vol. 17, no. 16, pp. 3274–3283, Nov. 2007.

[11] J. S. Kim, J. H. Lee, J. H. Park, C. Shim, M. Sim, and K. Cho, "High-Efficiency Organic Solar Cells Based on Preformed Poly(3-hexylthiophene) Nanowires," *Adv. Funct. Mater.*, vol. 21, no. 3, pp. 480–486, Feb. 2011.

[12] S. Günes, H. Neugebauer, and N. S. Sariciftci, "Conjugated Polymer-Based Organic Solar Cells," *Chem. Rev.*, vol. 107, no. 4, pp. 1324–1338, Apr. 2007.

[13] "Datasheet Dichlorobenzene." http://pubchem.ncbi.nlm.nih.gov/compound/1_2-dichlorobenzene#section=Top

[14] Y. Hernandez, V. Nicolosi, M. Lotya, F. M. Blighe, Z. Sun, S. De, I. T. McGovern, B. Holland M. Byrne, Y. K. Gun'Ko, J. J. Boland P. Niraj, G. Duesberg, S. Krishnamurthy, R. Goodhue, J. Hutchison, V. Scardaci, A. C. Ferrari, and J. N. Coleman, "High-yield production of graphene by liquid-phase exfoliation of graphite," *Nat. Nanotechnol.*, vol. 3, no. 9, pp. 563–568, Sep. 2008.

[15] F. Bonaccorso, A. Lombardo, T. Hasan, Z. Sun, L. Colombo, and A. C. Ferrari, "Production and processing of graphene and 2d crystals," *Mater. Today*, vol. 15, no. 12, pp. 564–589, Dec. 2012.

[16] T. Hasan, F. Torrisi, Z. Sun, D. Popa, V. Nicolosi, G. Privitera, F. Bonaccorso, and a. C. Ferrari, "Solution-phase exfoliation of graphite for ultrafast photonics," *Phys. Status Solidi Basic Res.*, vol. 247, pp. 2953–2957, 2010.

[17] F. Torrisi, T. Hasan, W. Wu, Z. Sun, A. Lombardo, T. S. Kulmala, G.-W. Hsieh, S. Jung, F. Bonaccorso, P. J. Paul, D. Chu, and A. C. Ferrari, "Inkjet-Printed Graphene Electronics," *{ACS} Nano*, vol. 6, no. 4, pp. 2992–3006, Apr. 2012.

[18] O. M. Maragó, F. Bonaccorso, R. Saija, G. Privitera, P. G. Gucciardi, M. A. Iatì, G. Calogero, P. H. Jones, F. Borghese, P. Denti, V. Nicolosi, and A. C. Ferrari, "Brownian Motion of Graphene," *{ACS} Nano*, vol. 4, no. 12, pp. 7515–7523, Dec. 2010.

[19] J.-C. Bolsée and J. Manca, "Effects of hole and electron trapping on organic field-effect transistor transfer characteristic," *Synth. Met.*, vol. 161, no. 9–10, pp. 789–793, May 2011.

[20] a. J. Mozer, N. S. Sariciftci, L. Lutsen, D. Vanderzande, R. Österbacka, M. Westerling, and G. Juška, "Charge transport and recombination in bulk heterojunction solar cells studied by the photoinduced charge extraction in linearly increasing voltage technique," *Appl. Phys. Lett.*, vol. 86, no. 11, p. 112104, 2005.

[21] K. Vandewal, L. Goris, I. Haeldermans, M. Nesládek, K. Haenen, P. Wagner, and J. V Manca, "Fourier-Transform Photocurrent Spectroscopy for a fast and highly sensitive spectral characterization of organic and hybrid solar cells," *Thin Solid Films*, vol. 516, no. 20, pp. 7135–7138, Aug. 2008.

[22] A. C. Ferrari and J. Robertson, "Origin of the 1150-cm-1 Raman mode in nanocrystalline diamond," *Phys. Rev. B*, vol. 63, no. 12, p. 121405, Mar. 2001.

[23] A. C. Ferrari, J. C. Meyer, V. Scardaci, C. Casiraghi, M. Lazzeri, F. Mauri, S. Piscanec, D. Jiang, K. S. Novoselov, S. Roth, and A. K. Geim, "Raman

Spectrum of Graphene and Graphene Layers," *Phys. Rev. Lett.*, vol. 97, no. 18, p. 187401, Oct. 2006.

[24] F. Tuinstra and J. L. Koenig, "Raman Spectrum of Graphite," *J. Chem. Phys.*, vol. 53, no. 3, pp. 1126–1130, Aug. 1970.

[25] C. Casiraghi, A. Hartschuh, E. Lidorikis, H. Qian, H. Harutyunyan, T. Gokus, K. S. Novoselov, and A. C. Ferrari, "Rayleigh Imaging of Graphene and Graphene Layers," *Nano Lett.*, vol. 7, no. 9, pp. 2711–2717, Sep. 2007.

[26] A. C. Ferrari and J. Robertson, "Interpretation of Raman spectra of disordered and amorphous carbon," *Phys. Rev. B*, vol. 61, no. 20, pp. 14095–14107, May 2000.

[27] S. Bertho, W. D. Oosterbaan, V. Vrindts, J. C. Bolsée, F. Piersimoni, D. Spoltore, J. D'Haen, L. Lutsen, D. Vanderzande, and J. V. Manca, "Poly(3-alkylthiophene) Nanofibers for Photovoltaic Energy Conversion," *Adv. Mater. Res.*, vol. 324, pp. 32–37, 2011.

[28] M. Manceau, A. Rivaton, J. L. Gardette, S. Guillerez, and N. Lemaître, "Light-induced degradation of the P3HT-based solar cells active layer," *Sol. Energy Mater. Sol. Cells*, vol. 95, pp. 1315–1325, 2011.

[29] M. T. Dang, G. Wantz, H. Bejbouji, M. Urien, O. J. Dautel, L. Vignau, and L. Hirsch, "Polymeric solar cells based on {P3HT:PCBM:} Role of the casting solvent," *Sol. Energy Mater. Sol. Cells*, vol. 95, no. 12, pp. 3408–3418, Dec. 2011.

[30] R. a. Street, M. Schoendorf, a. Roy, and J. H. Lee, "Interface state recombination in organic solar cells," *Phys. Rev. B*, vol. 81, no. 20, p. 205307, May 2010.

[31] K. Vandewal, K. Tvingstedt, A. Gadisa, O. Inganäs, and J. V Manca, "On the origin of the open-circuit voltage of polymer-fullerene solar cells.," *Nat. Mater.*, vol. 8, no. 11, pp. 904–909, 2009.

[32] L. J. A. Koster, M. Kemerink, M. M. Wienk, K. Maturová, and R. a J. Janssen, "Quantifying bimolecular recombination losses in organic bulk heterojunction solar cells," *Adv. Mater.*, vol. 23, pp. 1670–1674, 2011.

[33] L. Liu and G. Li, "Investigation of recombination loss in organic solar cells by simulating intensity-dependent currentvoltage measurements," *Sol. Energy Mater. Sol. Cells*, vol. 95, no. 9, pp. 2557–2563, 2011.

[34] J. K. Kraus, *Physics of Molecular Donor-acceptor Solar Cells: Correlation Between Interface Morphology, Energetics and Device Performance*. 2013.

[35] J. R. Tumbleston, Y. Liu, E. T. Samulski, and R. Lopez, "Interplay between bimolecular recombination and carrier transport distances in bulk heterojunction organic solar cells," *Adv. Energy Mater.*, vol. 2, pp. 477–486, 2012.

[36] J. D. Servaites, M. a. Ratner, and T. J. Marks, "Organic solar cells: A new look at traditional models," *Energy Environ. Sci.*, vol. 4, p. 4410, 2011.

[37] R. S. Crandall, "Modeling of thin film solar cells: Uniform field approximation," *J. Appl. Phys.*, vol. 54, no. 1983, pp. 7176–7186, 1983.

[38] C. Voz, J. Puigdollers, J. M. Asensi, S. Galindo, S. Cheylan, R. Pacios, P. Ortega, and R. Alcubilla, "Analysis of the dynamic short-circuit resistance in organic bulk-heterojunction solar cells: Relation to the charge carrier collection efficiency," *Org. Electron. physics, Mater. Appl.*, vol. 14, no. 6, pp. 1643–1648, 2013.

[39] J. C. Blakesley and D. Neher, "Relationship between energetic disorder and open-circuit voltage in bulk heterojunction organic solar cells," *Phys. Rev. B - Condens. Matter Mater. Phys.*, vol. 84, 2011.

[40] T. Kirchartz and J. Nelson, "Meaning of reaction orders in polymer:fullerene solar cells," *Phys. Rev. B - Condens. Matter Mater. Phys.*, vol. 86, pp. 1–12, 2012.

[41] J. Lorrmann, B. H. Badada, O. Inganäs, V. Dyakonov, and C. Deibel, "Charge carrier extraction by linearly increasing voltage: Analytic framework and ambipolar transients," *J. Appl. Phys.*, vol. 108, no. 11, p. 113705, Dec. 2010.

[42] K. Maturová, S. S. van Bavel, M. M. Wienk, R. A. J. Janssen, and M. Kemerink, "Description of the Morphology Dependent Charge Transport and Performance of Polymer:Fullerene Bulk Heterojunction Solar Cells," *Adv. Funct. Mater.*, vol. 21, no. 2, pp. 261–269, Jan. 2011.

[43] A. Pivrikas, G. Juska, T. Osterbacka, M. Westerling, M. Vilionas, K. Arlauskas, and H. Stubb, "Langevin recombination and space-charge-perturbed current transients in regiorandom poly(3-hexylthiophene)," *Phys. Rev. B*, vol. 71, no. 12, p. 125205, Mar. 2005.

[44] A. Chunder, J. Liu, and L. Zhai, "Reduced Graphene Oxide/Poly(3-hexylthiophene) Supramolecular Composites.," *Macromol. Rapid Commun.*, vol. 31, no. 4, pp. 380–4, Feb. 2010.

[45] L. Bu, E. Pentzer, F. A. Bokel, T. Emrick, and R. C. Hayward, "Growth of {Polythiophene/Perylene} Tetracarboxydiimide {Donor/Acceptor} Shish-Kebab Nanostructures by Coupled Crystal Modification," *{ACS} Nano*, vol. 6, no. 12, pp. 10924–10929, Dec. 2012.

[46] S. R. Cowan, A. Roy, and A. J. Heeger, "Recombination in polymer-fullerene bulk heterojunction solar cells," no. July, pp. 1–10, 2010.

[47] K. Vandewal, K. Tvingstedt, A. Gadisa, O. Inganäs, and J. V Manca, "On the origin of the open-circuit voltage of polymer–fullerene solar cells," *Nat. Mater.*, vol. 8, no. 11, pp. 904–909, Nov. 2009.

[48] A. Maurano, C. G. Shuttle, R. Hamilton, A. M. Ballantyne, J. Nelson, W. Zhang, M. Heeney, and J. R. Durrant, "Transient optoelectronic analysis of charge carrier losses in a selenophene/fullerene blend solar cell," *J. Phys. Chem. C*, vol. 115, pp. 5947–5957, 2011.

[49] K. R. Graham, P. Erwin, D. Nordlund, K. Vandewal, R. Li, G. O. Ngongang Ndjawa, E. T. Hoke, A. Salleo, M. E. Thompson, M. D. McGehee, and A. Amassian, "Re-evaluating the role of sterics and electronic coupling in determining the open-circuit voltage of organic solar cells," *Adv. Mater.*, vol. 25, pp. 6076–6082, 2013.

Chapter 3 Built-in metal grid structures in BNCD as transparent electrodes for PLED applications

3.1. Introduction

This chapter describes the development of a new type of transparent electrode based on boron doped nanocrystalline diamond (BNCD) with an integrated gold (Au) grid. This is a step towards stable alternatives for indium tin oxide (ITO) with high electrical conductivity. The necessity for the search for alternatives for ITO is due to the fact that indium is a rare and expensive element [1]. Indium also has the tendency to diffuse into the active layers of organic photovoltaic devices [2]. The first part of this chapter is devoted to the preparation of electrodes. In the second part, the electrical properties of BNCD layers with embedded grids are measured by 4-point measurements based on the van der Pauw configuration. These resistance measurements are related to the electrode optical transparency. Transparency changes are further investigated by transmission, reflection, absorption measurements and modelled in order to obtain the real and imaginary part of the refractive index of the layer. Furthermore, PLED-devices are fabricated and characterized in order to demonstrate the applicability of the BNCD/Cr:Au electrodes for charge extraction and -injection. In the next chapter, the application of BNCD/Cr:Au electrodes with P3HT:PCBM solar cell devices is discussed further.

The chapter outline is as follows:

- In the introduction we discuss BNCD layer properties relevant for construction of transparent electrodes for organic photovoltaics and organic LEDs.
- The experimental section is divided as follows:
    - An extended description of electrode fabrication
    - P-LED preparation
    - Sheet resistance measurements of BNCD:Cr/Au electrodes
    - Scanning electron microscopy
    - Transmission measurements and detailed optical characterization of transparent electrodes
- The result section shows
    - Optical microscopy results
    - Transmission and sheet resistance data
    - Detailed optical description and modelling of the optical data.
    - PLED-device characterization

The innovative concept described in this chapter is based on a hybrid electrode consisting of BNCD layers and a gold-grid which leads to highly transparent and low resistive electrodes which are compatible with OPV and PLEDs.

Since the discovery of Organic Light-Emitting Diodes (OLEDs) [3] and PLEDs [4], Indium Tin Oxide (ITO) has been used as a transparent electrode as part of the OLED and PLED device architecture utilizing ITO's high conductivity and transparency[5].

An important subgroup of frequently used semiconductors used as transparent electrode materials are metal oxides consisting of a lattice of tin oxide (SnO_2). In the SnO_2 lattice, fluorine (FTO) or indium (ITO) can be incorporated leading to highly conductive transparent materials [6]. ITO/FTO possess, like all tin oxides, low thermal conductivity which makes it less useful in applications where

local heat removal is important [7]. This thermal instability remains an important issue due to joule heating during operation conditions [8]. The index of refraction of the electrode is important for light output of OLED applications, determining the critical angle between the OLED polymer layer and the substrate. The critical angle is the angle above which total internal reflection occurs. This angle should thus be as high as possible. This is necessary to maximize the amount of light that is coupled into the environment. The refractive index of diamond is higher than that of tin oxide films and matches values of used organic polymers [9]–[11]. Layers with gradual decreasing refractive indices between that of diamond and glass can be used to optimize the light out coupling toward the surrounding.

In recent years, carbon-based materials have also been investigated for their use as transparent electrode to replace ITO. An important research direction, as already discussed, was using graphene [12]–[15], but also the potential of diamond has been investigated for its use as a transparent electrode [16]–[18].

B-doping is an effective pathway for the reduction of NCD resistivity. However, after high B-doping (5000 ppm B /C in the gas phase during the CVD diamond preparation) of NCD, the intrinsic sheet resistance remains high (~2 kΩ/sqr) compared to metal oxide electrodes (~20 Ω/sqr). However, this problem can be overcome by utilizing a low resistant metal mesh [19]. By the use of electrodes consisting of metal grids embedded in a semiconducting layer, a decoupling of conductivity and transparency loss can be reached [20]. In general, thin metal films have an intrinsic low transparency. To increase film transparency films can be patterned into grids with openings, or pitches. The conductivity of the metal grid can be improved by increasing the thickness of the metal layer. This has no effect on the transparency of the layer if the pitch size remains constant. Selective conductivity of the pitch can be obtained by filling the pitch with a selective hole or electron conductor. In the past, transparent conductors have been used to fill the pitch to homogenize the charge collection. Previously used transparent conductors grids were used with highly conductive PEDOT:PSS [21] and graphene [22], [23]. Similar effects were obtained by using metal nanowire systems embedded in PEDOT:PSS [24], [25]. The choice of the metallization pattern shape has been investigated intensively in recent years. Geometric patterns have been used ranging from linear [26] and hexagonal mesh electrodes [21] to spiral ones to optimize charge distribution while keeping transparency at a maximum [26]. Finite element optimization indicates that leaf and nerve like patterns can be an even more optimal option [27].

When metal grids are used in hybrid transparent electrodes, the grid induces a surface roughness, which causes high local electric field gradients and consequently short-cuts of the polymer layers of the device. To increase the compatibility of ultra-thin organic layers (thickness around 100 nm) with BNCD layers with a built-in metallic grid, a careful choice of strategy, techniques and materials is necessary. Gold was chosen in this work since it has a very low contact resistance in combination with BNCD diamond [28], [29] and the polymers used in solar cells [30]. In addition to high charge transport, good adhesion is necessary between the layers to create stable electrodes. Since gold by itself has a low adhesion affinity to diamond, carbide forming materials can be used to enhance the adhesion between gold and BNCD layers [31], [32].

Further, thermal stability of the contact adhesion is possible by the use of an anti-diffusion layer, such as platinum, between the carbide forming material and the gold layer [33].

For easier fabrication and processing chromium is used as a carbide forming adhesion layer in this work. Therefore, the electric contact between the grid and diamond was improved, leading to low sheet resistance. To create electrodes for preparation of highly efficient solar cells, we anticipated that embedding the electrode layer into the p-type layer might increase the device performance [21], [34].

Another important problem tackled in this section is the optical transparency of BNCD electrodes. By performing analysis of the optical properties expressed by the complex index of refraction n+ik [35], [36]. The optical properties of thin films on transparent substrates are characterized by the optical transmittance T, reflectance R, and absorptance A spectroscopies [35]. The salient feature of the low-absorbing thin film with thickness d is the presence of the interference fringes in the optical spectra which depend on d(n+ik) product and via n(λ)+ik(λ) are related to the wavelength λ of the incident light. Thicker films give a shorter period of interferences (i.e. increased maxima and minima for a given wavelength range than thinner films) and the maxima and minima are closer together than for thinner films.

In order to decrease the sheet resistance of the BNCD layers towards values comparable to the standard ITO-devices, a method is developed to build in a gold grid into BNCD layers. For proof of principle, we used a square grid. [37]. With BNCD/Cr:Au grid electrodes PLEDs were prepared to study device properties, electroluminescent emission (EL) and J-V response. Identical ITO electrode reference PLEDs were prepared for comparison. P3HT:PCBM solar cells based on BNCD:Cr/Au electrodes perform in a similar fashion compared to their ITO-based counterparts. For BNCD-Cr/Au PLEDs a higher current density and luminance flux is observed in comparison to ITO electrode PLEDs.

3.2. Experimental section

3.2.1. Electrode preparation

In this section, the procedure for embedding an Au-grid into a BNCD layer via a series of different steps including photolithography, solution processing and vacuum deposition is described. The outline of the procedure is described in Figure 3-1.

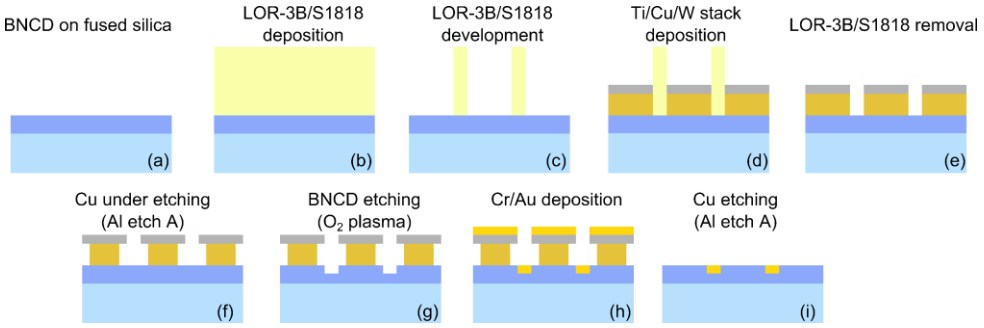

Figure 3-I: Steps for sample preparation. List of abbreviations: Lift off resist (LOR), positive resist (S1818)

First a BNCD layer was grown on a fused silica substrate (Figure 3-I (a)). To embed the Cr/Au lines in the diamond, grid pattern in the form of a LOR3B lift-off resist and a S1818 positive photolithography photoresist on top of the BNCD layer (Figure 3-I (b-c)) was deposited. A sputtered metal stack, consisting of a carbide forming Ti adhesion layer (20 nm), a sacrificial Cu layer (400 nm) and an oxygen-plasma protection W-layer (100 nm) (Figure 3-I (d)), was deposited on the patterned BNCD surface. The adhesion-, sacrificial- and oxygen protection materials were chosen in order that wet etching of the sacrificial layer does not influence the morphology of the oxygen plasma protection layer [39,40]. After removal of the photoresist (Figure 3-I (e)), the sacrificial Cu-layer was under etched by the use of Al etch A (80% H_3PO_4+5%HNO_3+5%HAc+10%H_20) [38] in order to create a lift-off structure (Figure 3-I (f)). The negative of the metal pattern, and thus the final grid pattern was etched into the BNCD-layer by the use of an oxygen plasma (Figure 3-I (g)). After these two etching steps, the pattern was filled with Cr/Au by thermal evaporation, the etched pits were filled up at the height of the BNCD-surface (Figure 3-I (h)). The Cr/Au layer deposited on top of the protective metal stack was removed by etching away the remaining sacrificial and adhesion layer leaving the Cr/Au layer embedded in the BNCD-layer (Figure 3-I (i)). An overview of the different layers and their function used in this work is given in Table 3-1. An overview of the chemicals used are displayed in Table 3-2. In the following sections we discuss the process in greater detail.

Prior to BNCD diamond growth on fused silica substrates, substrates were cleaned using RCA1 and RCA2 cleaning techniques. Afterwards, the samples were immersed in a suspension of 4 nm Bucky Diamond diluted to 0.33 g/L for 1 min and then spincoated at 4000 rpm with water sprayed on top in order to obtain uniform surface coverage. BNCD layers were subsequently grown in an Astex AX6550 microwave plasma enhanced chemical vapor deposition system with the following conditions, base pressure < 2.6E-8 Bar, working pressure: 2.6E-2 Bar, microwave power: 3500 W and substrate stage heated by plenum on the underside of the puck. Growth time was typically 2 hours. Flow rates were 380 sccm H_2, 20 sccm CH_4, 100 sccm TMB (TMB is diluted with H_2), so the methane composition was 4%, and the boron to carbon ratio was 5000 ppm. The sample preparation has been described in Figure 3-1. The above stated conditions were used to grow an 80 nm thick BNCD layer on a fused silica substrate (Figure 3-I (a)). The growth parameters are summarized in Table 3-3.

Table 3-1: In the first column the material layers used in the lithography process is given. The layer functions are shown in the second column.

Layer material	Layer function
S1818	Positive photoresist to pattern the BNCD-layer with the same geometry as the metal grid.
LOR-3B	Used in order to enable S1818 lift-off compatible
Ti-layer	Metal layer with greater adhesion for both BNCD and copper
Cu-layer	Sacrificial Cu layer needed to create a lift-off structure for Cr-Au patterning in combination with W-layer
W-layer	• O_2-plasma protection layer to enable patterning of BNCD • Upper part of the lift-off structure needed for Cr/Au deposition in the patterned parts of the BNCD-layer

Table 3-2: In the first column the chemicals used in the lithography process are stated. The function of the chemicals are shown in the second column.

Chemical	Function
TMAH	Developer for pattern development in S1818-LOR3 resist
Acetone	First removal step to remove metal from the top of S1818
Remover PG	Complete removal of S1818 from the grid lines
Al etchant	Removal of the sacrificial copper layer and adhesion Ti-layer

Table 3-3: Growth conditions for BNCD-layer growth.

Growth parameter	Value
4 nm –Bucky diamond suspension concentration	0.33 g/L
Spincoat speed	4000 rpm
Base pressure	2.6E-8 Bar
Working pressure	2.6E-2 Bar
Microwave power	3500 W
Growth time	2h00
Gas composition	380 sccm H_2, 20 sccm CH_4, 100 sccm TMB
Boron to carbon ratio	5000 ppm
Final film thickness	80 nm

A polymer mask for metal stack patterning was prepared by positive resist lithography using S1818 (Shipley) as a photoresist. Substrates were annealed at

195°C for 5 min. Since the S1818 edge after patterning is without an undercut, it is not usable as a lift-off resist. Therefore, a lift-off resist (LOR-3B) (Microchem) was used to make a lift off structure of S1818 possible during the development. The LOR-3B layer was deposited by spin coating at a speed of 2000 rpm for 45 s as shown in Figure 3-I (b). The samples were baked at 195°C for 5 minutes. Afterwards a layer of S1818 was deposited by spin coating at 3000 rpm for 30 s. After a second baking step at 125°C for 1 min, the polymer layer was patterned using lithography. After lithography, the sample was developed using a 1:10 water:TMAH solution for 40 s. The final photoresist pattern was a negative of the final electrode shape as shown in Figure 3-I (c).

After patterning, 20 nm of Ti was deposited by sputtering to act as an adhesion enhancer between the Cu layer and BNCD. For Ti sputtering a reactive direct current (DC)-pulsed magnetron sputtering system was used with the sample positioned at 12 cm from the anode. Ti was deposited at 150 W for 1 min in a 50 sccm Ar flow at a base pressure below 5E-6 mBar and a working pressure of 4.3E-3 mBar. Afterwards a 400 nm Cu layer was deposited by the use of a Balzers uniun Med 010 system. The Cu layer was deposited for 100 min at 50 mA and a working pressure of 5E-2 mBar. Subsequently, a 100 nm W layer was deposited as described in Figure 3-I (d). W was sputtered with a reactive DC-pulsed magnetron sputtering system with the sample positioned at 12 cm from the anode. W was deposited at 150 W for 6 min in a 50 sccm Ar flow at a base pressure below 5E-6 mBar and a working pressure of 4.3E-3 mBar.

After W deposition, photoresist was removed from the substrate by rinsing the sample in acetone resulting in the structure given in Figure 3-I (e). To be sure that all the SU8/LOR-3B is removed, the sample was soaked in Remover PG at 60°C for 20 min.

The sample was dipped in Aluminum etchant A to etch the Cu under the W-layer to produce a lift off structure (Figure 3-I (f)). This was necessary to be able to remove the W-layer covered with Cr and Au after deposition. This effect was optimized by investigating the front and back side of the sample by optical transmission microscopy. A typical undercut after 5 s of etching is around 0.5 µm as shown in Figure 3-II.

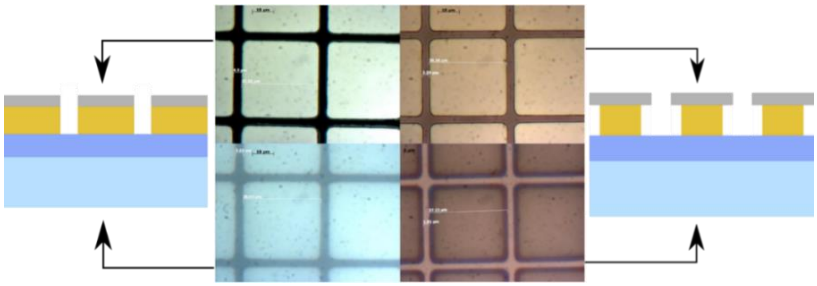

Figure 3-II: Center: Light microscopy images of Cu-W grid before (left) and after (right) under etching of the Cu layer to produce a lift off structure. Sides: Cross sectional schematic representation of the patterned metal layers before (left) and after (right) Cu etching.

The patterned samples were then treated using an oxygen plasma (150 W 50% valve 50 sccm O_2) for 2.5 minutes to etch away BNCD as shown in (Figure 3-I (g)). In order to evaluate the BNCD etch rate the pitch depth was measured by DEKTAK before and after the oxygen plasma treatment. This thickness measurement was performed at several positions on the sample. A typical result is shown in Figure 3-III where the dashed blue line is the dektak-profile after oxygen plasma etching and the full orange line is the dektak-profile before oxygen plasma etching.

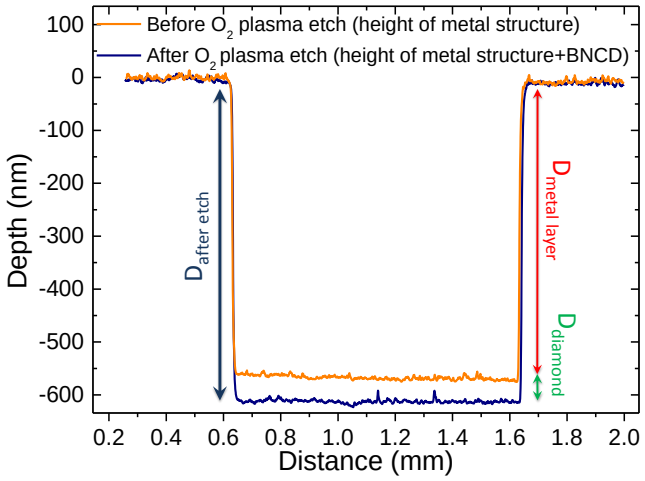

Figure 3-III: Height difference before and after BNCD etching.

Finally, Cr/Au was deposited using the Ti-Cu-W negative as a mold for the metal grid (Figure 3-I (h)) and Cu was etched away by aluminum etchant A leaving the Cr/Au structure (Figure 3-I (i)).

3.2.2. Substrate cleaning

Prior to the PLEDs preparation BNCD/Cr:Au substrates and indium tin oxide (ITO) coated (100 nm) glass substrates (Kintec, sheet resistivity 20 Ω/sqr) were exposed to an ultrasonic bath cleaning procedure of 30 min in soap solution, 10 min in demineralized water, 10 min in acetone and 10 min in isopropanol, followed by a UV/O_3-treatment for 15 min. Following the cleaning procedure poly(3,4-ethylenedioxythiophene):poly(styrenesulfonate) PEDOT:PSS was spin coated at ambient atmosphere to form a layer of ~35 nm. The PEDOT:PSS covered substrates were then annealed in an inert atmosphere (N2) at 120 °C for 10 min.

3.2.3. Preparation of PLED devices

In order to prepare the active layer of the PLED devices SuperYellow (Merck), a poly-(p-phenylenevinylene) derivate, on BNCD electrodes was used. After the samples had cooled down to room temperature a layer of ~80 nm of SuperYellow, was spin coated in an inert atmosphere from 5 mg/ml SuperYellow –Chlorobenzene solution. The SuperYellow solution was prepared in an inert atmosphere and stirred overnight. On top of the SuperYellow a layer of ~30 nm Ca and ~80 nm Al was thermally evaporated at a pressure of ~10E-6 Bar. Devices were characterized by measuring the current density (J) as a function of applied bias voltage (V) while simultaneous measuring the total luminous flux (Φ). The J-V measurements were performed using a Keithley 2401 source meter and the Φ was measured on a calibrated integrating sphere – spectrometer setup from Avantes.

3.2.4. Opto-electrical characterization of transparent electrodes

Optical microscopy was performed with a Zeiss Axiovert 40 MAT at 1000x magnification. The sheet resistance of films was measured using a digital multimeter (Keithley 2400) with a four-point probe configuration to eliminate contact resistance. The transmission of the samples was measured using a solar simulator Newport Oriel class A, equipped with a Xenon Short Arc lamp with 150 W power (1 sun at 1.5 air mass density, i.e. 100 mW/cm^2). The transmitted signal was recorded using a photodiode coupled to a Keithley 2400.

Light absorption was determined by photo thermal deflection spectroscopy (PDS) using 13Hz chopped monochromatic light over the energy range of 0.7–4 eV originating from a 150 W xenon arc lamp. During the measurement, the sample was immersed in Florinert FC72. Transmitted and reflected light from the sample was collected using an integrated sphere. The signal from the detectors was coupled via the multiplexer Signal Recovery 3830 to the current preamplifier and a lock-in amplifier referenced to the chopper frequency.

The analysis of optical properties expressed by the dielectric function or the complex index of refraction n+ik has been the subject of previous studies [35], [39]. Among the widely used methods to investigate the optical properties of thin films on transparent substrates are optical transmittance T, reflectance R and absorptance A spectroscopy [40]. The salient feature of low-absorbing thin films with thickness d is the presence of interference fringes in the optical spectra which depend on d(n+ik) product and via $n(\lambda)+ik(\lambda)$ are related to the wavelength λ of the incident light. Thicker films give more maxima and minima in a given wavelength range than thinner films, and the maxima and minima are closer together than for thinner films. On the other hand ultrathin films are unique in the absence of interference fringes.

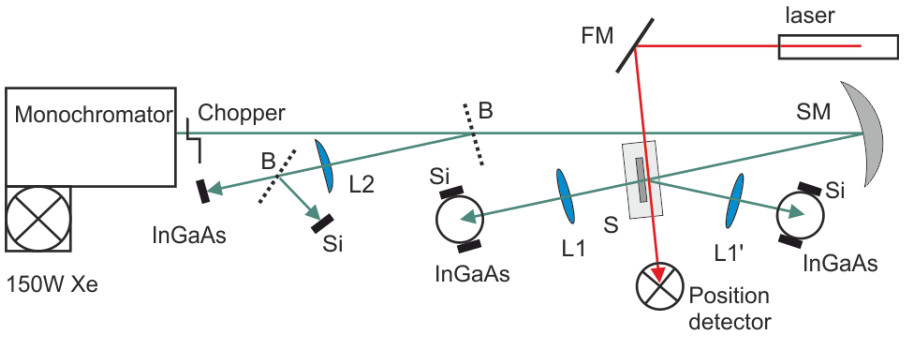

Figure 3-IV: Photo thermal deflection spectroscopy (PDS) setup. 150 W Xe lamp and monochromator as a monochromatic light source, mechanical chopper (Ch), He-Ne laser as a probe beam source, beamsplitter (B), spherical mirror (SM), flat mirror (FM), detectors Si and InGaAs attached to the integrating sphere, focusing lenses (L1-4), position detector (PD) and sample (S) immersed in liquid.

The PDS setup is shown in Figure 3-IV. The sample is immersed in a transparent liquid (Florinert FC72) and periodically illuminated by a monochromatic light from a 150 W Xe lamp with a monochromator with ultraviolet, visible and infrared gratings and a chopper operating at a low frequency of 13Hz. About 8% of the light is deflected by the beam splitter into the integrating sphere equipped with Si and InGaAs photodiodes to monitor the light intensity. This compound detector can detect the spectrum in the broad spectral range from UV to near infrared region from 250 to 1700 nm. The signal from the detectors is coupled via the multiplexer Signal Recovery 3830 to the current preamplifier and a lock-in amplifier referenced to the chopper frequency. The compound detectors are also placed in front and behind the sample S to detect the reflectance and transmittance spectra, whereas the relative absorption spectra are detected by the position detector monitoring the laser beam parallel to the sample surface. The generated heat in the thin film on a glass substrate generates periodical thermal waves in the liquid surrounding the sample causing periodical deflection of the laser beam. The amplitude of the deflection normalized to a black sample (such as carbon nanotubes thin film on glass) spectra gives the optical absorption of thin films.

The dielectric function of thin films is evaluated from the reflectance and absorption spectra using the commercial software FilmWizard (http://www.sci-soft.com/). First, the parameters of a suitable model describing the real and complex index of refraction are fitted together with the film thickness. In the case of BNCD Lorentz Oscillator and Drude model were applied to describe both bandgap absorption and the absorption on free carriers. The surface scattering is modeled by effective media approximation [41].

Once the index of refraction, thin film thickness and surface roughness are known, the optical absorption coefficient can be calculated from the absorption spectrum (A) or in the case of smooth films from A/T using the Ritter-Weiser model [42].

3.3. Results & discussion

3.3.1. Optical images

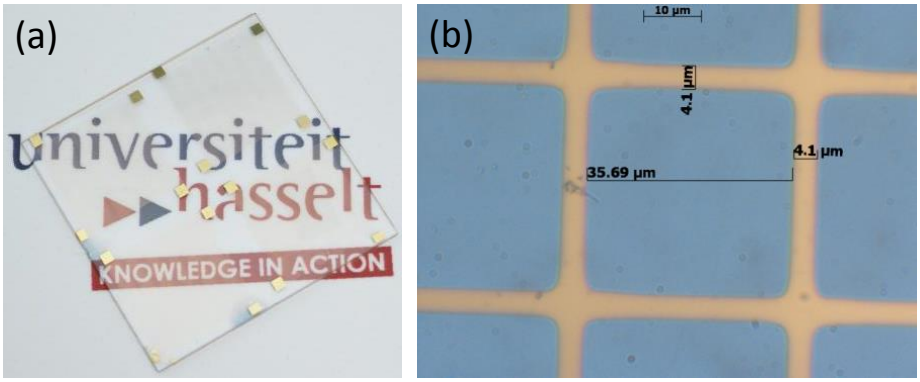

Figure 3-V: (a) Optical image of Au grid imbedded in BNCD diamond layer. (b) Optical microscopy image of the electrode. The grid lines are ~4 µm wide and the pitch is ~36 µm.

Optical microscopy images of optimal BNCD:Cr/Au electrodes are shown in Figure 3-V (a)-(b)). The visual morphology of the grid is shown in Figure 3-V (a). In the corners of the sample, 4 grids are shown with a size of 1 cm by 1 cm. A higher magnification image is shown in Figure 3-V (b) 4 µm gold grid lines spaced 36 µm from each other.

3.3.2. Transmission and resistivity

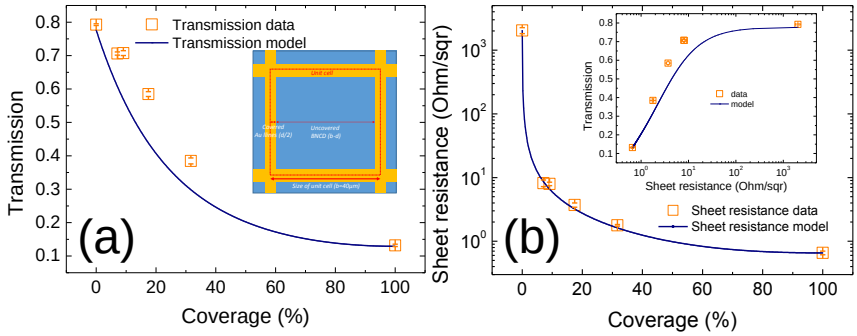

Figure 3-VI: (a) Transmission as a function of metal coverage for a 40 µm unit cell. Inset shows the unit cell and the related parameters. A coverage of 0 % would correspond to a BNCD layer without any metallic grid and 100% corresponds to a full metal layer on a BNCD structure. Inset shows optical transmission as a function of sheet resistance. The transmission is measured using a parallel beam of Air Mass 1.5 solar simulated light. *(b) Sheet resistance*

as a function of metal coverage for a 40 µm unit cell. Inset shows transmission as a function of sheet resistance.

Transmission measurements on BNCD with embedded grids have been performed as a function of metal coverage as can be seen in Figure 3-VI. The line width of the metal lines is an important parameter. For a squared grid the relation between the transparency of the grid T(d) and the line width is given by equation 3-1:

$$T(d) = 10^{\left[-\left(A_{Au}\left(\frac{b^2-(b-d)^2}{b^2}\right)+A_{BNCD}\left(\frac{(b-d)^2}{b^2}\right)\right)\right]} \qquad \textbf{3-1}$$

Where b is the size of the unit cell and d is the size of the BNCD square. $A_{BNCD} = -log(T_{BNCD})$ is the absorbance of the BNCD layer on top of a fused silica substrate. T_{BNCD} is the transmittance of BNCD. $A_{Au} = -log(T_{Au})$ is the absorbance of a pure Cr/Au layer on top of a fused silica substrate. T_{Au} is the transmittance of a pure Cr/Au layer on top of a fused silica substrate. The transmittance of pure diamond is around 80% and for Cr/Au layer is around 10%.

Besides transmittance, also resistivity of the electrode material is a crucial criterion if it should be used as a transparent electrode. The sample resistivity can be obtained by measuring the sheet resistance of the sample with the Van Der Pauw method [43]. This results in a sheet resistance which is defined by the ratio between resistivity and layer thickness. The sheet resistance was modelled using equation 3-2 based on ohms law.

$$R_{sh,tot}(d) = \frac{R_{sh}^{Au}\left(d^2 R_{sh}^{BNCD} + dbR_{sh}^{Au} - d^2 R_{sh}^{BNCD} - dbR_{sh}^{BNCD}\right)}{b\left(dR_{sh}^{BNCD} + bR_{sh}^{Au} - dR_{sh}^{Au}\right)} \qquad \textbf{3-2}$$

Here, R_{sh}^{Au} and R_{sh}^{BNCD} are the sheet resistances of complete gold and BNCD layers. As indicated in the inset of Figure 3-VI (a) d/2 is the width of the gold line in the unit cell and b is the size of the unit cell. Here, the values of R_{sh}^{Au} and R_{sh}^{BNCD} filled into the equation 3-2 were kept constant and d was the variable parameter which depends on the coverage. The derivation and aim of the equation 3-2 is further explained in the Materials and Methods (Appendix section 6). Without fitting it can be seen that the calculated sheet resistance perfectly follows the measurement data in Figure 3-VI (b). The comparison of the transmission as a function of sheet resistance is shown in the inset of Figure 3-VI (b).

Although the sheet resistance is a good measure of the general resistance of the electrode, it is not following the resistive pathway which charge carriers encounter the Cr/Au collecting electrodes in working devices. In a PLED, charge carriers are injected from the low resistive grid into the high resistive BNCD and light is generated at the position where electrons and holes are recombining in the system after the holes crossed it's resistive pathway. The resistive pathway that charge carriers can travel in the electrode is comparable to the spatial

distribution of the yellow light output from the system in Figure 3-VII. The figure shows a microscopic picture of a working PLED. Here we see black lines at the position of the gold grid and the yellow parts represents the SuperYellow luminescence above the BNCD-layer. The homogeneous distribution of the luminescence indicate that the charge carriers are distributed homogeneously over the BNCD part of the grid pattern and that the voltages distributed over the BNCD layer is above the turn-on voltage of SuperYellow.

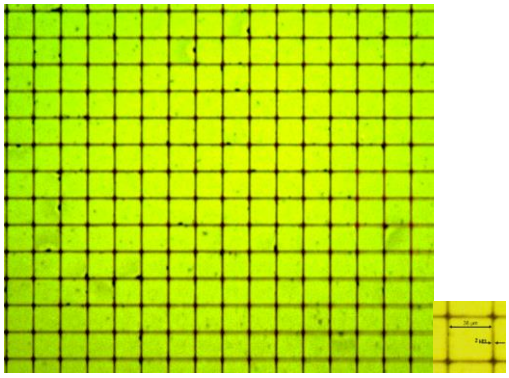

Figure 3-VII: Optical microscopy image of working PLED device based on BNCD/Cr:Au /SuperYellow materials. In the inset, the geometric distances of the grid lines are shown (pitch 36 µm and linewidth 2 µm).

The optical properties of electrodes (transmitted (full black line), reflected (red dashed line) and absorbed light (blue short dashed line)) are further studied in Figure 3-VIII.

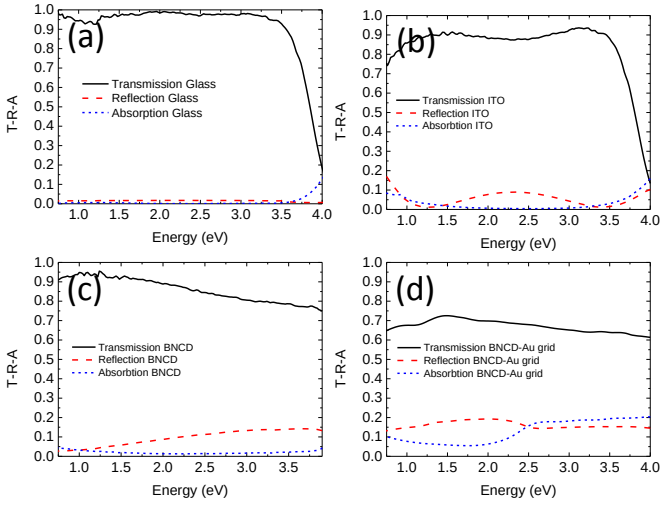

Figure 3-VIII: Transmission-Reflection-Absorption spectra for Glass (a), ITO (b), BNCD (c) and BNCD:Cr/Au layers (d).

For bare glass substrates, the Transmission-Reflection-Absorption (T-R-A) spectra are shown in Figure 3-VIII (a). At energies above 3.5 eV, transmission is reduced due to impurity absorption in the glass. Reflection of the glass substrates remains ~0.01 over the complete energy range.

For the ITO-electrode, T-R-A spectra are shown in Figure 3-VIII (b). ~9% of transmitted light is lost compared to the glass substrates. Like the glass substrate, the transmission is diminished at energies above 3.5 eV. The loss in transmission is mainly due to an increase of 8% of the light reflection in the ITO-layer.

For the BNCD layers (Figure 3-VIII (c)) on fused silica substrates, the transmission is similar with that of ITO. There is no transmission intensity decline at energies above 3.5 eV making these layers interesting for UV-based applications [44]. A clear interference of the reflected light pattern is present in the 87 nm thick BNCD layer. At energies above 3.5 eV, no significant decrease in reflection is observed. Light absorption is low (~1%) for the BNCD film indicating that the main loss is due to reflection, which can be tuned by anti-reflective coatings.

When the Au grid is used, the transmission is reduced further to 70% for a pitch of 36 µm (Figure 3-VIII (d)). The presence of a gold grid increases the reflection up to 0.2. This is due to reflection of light by gold for light energies lower than 2.5 eV. Light absorption is increased at values above 2.5eV due to the absorption of light by the gold grid.

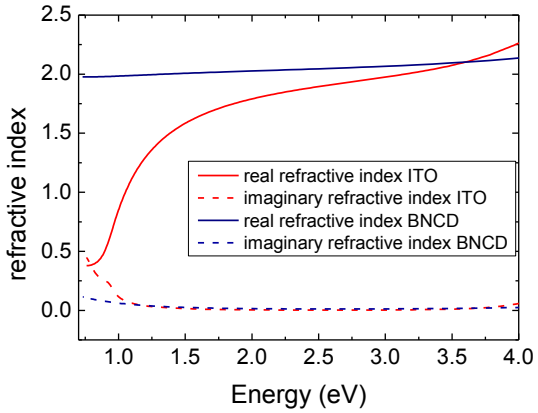

Figure 3-IX: Real and imaginary part of the refractive index of BNCD and ITO as modelled from T-R-A data. A colored version of the figure can be found in the electronic version of the thesis.

Absorption, reflection and transmission data was used to model the complex index of refraction as shown in Figure 3-IX. The figure shows that for the BNCD, the real and imaginary part are constant over the whole energy range for their respective values of 2 and 0.011. For ITO, the real part changes from 0.37 at 0.78 eV up to 2.3 at 4 eV. The refractive indices of the polymers are better

matched with those of BNCD, making BNCD a better material for accepting light from the polymers [35]. In the future, layers with gradually changing refractive indices can be used to maximize the light output to the low refractive index environment.

3.3.3. Application in PLED devices

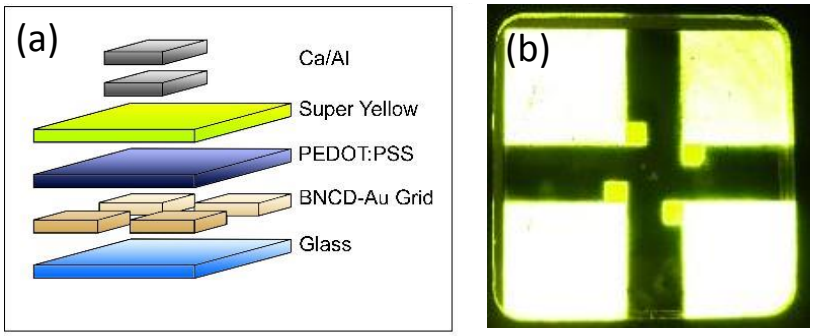

Figure 3-X: (a) Schematic layout of PLEDs. (b) Macroscopic optical image of a BNCD-Cr/Au grid electrode device under operation.

PLEDs were constructed on BNCD electrodes, as shown in Figure 3-X (a), and compared to ITO electrode reference devices. ITO reference devices were, apart from the ITO anode, constructed in an identical way. Figure 3-X (b) illustrates the BNCD-Cr/Au electrode integrated in a working PLED. Figure 3-X (b) also shows the homogenous PLED emitted light distribution over the BNCD-Cr/Au grid electrode. The total luminance flux (Φ) – voltage (V) and the current density (J) – voltage (V) characteristics of the PLEDs fabricated with both electrodes are shown in Figure 3-XI.

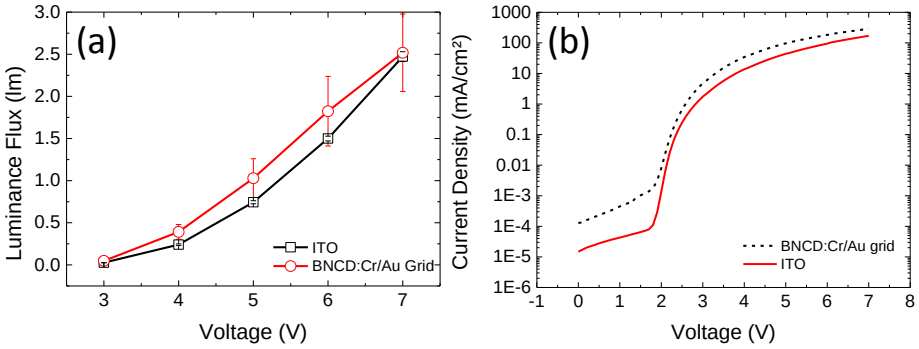

Figure 3-XI: (a) The total luminance flux (Φ) as a function of the applied voltage on the ITO and BNCD-Cr/Au grid electrode devices. (b) The current density vs voltage (J-V) characteristics, in semi-log plot, of ITO and BNCD-Cr/Au grid electrode PLEDs, with identical device structures. A colored version of the figure can be found in the electronic version of the thesis.

BNCD–Cr/Au LEDs JV-characteristics show enhanced current densities for the same voltage compared to the ITO reference. Accordingly, the PLED constructed on the BNCD- Cr/Au electrode exhibits an overall higher total luminance flux compared to the ITO electrode PLEDs. The luminance flux is enhanced, despite the light transmission losses in the BNCD- Cr/Au grid. The transmission and reflection measurements, as depicted above in Figure 3-VIII, show that the transmission of the BNCD-Cr/Au grid and glass substrate (68%) is ~20% lower than the transmission of ITO patterned glass substrate (87%) at the dominant emission peak around 2.25 eV (550 nm). From linear fitting of the J-V characteristics, the turn-on voltages (V_{ON}) were determined. For the BNCD-Cr/Au grid PLEDs a turn-on voltage of 1.76 V was measured and for the ITO PLEDs 1.80 V. The higher current density and total luminance flux of the BNCD-Cr/Au grid electrode PLEDs are ascribed to improved hole injection. Optical transparency can be enhanced by 7.5% by simple reduction of the grid line thickness from the current 4 microns to 1 micron. Optimization of the BNCD layer hole carrier mobility would enable an increase in the grid pitch and reach even higher optical transparencies.

3.4. Conclusion

In conclusion, we demonstrated a novel ITO-free transparent electrode for PLEDs and a novel production process to embed a metal (gold) grid into a BNCD diamond film. After the BNCD diamond growth the gold grid was embedded into the layer by a series of solution processing, vacuum deposition and photolithography steps. The transparent electrodes were optically and electrically characterized and optimized to yield the highest optical transparency and the lowest in-plane resistivity. The resulting orthogonal gold grid has a trace width of 2 µm spaced 36 µm apart. Further optimization of the substrate and the BNCD/Cr:Au grid layer is needed to improve the optical transmission. The application of BNCD:Cr/Au electrodes in organic electronic devices was demonstrated. Furthermore, the optical and electrical characterization of PLEDs was performed using the described BNCD/Cr:Au grid electrode. To accurately assess the performance of these devices, identical reference devices with ITO electrode were prepared. Although, the BNCD/Cr:Au grid electrode devices suffer a lower luminous power efficacy, we suggest that, further work is needed to improve optoelectronic properties of the electrode. These results show that the described BNCD/Cr:Au grid electrode is already a viable alternative to replace ITO in PLEDs taking into account the thermal conductivity and chemical stability.

References

[1] R. G. Gordon, "Criteria for Choosing Transparent Conductors," *MRS Bull.*, vol. 25, no. 08, pp. 52–57, Jan. 2011.

[2] A. R. Schlatmann, D. W. Floet, A. Hilberer, F. Garten, P. J. M. Smulders, T. M. Klapwijk, and G. Hadziioannou, "Indium contamination from the indium–tin–oxide electrode in polymer light-emitting diodes," *Appl. Phys. Lett.*, vol. 69, no. 12, p. 1764, Sep. 1996.

[3] C. W. Tang and S. A. VanSlyke, "Organic electroluminescent diodes," *Appl. Phys. Lett.*, vol. 51, no. 12, pp. 913 – 915, 1987.

[4] J. H. Burroughes, D. D. C. Bradley, A. R. Brown, R. N. Marks, K. Mackay, R. H. Friend, P. L. Burns, and A. B. Holmes, "Light-emitting diodes based on conjugated polymers," *Nature*, vol. 347, no. 6293, pp. 539–541, 1990.

[5] A. Klein, C. Körber, A. Wachau, F. Säuberlich, Y. Gassenbauer, S. P. Harvey, D. E. Proffit, and T. O. Mason, "Transparent Conducting Oxides for Photovoltaics: Manipulation of Fermi Level, Work Function and Energy Band Alignment," *Materials (Basel).*, vol. 3, pp. 4892–4914, 2010.

[6] P. P. Edwards, A. Porch, M. O. Jones, D. V. Morgan, and R. M. Perks, "Basic materials physics of transparent conducting oxides," pp. 2995–3002, 2004.

[7] T. Ashida, A. Miyamura, N. Oka, Y. Sato, T. Yagi, N. Taketoshi, T. Baba, and Y. Shigesato, "Thermal transport properties of polycrystalline tin-doped indium oxide films," *J. Appl. Phys.*, vol. 105, 2009.

[8] H. H. Khaligh and I. a Goldthorpe, "Failure of silver nanowire transparent electrodes under current flow.," *Nanoscale Res. Lett.*, vol. 8, no. 1, p. 235, 2013.

[9] M. Ma, F. W. Mont, X. Yan, J. Cho, E. F. Schubert, G. B. Kim, and C. Sone, "Effects of the refractive index of the encapsulant on the light-extraction efficiency of light-emitting diodes.," *Opt. Express*, vol. 19 Suppl 5, no. S5, pp. A1135–40, Sep. 2011.

[10] F. W. Mont, J. K. Kim, M. F. Schubert, E. F. Schubert, and R. W. Siegel, "High-refractive-index TiO[sub 2]-nanoparticle-loaded encapsulants for light-emitting diodes," *J. Appl. Phys.*, vol. 103, no. 2008, p. 083120, 2008.

[11] A. Bahtiar, K. Koynov, Y. Mardiyati, H.-H. Hörhold, and C. Bubeck, "Slab waveguides of poly(p-phenylenevinylene)s for all-optical switching: impact of side-chain substitution," *J. Mater. Chem.*, vol. 19, p. 7490, 2009.

[12] Y. Wang, S. W. Tong, X. F. Xu, B. Ozyilmaz, and K. P. Loh, "Interface engineering of layer-by-layer stacked graphene anodes for high-performance organic solar cells.," *Adv. Mater.*, vol. 23, no. 13, pp. 1514–8, Apr. 2011.

[13] D. S. Hecht and R. B. Kaner, "Solution-processed transparent electrodes," *MRS Bull.*, vol. 36, no. 10, pp. 749–755, Oct. 2011.

[14] H. Park, S. Chang, M. Smith, S. Gradečak, and J. Kong, "Interface engineering of graphene for universal applications as both anode and cathode in organic photovoltaics.," *Sci. Rep.*, vol. 3, p. 1581, 2013.

[15] Y. A. Akimov, "The Potential of Graphene as an ITO Replacement in Organic Solar Cells: An Optical Perspective," *IEEE J. Sel. Top. Quantum Electron.*, vol. 20, no. 1, pp. 36–42, Jan. 2014.

[16] Y. L. Zhong, A. Midya, Z. Ng, Z.-K. Chen, M. Daenen, M. Nesladek, and K. P. Loh, "Diamond-based molecular platform for photoelectrochemistry.," *J. Am. Chem. Soc.*, vol. 130, no. 51, pp. 17218–9, Dec. 2008.

[17] C. H. Y. X. Lim, Y. L. Zhong, S. Janssens, M. Nesladek, and K. P. Loh, "Oxygen-terminated nanocrystalline diamond film as an efficient anode in photovoltaics," *Adv. Funct. Mater.*, vol. 20, pp. 1313–1318, 2010.

[18] W. S. Yeap, X. Liu, D. Bevk, A. Pasquarelli, L. Lutsen, M. Fahlman, W. Maes, and K. Haenen, "Functionalization of Boron-Doped Nanocrystalline Diamond with N3 Dye Molecules.," *ACS Appl. Mater. Interfaces*, Jun. 2014.

[19] M. Ye, M. Lv, C. Chen, J. Iocozzia, C. Lin, and Z. Lin, *Low-cost Nanomaterials*. 2014.

[20] Y. Galagan and J. J. Rubingh, "ITO-free flexible organic solar cells with printed current collecting grids," *… Sol. Cells*, vol. 95, no. 5, pp. 1339–1343, 2011.

[21] Y. Zhu, Z. Sun, Z. Yan, Z. Jin, and J. M. Tour, "Rational Design of Hybrid Graphene Films for High-Performance," *ACS Nano*, vol. 5, no. 8, pp. 6472–6479, 2011.

[22] P. Lin, W. C. H. Choy, D. Zhang, F. Xie, J. Xin, and C. W. Leung, "Semitransparent organic solar cells with hybrid monolayer graphene/metal grid as top electrodes," *Appl. Phys. Lett.*, vol. 102, 2013.

[23] W. Gaynor, G. F. Burkhard, M. D. McGehee, and P. Peumans, "Smooth nanowire/polymer composite transparent electrodes," *Adv. Mater.*, vol. 23, pp. 2905–2910, 2011.

[24] Y. J. Noh, S. S. Kim, T. W. Kim, and S. I. Na, "Cost-effective ITO-free organic solar cells with silver nanowire-PEDOT:PSS composite electrodes via a one-step spray deposition method," *Sol. Energy Mater. Sol. Cells*, vol. 120, pp. 226–230, 2014.

[25] Y. Galagan, B. Zimmermann, E. W. C. Coenen, M. Jørgensen, D. M. Tanenbaum, F. C. Krebs, H. Gorter, S. Sabik, L. H. Slooff, S. C. Veenstra, J. M. Kroon, and R. Andriessen, "Current collecting grids for ITO-free solar cells," *Adv. Energy Mater.*, vol. 2, pp. 103–110, 2012.

[26] S. Dongaonkar, "Technology agnostic analysis and design for improved performance, variability, and reliability in thin film photovoltaics," *Theses and Dissertations Available from ProQuest*. pp. 1 – 229, 2013.

[27] A. R. Burgers,"Method for manufacturing a metallization pattern on a photovoltaic cell." United States Patent and Trademark Office, Patent Application No. 09856557, 2013

[28] T. Teraji, S. Koizumi, and Y. Koide, "Ohmic contact for p -type diamond without postannealing," *J. Appl. Phys.*, vol. 104, no. May 2013, pp. 10–13, 2008.

[29] G. Kawaguchi, J. Nakanishi, A. Otsuki, T. Oku, and M. Murakami, "Dependence of contact resistance on metal electronegativity for B-doped diamond films," *J. Appl. Phys.*, vol. 75, no. 10, p. 5165, May 1994.

[30] J. C. Bolsée and J. Manca, "Effects of hole and electron trapping on organic field-effect transistor transfer characteristic," *Synth. Met.*, vol. 161, pp. 789–793, 2011.

[31] J. Nakanishi, a. Otsuki, T. Oku, O. Ishiwata, and M. Murakami, "Formation of ohmic contacts to p-type diamond using carbide forming metals," *J. Appl. Phys.*, vol. 76, no. May 2013, pp. 2293–2298, 1994.

[32] M. Yokoba, Y. Koide, a Otsuki, F. Ako, T. Oku, and M. Murakami, "Carrier transport mechanism of Ohmic contact to p -type diamond," vol. 81, no. May 2013, pp. 6815–6821, 1997.

[33] H. A. Hoff, G. L. Waytena, C. L. Vold, J. S. Suehle, I. P. Isaacson, M. L. Rebbert, D. I. Ma, and K. Harris, "Ohmic contacts to semiconducting diamond using a Ti/Pt/Au trilayer metallization scheme," *Diam. Relat. Mater.*, vol. 5, no. 12, pp. 1450–1456, Dec. 1996.

[34] J.-S. Yu, I. Kim, J.-S. Kim, J. Jo, T. T. Larsen-Olsen, R. R. Søndergaard, M. Hösel, D. Angmo, M. Jørgensen, and F. C. Krebs, "Silver front electrode grids for ITO-free all printed polymer solar cells with embedded and raised topographies, prepared by thermal imprint, flexographic and inkjet roll-to-roll processes," *Nanoscale*, vol. 4, p. 6032, 2012.

[35] W. L. W. Born Max, Wolf Emil, A. B. Bhatia, P. C. Clemmow, D. Gabor, A. R. Stokes, A. M. Taylor, P. A. Wayman, "Principles of Optics: Electromagnetic Theory of Propagation, Interference and Diffraction of Light: : 9780521642224: Amazon.com: Books.".

[36] H. G. Tompkins and W. A. McGahan, *Spectroscopic Ellipsometry and Reflectometry: A User's Guide*. 1999.

[37] W. B. Jackson, N. M. Amer, A. C. Boccara, and D. Fournier, "Photothermal deflection spectroscopy and detection.," *Appl. Opt.*, vol. 20, no. 8, pp. 1333–44, Apr. 1981.

[38] K. R. Williams, K. Gupta, and M. Wasilik, "Etch rates for micromachining processing-part II," *J. Microelectromechanical Syst.*, vol. 12, no. 6, pp. 761–778, Dec. 2003.

[39] "Principles of Optics: Electromagnetic Theory of Propagation, Interference and Diffraction of Light: Max Born, Emil Wolf, A. B. Bhatia, P. C. Clemmow, D. Gabor, A. R. Stokes, A. M. Taylor, P. A. Wayman, W. L. Wilcock: 9780521642224: Amazon.com: Books.".

[40] "Spectroscopic Ellipsometry and Reflectometry: A User's Guide: Harland G. Tompkins, William A. McGahan: 9780471181729: Amazon.com: Books.".

[41] Z. Remes, R. Vasudevan, K. Jarolimek, A. H. M. Smets, and M. Zeman, "The Optical Spectra of a-Si:H and a-SiC:H Thin Films Measured by the Absolute Photothermal Deflection Spectroscopy (PDS)," in *Solid State Phenomena*, 2014, vol. 213, pp. 19–28.

[42] D. Ritter and K. Weiser, "Suppression of interference fringes in absorption measurements on thin films," *Opt. Commun.*, vol. 57, no. 5, pp. 336–338, Apr. 1986.

[43] L. J. Van Der Pauw, "A method of measuring specific resistivity and hall effect of discs of arbitrary shape," *Philips Res. Reports*, vol. 13, no. 1, pp. 1–9, 1958.

[44] J. L. Bolognia, J. L. Jorizzo, and R. P. Rapini, *Dermatology*. Gulf Professional Publishing.

Chapter 4 Use of BNCD/Cr:Au electrodes in organic solar cell applications

4.1. Introduction

This chapter aims to demonstrate the potential of novel BNCD electrodes for solar cell applications and provide a detailed study of organic solar cell performance constructed on BNCD/Cr:Au electrodes with and without PEDOT:PSS layers. P3HT:PCBM blends are used as an active layer material. BNCD/Cr:Au electrodes are investigated with (15 devices) and without PEDOT:PSS (6 devices). For reference devices, indium tin oxide (ITO) is used as a transparent electrode (6 devices were studied).

In the first part, we study the short circuit resistance of BNCD – P3HT/PCBM solar cells for different light intensities from JV-curves and FTPS-measurements.

In the second part, the effect of the light intensity dependency of leakage current is modelled and related with the charge collection efficiency. The effects of bimolecular recombination on the charge collection efficiency are investigated. Afterwards, the effects of the charge collection efficiency is studied from the point of view of the charge transfer energy and the open circuit voltage complementing previous works on different active layer materials by Vandewal et al [1], [2] and Piersimoni et al [3].

Finally, Kelvin probe results are presented, showing the effectiveness of PEDOT:PSS coverage on BNCD electrodes.

The chapter is structured as follows

- Introductory discussion on effects of electrode materials on solar cell parameters
- Experimental section with description of
  - Light intensity dependent JV-characterization
  - Fourier transform photocurrent spectroscopy (FTPS)
  - Scanning Kelvin Probe microscopy
- Result and discussion
  - Experimental JV-characteristics of BNCD- P3HT/PCBM devices
  - Light dependency of short circuit resistance
  - Light intensity dependent photocurrent and FTPS results
  - Light intensity dependent open circuit voltage
  - Kelvin probe study of electrodes

4.1.1. Leakage currents

In this chapter we show that leakage currents can originate at the interface of BNCD:Au electrodes and polymer layers on the device. These leakage currents affect the reproducibility of solar cell parameters of P3HT:PCBM solar cells on BNCD/Cr:Au electrodes. These effects are compared to ITO electrodes. JV-characterization is used as the main technique to probe the effects of the leakage currents. Recombination mechanisms are studied both at short circuit current and at open circuit voltage. The electrode limitation of attained power conversion efficiencies are also discussed. Recombination mechanisms can be subdivided into Langevin recombination [4] and non-radiative trap assisted recombination [5]. FTPS is used in order to probe the effects of leakage currents on the charge transfer state. In this way we show a framework in which the devices can be further optimized.

Leakage currents are related to the backflow of generated charge carriers at the electrodes. This occurs in regions where the active layer is thin. These leakage currents are already visible in dark JV-measurements[6]. Besides dark leakage currents, the light intensity dependence is also investigated [7]. Leakage currents mainly affect the slope of the JV-curve at applied voltages around 0 V. Although dark leakage current have barely any effect on the short circuit current, [7] Vos et al showed in their work that the light intensity dependent leakage current also influences the charge transport of photo-generated charges and could influence the short circuit current. In addition, leakage currents can also affect the open circuit voltage. Other factors which have the possibility to limit open circuit voltage are discussed below.

4.1.2. Electrode work function

In organic solar cells, the difference in electrode work function between a transparent electrode and counter electrode, as well as matching to the electronic structure of the active layers, is important for the built-in voltage in the device [8]. Electrode work function can be altered by the influence of the active layer after coming into close contact due to charge transfer effects between the materials [9]. The effect of the work function difference between the anode and cathode has also been related to the open circuit voltage [10], [11].

4.1.3. Active layer composition and recombination aspects

The open circuit voltage is strongly regulated by the active layer composition and donor – acceptor energy alignment, influencing also the recombination mechanisms on the p-n junction [5], [12]. This is due to the fact that at room temperature, charge carriers from the HOMO of the electron donor can thermally partially populate the LUMO of the acceptor creating free holes in the electron donor HOMO under dark conditions. [13]. The thermal transport of these charge carriers is responsible for the dark saturation current, which is ultimately responsible for the limitation of the open circuit voltage [14].

Trap assisted recombination can be caused in organic based materials by bulk trap states or traps at the interface [15], [16]. These trap states are mainly located within the band gap, and are responsible for immobilization of charge carriers [17], [18].

In this study, we studied how leakage currents can be reduced by the use of an electron blocking layer such as PEDOT:PSS. Investigated parameters are leakage current, dark saturation current, ideality factor, and bimolecular recombination parameter determined from light intensity dependent JV-characterization. In addition, the effect of light intensity dependent leakage currents on the charge transfer energy are studied by Fourier transform photocurrent spectroscopy (FTPS). Kelvin probe measurements are used in order to study the work function composition of the BNCD/Cr:Au electrodes and how these are affected by the coverage of the electrode by PEDOT:PSS layers.

4.2. Experimental section

Here we give an overview of the sample preparation and the methods used to characterize the solar cell devices based on BNCD:Cr/Au electrodes.

- First, a description of the method used to produce P3HT:PCBM solar cells is given. In order to investigate the effects of PEDOT:PSS, we prepared devices with and without a PEDOT:PSS layer on BNCD:Cr/Au electrodes. These devices were compared to ITO-devices with a PEDOT:PSS layer. The active layer deposition conditions remained the same during the investigations.
- The techniques used to characterize the devices used in this chapter are:
    - Light intensity dependent JV-characterization. This technique is the principal technique for determination of device performances and in addition information on how charge recombination influences the device performance.
    - FTPS is used as an opto-electronical technique to investigate the sub-bandgap properties of organic solar cell devices. This is of particular interest as it probes the charge transfer properties at the molecular level.
    - Scanning Kelvin Probe microscopy is used as a technique to probe the effects of PEDOT:PSS on the interfacial electronic properties of BNCD/Cr:Au electrodes.

4.2.1. Preparation of BNCD electrodes

BNCD/Cr:Au electrodes used in this work were prepared according to the description in the previous chapter. Prior to solar cell preparation, BNCD:Cr/Au covered substrates and the indium tin oxide (ITO) coated (100 nm) glass substrates (Kintec, sheet resistivity 20 Ω/sqr) were exposed to an ultrasonic bath cleaning procedure of 30 min in soap solution, 10 min in demineralized water, 10 min in acetone and 10 min in isopropanol, followed by a UV/O3-treatment for 15 min.

On clean substrates poly(3,4-ethylenedioxythiophene):poly(styrenesulfonate) PEDOT:PSS was spin coated in an ambient atmosphere to form a layer thickness of ~35 nm. The PEDOT:PSS covered substrates were annealed in an inert atmosphere (N_2) at 120 °C for 10 min. For 6 BNCD:Cr/Au samples this processing step was omitted.

For solar cell preparation, a ~250 nm thick layer of a polymer blend was spin coated in an inert atmosphere from a solution. The solution composed of 20 mg/ml Poly(3-hexylthiophene-2,5-diyl) (P3HT) 16 mg/ml (6,6)-Phenyl C61 butyric acid methyl ester (PCBM) in Ortho-dichlorobenzene. The solution was prepared in an inert atmosphere and stirred overnight at 50°C. The layer was slow dried in an inert atmosphere for ~1 h. On top of the P3HT:PCBM layer, a layer of ~30 nm Ca and ~80 nm Al was thermally evaporated at a pressure of ~10E-6 Bar.

4.2.2. Characterization of electrodes

JV-characterization was performed by the use of a Keithley 2400 multimeter. The voltage was swept from -0.5 V up to 1.5 V in order to obtain information necessary to extract solar cell parameters. Solar cells were characterized by the

use of a Keithley 2400 multimeter and illuminated using a solar simulator Newport Oriel class A, equipped with a Xenon Short Arc lamp with 150 W power (1 sun at 1.5 air mass density, i.e. 100 mW/cm^2). Neutral density filters (Edmund Optics) were used in order to regulate the light intensity during the JV-sweep.

FTPS measurements were performed using a frequency modulated beam of a Thermo Electron Nicolet 8700 FTIR with an external detector. This procedure is further described in Ref. [19].

Scanning Kelvin Probe Microscopy (SKPM) was carried out using a Park Systems XE-100. A conductive gold (Au) tip was used to perform the topographic and surface potential (SP) measurements in a dual-pass tapping mode. In SKPM measurements, the Fermi levels are aligned between the sample surface and the Au tip when they are electrically connected. A finite electrical field generated by the work function (WF) difference between the sample and the tip is nullified by the voltage applied from the SKPM system. This applied voltage is identified as the SP = WF tip-WF sample where WF tip and WF sample are the WFs of the probe tip and the sample respectively. In this study, the probe tip was calibrated against a reference sample HOPG (WF is 4.6 eV). Filtered PEDOT:PSS (via 0.45 µm filter) was spin coated onto a diamond-grid with at 500 rpm for 5 s and then 3000 rpm for 60 s. A 80 nm thick PEDOT:PSS layer was then produced after annealing in an oven at 120 °C.

4.3. Results and discussion

4.3.1. JV-characteristics

Solar cells were prepared by the deposition of P3HT:PCBM films on top of transparent BNCD electrodes in several configurations. For these devices, typical JV-characteristics are shown in Figure 4-I where the solar cells with bare BNCD:Cr/Au electrode depicted by the blue short dashed line, the devices based on BNCD:Cr/Au electrode covered by a PEDOT:PSS layer by a black long dashed line and the reference device based on ITO electrodes covered by PEDOT:PSS by a red full line.

From Figure 4-I it can be seen that by the use of different types of transparent electrodes, both the short circuit current (J_{sc}) and open circuit voltage (V_{oc}) are affected. Although, the efficiencies of BNCD – P3HT/PCBM solar cells are close to the efficiencies of reference devices, it was observed that the efficiency values are scattered from device to device, despite similar cleaning steps and active layer processing conditions were used. In order to understand the cause of the randomly changing recombination mechanism, light intensity dependent JV-measurements were performed in combination with FTPS.

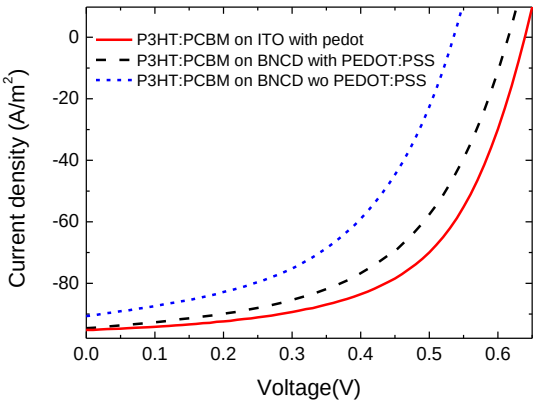

Figure 4-I: JV-curves of studied solar cells.

4.3.2. Introduction of light intensity dependency of R_{sc} and introduction of ΔV_{oc}

For improved understanding of differences in solar cell characteristics of OBHJ devices based on BNCD the following characteristics were studied in detail.

First, the short circuit resistance R_{sc} can be defined as the resistance in the JV-curve plot at 0 V or the short circuit current. The short circuit resistance is determined by the factor 1/slope as can be seen in the red dotted lines on the blue IV curves in Figure 4-II (a).

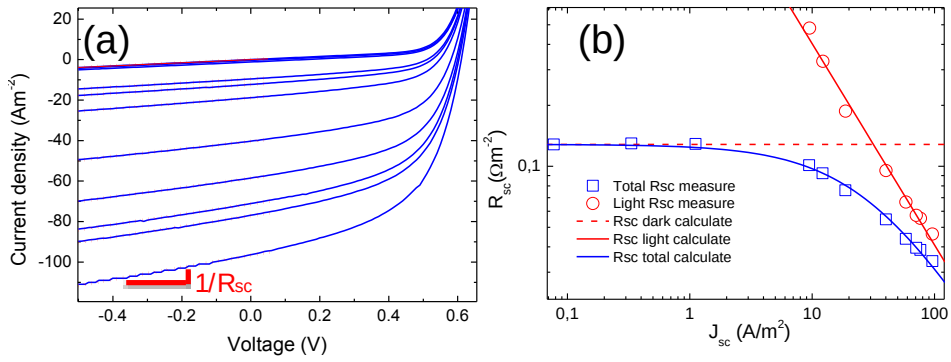

Figure 4-II: (a) Measurement method for short circuit resistance measurement. The different curves result from measuring the same device at different light intensities. (b) Short circuit resistance as a function of short circuit current density derived from JV plots measured at different illumination levels at 0 V. The short circuit resistance can be subdivided into a dark part (red dotted line) and a light dependent part, which decreased the short circuit resistance further with increasing the short circuit current. The short circuit current is modulated by changing the light intensity falling on the solar cell device during the measurements. This part is shown with the red line. The light illumination corresponded to 1.5 Air Mass.

In Figure 4-II (b), it is seen that as a function of increasing short circuit current, the short circuit resistance can drop by an order of magnitude. The short circuit current depends on the light intensity during measurements. The dark short circuit resistance is mainly caused by low resistive regions in the active layer and where dark leakage currents tend to be high. The light short circuit- and dark short circuit resistance can be expressed according to the following relation as discussed by Merten et al. [20]:

$$\frac{1}{R_{sc(tot)}} = \frac{1}{R_{sc(dark)}} + \frac{1}{R_{sc(Light)}} \qquad \textbf{4-1}$$

Equation 4-1 is valid in all types of solar cell devices although the light intensity induced short circuit resistance has negligible effects on the open circuit voltage of optimal working devices. The ln-ln relation between the short circuit current and R_{sc} (Light) is linear (full red line in Figure 4-II (b)). Due to the decrease of short circuit resistance at high short circuit currents, the open circuit voltage has to be corrected for light dependent short circuit resistance effects. The correction for this can be done using the relation described in Equation 4-2:

$$J(V)_{corrected} = J(V)_{original} - \left(\frac{V}{R_{sc}}\right) \qquad \textbf{4-2}$$

Trends of V_{oc} as a function of light intensity, before and after short circuit resistance correction, can be seen in *Figure 4-III*.

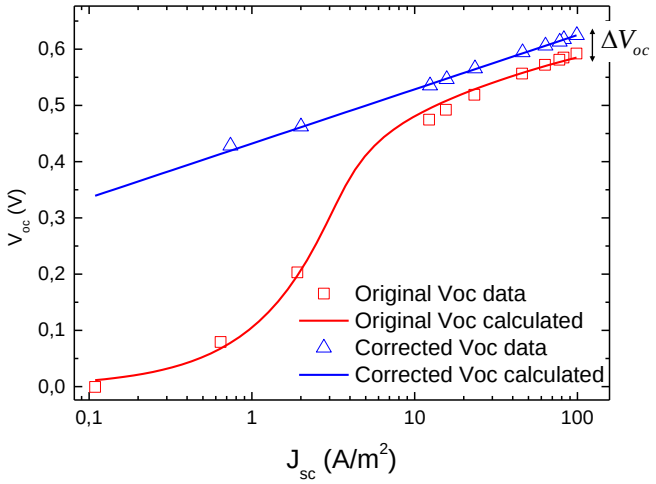

Figure 4-III: Open circuit voltage as a function of short circuit current. The red symbols represent open circuit voltage as a function of short circuit current for the original data. The red line shows the convolution of the effects of both dark and light short circuit resistances. The blue triangle symbols and the fit-line represent the open circuit voltage after correction for dark- and light leakage currents. ΔV_{oc} *is determined under light-conditions of 1.5 Air Mass.*

In *Figure 4-III* a linear trend between the open circuit voltage as a function of the short circuit current after correction for the R_{sc} (blue line with triangle symbols) can be established.

In order to plot the open circuit voltage linearly as a function of the short circuit current, the short circuit current should be reverted to logarithmic scale. Therefore, it is possible to determine the ideality factor n and dark saturation current J_o by linearly fitting the corrected data points marked by the blue color line through with blue triangles. This is carried out according to the relation described in equation 4-3:

$$V_{oc(corrected)} = \frac{nkT}{q}\ln\left(\frac{J_{sc}}{J_o}\right) \qquad \textbf{4-3}$$

From these fitted values and the expression of the short circuit resistance as a function of light intensity, the original open circuit voltage can be recalculated according to equation 4-4.

$$V_{oc(original)} = J_{sc}R_{sc(tot)} - \frac{nkT}{q}LambertW\left(\frac{qJ_0R_{sc(tot)}}{nkT}\exp\left(\frac{qR_{sc(tot)}(J_{sc}+J_0)}{nkT}\right)\right) \qquad \textbf{4-4}$$

Where LambertW is defined as follows: $x = y.\exp(y) \Leftrightarrow y = LambertW(x)$. By comparing the convoluted and deconvoluted data at 1 sun light intensity, a shift in V_{oc} (ΔV_{oc}) is visible. ΔV_{oc} can thus be defined as the change in open circuit voltage due to light induced leakage currents in the solar cell device. In this work, ΔV_{oc} is determined under light-conditions of 1.5 Air Mass.

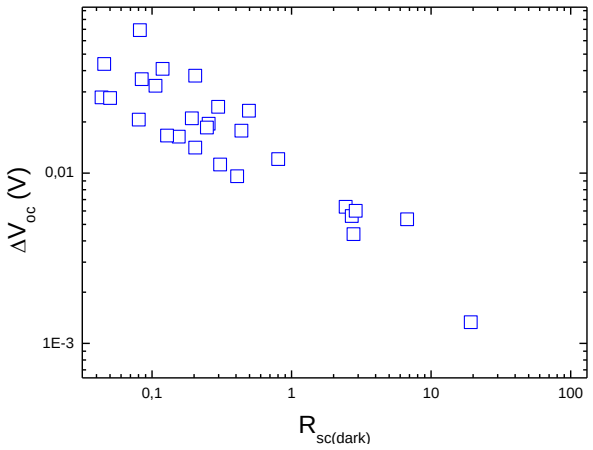

Figure 4-IV: Effect of short circuit resistance on open circuit voltage difference calculated from corrected JV-curves. Every point represents a different solar cell. ΔV_{oc} *was determined under light-conditions of 1.5 Air Mass while dark shunt resistance* $R_{sc(dark)}$ *is determined from dark JV-curves.*

In order to investigate if there is any relationship between dark- and light induced leakage currents, ΔV_{oc} is plotted as a function of the dark shunt resistance. This relationship reveals a ln-ln relationship as shown in *Figure 4-IV*. This indicates that the dark short cut resistance has a significant influence on the light intensity dependent shunt resistance, which is responsible for ΔV_{oc} .

In order to give a physical meaning to the light induced short circuit resistance, the short circuit resistance data is modelled according to the model described by Vos et al. in Ref. [7] and developed by Crandall in Ref. [21]. In the work of Vos et al. in Ref [7], the short circuit resistance is related to the charge collection length in solar cell devices. This relation is described by equation 4-5.

$$R_{sc(light)} = \left(\frac{l_{co}}{L/2} - 1 \right) \frac{V_{bi}}{J_{sc}} \qquad \textbf{4-5}$$

Where l_{co} is the collection length at short circuit current, L the thickness of the active layer, V_{bi} the built-in voltage as determined according to Ref. [22] and J_{sc} is the short circuit current density. The collection length is equal to the sum of the collection lengths of electrons and holes. It is conceptually the maximal distance a charge can travel after dissociation of the exciton before it recombines. By approximation, the average position where the free charge carriers are generated is in the center of the device at a position of $L/2$.

From the ratio between the device thickness and the collection length, the collection efficiency can be extracted according to equation 4-6 [7]:

$$\eta = 1 - \frac{L/2}{l_{co}} \qquad \textbf{4-6}$$

The collection length l_{co} is actually the weighted sum of drift lengths of electrons and holes [21]. Diffusion currents are neglected, since the collection length is determined at short circuit conditions, where the internal built-in field is high, and the effects of diffusion currents are negligible compared to the drift currents. The reference to which this distance is measured is half of the active layer thickness L. The collection efficiency determines the charge transport quality at short circuit current. It can thus be defined as the distance that a charge carrier can travel at short circuit conditions compared to half the thickness of the active layer. It should not be confused with other types of efficiencies such as power conversion efficiency, which relates to the amount of solar light power which is converted into electrical power, or quantum efficiency, which relates to the amount of charge carriers which escape the device compared to the amount of generated charge carriers.

In Figure 4-V, the effects of ΔV_{oc} on the collection length is given by the red squares. In the inset the effect of ΔV_{oc} on charge collection efficiency is seen. The reciprocal relation between collection length with ΔV_{oc} together with the inverse relation between ΔV_{oc} and $R_{sc(dark)}$ shows that low shortcut resistances

in dark results in the degradation of charge transport (measured by lower collection lengths) and with it also reduced charge collection efficiencies.

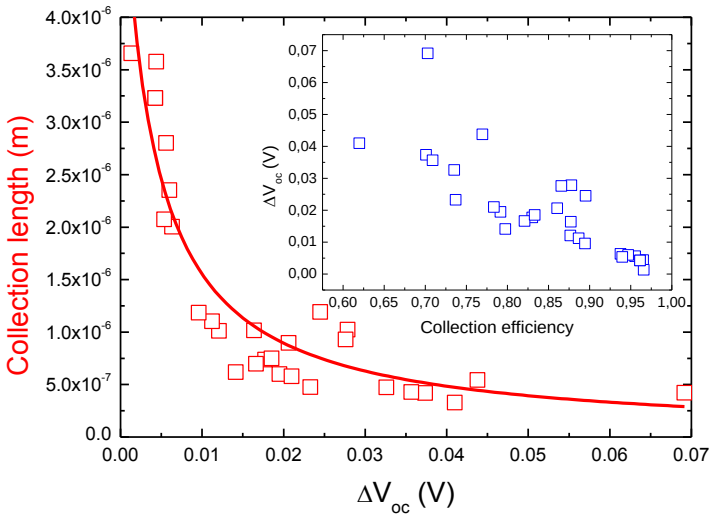

Figure 4-V: Effect of open circuit voltage difference on collection length. Every red square represents a different solar cell. The red line is added as a guide. Inset shows the effect of collection efficiency on ΔV_{oc} .

4.3.3. Effect of light intensity on charge collection efficiency

This section describes the effects of light power on short circuit current density. The generation of this short circuit current is a power law dependent on the intensity of the light according to equation 4-7:

$$J_{sc} \propto P^{\alpha} \qquad \textbf{4-7}$$

Where parameter α depends on the type of carrier recombination and its rate. α equal to unity is represented in *Figure 4-VI* for P3HT:PCBM devices on ITO (red line in *Figure 4-VI*) [23]. α can become less than 1 when BNCD/Cr:Au electrodes are used, as shown in the blue line in *Figure 4-VI*. This is due to several reasons such as bimolecular recombination as discussed in the introduction [23] and interfacial space charge formation [24]. If the system is governed by space charge formation, the minimal value for α is 0.75 when $J_{sc} \propto P^{3/4}$ due to excess trapping of one of the charge types [24]. In the case where the system is governed by bimolecular recombination the value for α can reduce further to values of 0.5 when equal fractions of free electrons and holes are able to recombine with each other in devices. [23]. In chapter 2, the reduced light intensity dependent short circuit resistances and increased bimolecular recombination remained absent. This is due to a different location of the origin of the leakage current. In chapter 2, the reduced short circuit resistances originates due to graphene flakes in the active layer while in this chapter, it is caused by the transparent electrode.

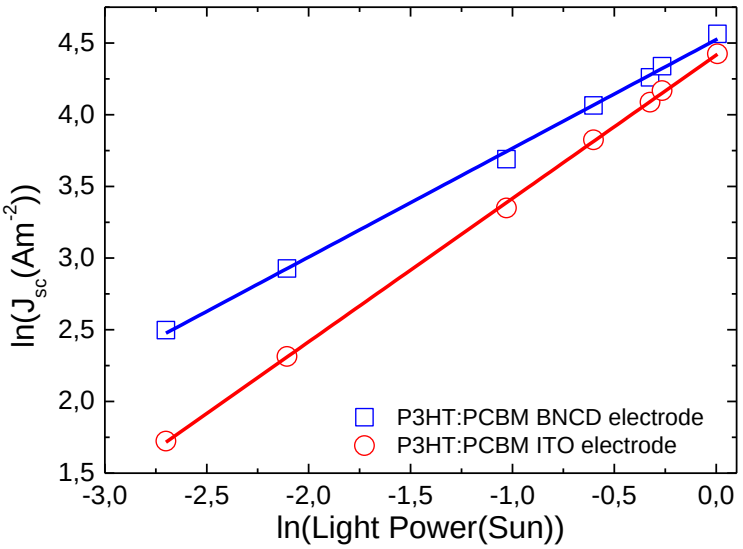

Figure 4-VI: Determination of experimental charge collection efficiency from the slope of short circuit current as a function of light power. The red line (open circles) represents a P3HT:PCBM solar cell based on an ITO electrode. The slope of the line, α, is 1. The blue line (open squares) represent the light intensity dependency of a P3HT:PCBM solar cell based on a BNCD:Cr/Au electrode. α is significantly lower than 1. In this case it is equal to 0.75.

From the section above it was established that the short circuit current is light intensity dependent. In this section the effect of light intensity on the charge collection efficiency is further discussed. In Figure 4-VI, α values are calculated from the light intensity dependent J_{sc}. Figure 4-VII shows the modelled collection efficiency from the light intensity dependent short circuit resistances as a function of α. This figure implies a similar origin for changes in α and the charge collection efficiency since the deviation from α equal from 1 increases when the charge collection efficiency is synchronically decreasing. These values are compared for the different electrodes as used in combination with P3HT:PCBM active layers. Both values are close to 1 for ITO-electrodes, while they reduce significantly when BNCD/Cr:Au electrodes with and without PEDOT:PSS are used. This indicates that the ITO-reference devices give rise to the highest collection efficiencies and barely any recombination loss at short circuit current. BNCD/Cr:Au electrodes show considerably lower collection efficiencies and increased recombination mainly due to low dark short circuit resistances in these devices.

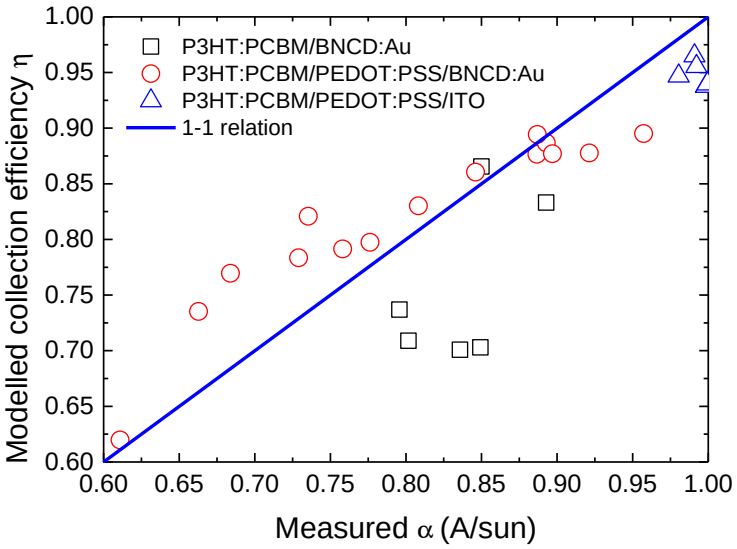

Figure 4-VII: Measured α (A/sun) compared to the modelled collection efficiency from the short circuit resistance. Every point is a different device. ITO devices are shown as blue triangles, BNCD:Cr/Au devices with and without a PEDOT:PSS layer are shown in red circles and black squares respectively.

4.3.4. Effects of charge transfer energy on charge collection efficiency

Here we investigate the effect of BNCD/Cr:Au electrodes on charge transfer using FTPS. In the work of Vandewal et al [1], [2] and Piersimoni et al [3], the effect of changes of the open circuit voltage due to changes in the active layer were investigated by FTPS. The investigated effects were mainly related to specific donor and acceptor materials and their morphological properties. To the best knowledge of the author, the effect of the charge collection efficiency and bimolecular recombination on the charge transfer energy has not been previously investigated.

An example of the charge transfer complex is shown in Figure 4-VIII. The charge transfer complex absorption band appears in a region between 1 eV and 1.5 eV. At 1.8 eV, the absorption peak of PCBM is observed and absorption of P3HT appears at 2 eV.

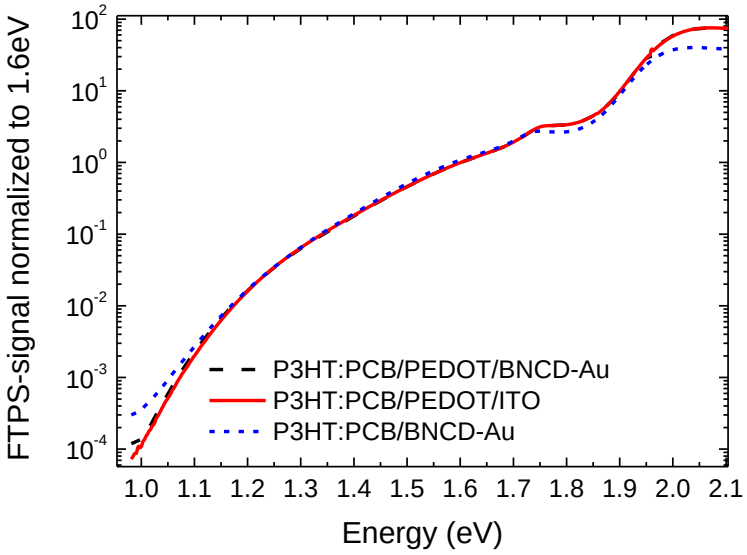

Figure 4-VIII: FTPS- spectra for different studied electrode configurations.

From modelling of the charge transfer complex by the use of Marcus theory, information about the charge transfer energy E_{ct} and reorganization energy λ can be obtained. This is attained by the use of equation 4-8:

$$PC \propto \frac{A}{E\sqrt{4\pi\lambda kT}} \exp\left(\frac{-(E_{ct}-\lambda-E)^2}{4\lambda kT}\right) \qquad \textbf{4-8}$$

Here, E is the light energy, λ the reorganization energy and E_{ct} the charge transfer energy.

The charge transfer energy of 18 BNCD/Cr:Au- P3HT:PCBM (η<0.9) and 6 ITO-P3HT:PCBM (η>0.9) devices were measured and related to the charge collection efficiency in Figure 4-IX. The data showed that decreasing charge transfer energy is related with an increase in charge collection efficiency. Vandewal et al. [1], [2] described the origin of the charge transfer energy as the energy difference between the Fermi level of the electron donor and the Fermi level of the electron acceptor, responsible for a built-in voltage which relates to the open circuit voltage when charge recombination is mainly governed by radiative recombination[12]. The relationship between charge collection efficiency and charge transfer energy indicates the radiative bimolecular origin of the charge collection efficiency when no external voltage is applied. This statement is supported by the fact that observed α values in Figure 4-IX fall below 0.75 towards 0.5 and the absence of S-curves, which are both related to local space charge effects [25], [26]. From these findings it can thus be concluded that JV-characteristics are mainly influenced by bimolecular recombination and reduce charge collection efficiency. This leads to a blue shift of the charge transfer energy in these devices. The shift due to bimolecular recombination can be

caused by depopulation of high energetic states in the bandgap due to recombination of the leaking electrons flowing from the electrode with photogenerated holes in the active layer.

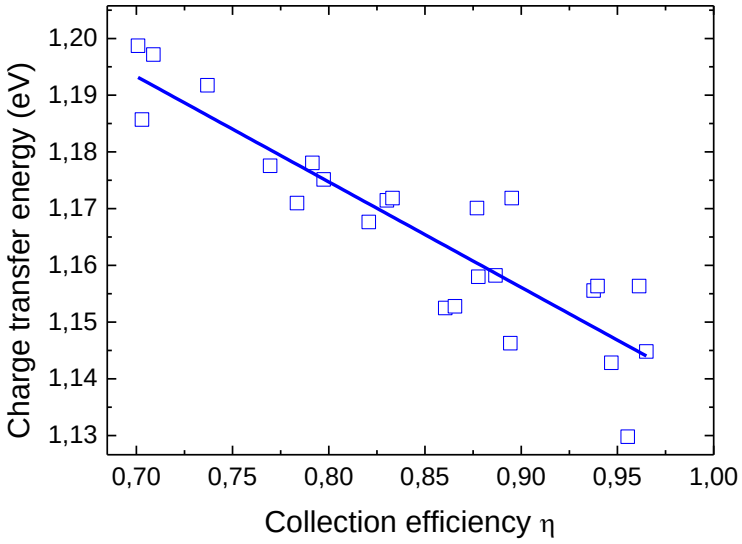

Figure 4-IX: Effect of charge collection efficiency on charge transfer energy. Every point is the charge transfer energy of a solar cell device in relation with its respective charge collection efficiency.

4.3.5. Open circuit voltage in relation with collection efficiency

In order to investigate the influence of non-radiative recombination effects on charge collection efficiency, 25 different devices were prepared under similar conditions but with different electrodes. The devices are compared in Figure 4-X. The collection efficiency is shown as a function of both, the uncorrected V_{oc}, (open symbols) and the built-in voltage (filled symbols).

For ITO devices, V_{oc} is around 0.62 V and collection efficiency is above 0.9. When PEDOT:PSS is used on BNCD/Cr:Au devices, a significant drop in V_{oc} is observed down to a value of 0.58 V. This indicates that the open circuit voltage for BNCD/Cr:Au devices, covered with PEDOT:PSS, can be governed by the work function of PEDOT:PSS.

For uncoated BNCD/Cr:Au electrodes it is seen that the open circuit voltage is further decreased to a value of 0.53 V but the collection efficiency is restored to low values (black squares). This might be possible by pinning of the P3HT Fermi energy level to the gold Fermi level potential leading to more efficient charge collection. By use of Au electrodes covered by PEDOT:PSS, the collection efficiency is again around 1 but at a lower open circuit voltage compared to ITO devices (green top down triangle). When BNCD/Cr:Au electrodes are coated with a PEDOT:PSS layer, open circuit voltages are considerably higher compared to

their uncoated electrodes (red circles). ITO-reference devices give the highest open circuit voltages with improved reproducibility (blue top up triangles). The built-in potential follows the open circuit voltage, indicating that the observed changes are not due to dark shunting effects.

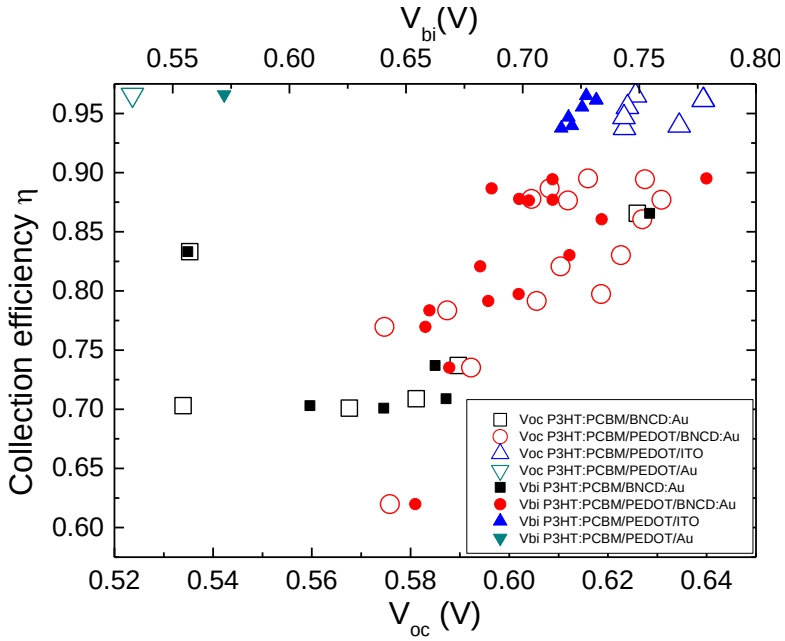

Figure 4-X:Effect of V_{oc} and V_{bi} on collection efficiency. Every point is from a different device. ITO devices are shown as blue triangles, BNCD:Cr/Au devices with and without a PEDOT:PSS layer are shown in red circles and black squares respectively. The filled symbols represent the built-in voltage, and the open symbols represent the open circuit voltage.

By comparing the effects of charge transfer energy (Figure 4-IX) and the V_{oc} (Figure 4-X) with the charge collection efficiency, it can be seen that the effect of the charge transfer energy on the collection efficiency is non-linear with V_{oc}. This occurs in addition to results described in previous works, where a linear correlation was found between the open circuit voltage and the charge transfer energy and the charge collection efficiency was considered to be equal to 1 [27]. In the reported case it is always assumed that the only origin of the open circuit voltage change is the radiative recombination which could be probed by the charge transfer energy [12]. In this case, significant amounts of charge carriers should recombine non-radioactively when charge collection efficiencies are low.

Several groups use the effect of light intensity on open circuit voltage, after deconvolution of the effects of the short circuit resistance, for the determination of the ideality factor and dark saturation current [5][28].

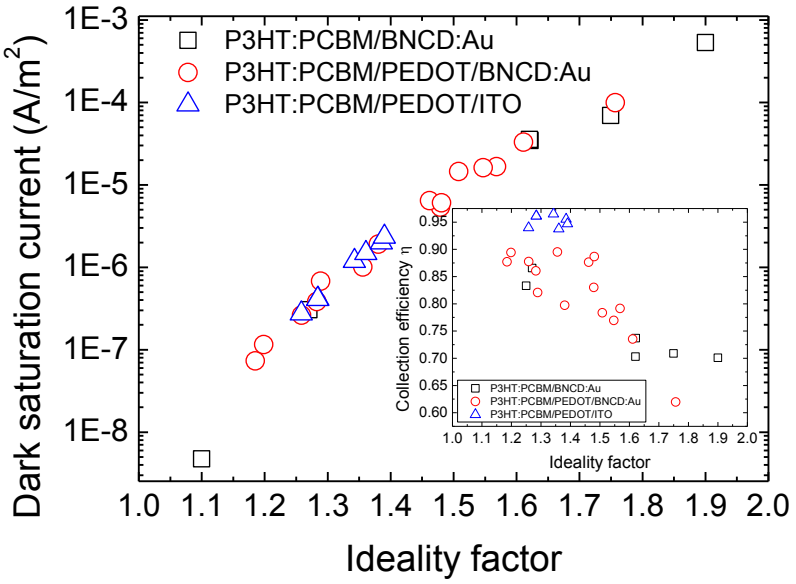

Figure 4-XI: Relationship of ideality factor and dark saturation current of different solar cells. Every point represents a different device. ITO devices are shown as blue triangles, BNCD:Cr/Au devices with and without a PEDOT:PSS layer are shown in red circles and black squares respectively. The inset describes the relation between the ideality factor n with the charge collection efficiency η.

A significant variation in the ideality factor and dark saturation currents for different devices are observed in Figure 4-XI. These differences result from charge carriers which are not only related to transport in the HOMO or LUMO of the device, where hop-diffusion takes place according to the given kT, but also including trap states in the band gap, where considerably higher energies E_t are needed in order to hop to neighboring states [18]. The fact that the ideality factor mainly changes between 1 and 2 is explained by the theory that only free charge carriers, moving with energy kT, can recombine with trapped counter charge carriers moving with an energy of E_t [17], [18]. This induces an ideality factor given by equation 4-9:

$$n_{ideal} = \left(\frac{1}{2} + \frac{kT}{2E_t}\right)^{-1} = \frac{2}{1 + \frac{kT}{E_t}} \qquad \textbf{4-9}$$

Thus when $E_t = kT$, the ideality factor equals 1 and both traps move freely in the device. When $E_t = \infty$, the ideality factor will become 2 [17], [18].

The population of trap states at the interface between the transparent electrode and the active layer can cause a trap induced thermal doping effect, with a thermally activated current increase in the device as a consequence, leading to increased dark saturation currents [14] as shown in Figure 4-XI.

The increase in ideality factor is plotted in relation with a decreasing charge collection efficiency (inset in Figure 4-XI). The highest ideality factors are observed when P3HT:PCBM devices are in direct contact with the BNCD/Cr:Au layer. The ideality factor is lower when a layer of electron blocking PEDOT:PSS is used between the electrodes. This gives a significant increase in charge collection efficiency. The highest charge collection efficiencies are observed for ITO-reference devices.

In summary, from this analysis we can conclude that even if the active layer properties remain unchanged, the extra trap formation at the interface states present near the transparent electrode can significantly influence device characteristics. Photo generated holes can recombine near the electrode with electrons which diffuse from the transparent electrode material and recombine with them, lowering the charge collection efficiencies. This mainly takes place when the electron-blocking capacity of the PEDOT:PSS layer is low or when no PEDOT:PSS layer is present explaining the high occurrence and low charge collection efficiencies in devices with low short circuit resistances.

4.3.6. Origin of recombination in BNCD/Cr:Au electrodes

In order to protect solar cells against electrode induced recombination a thin coating of PEDOT:PSS on BNCD was used. Kelvin probe experiments were performed on BNCD/Cr:Au electrodes before and after coverage by PEDOT:PSS layers. Also, Kelvin probe measurements were performed on reference ITO-electrodes covered by PEDOT:PSS. Measurements on PEDOT:PSS covered ITO reference samples showed a uniform work function of 4.99 eV. Kelvin probe measurements on BNCD/Cr:Au electrodes gave a work function of around 5.11 eV for the BNCD-layer after coverage with PEDOT:PSS. When PEDOT:PSS is not present, the work function is around 4.96 eV for the BNCD-layer and 4.92 eV for the gold part.

Additional electron charge carrier recombination can be caused by the presence of higher electron densities in the Au-grid regions. Since BNCD itself is a high band gap, p-type material, the free electron densities of states is low, and free holes are transported to the BNCD valence band making it an ideal hole transporting material. Au on the other hand is a metallic material with high intrinsic electron densities at its Fermi level. We can thus conclude that when the electrode is covered with PEDOT:PSS, the electrical effects of both BNCD and Au are well homogenized and the electrical properties are mainly governed by the PEDOT:PSS layer as shown in Figure 4-XII.

If the PEDOT:PSS layer is damaged, inhomogeneities create electric shunts in the device, therefore the electrical integrity of PEDOT:PSS is compromised, and leakage currents will appear.

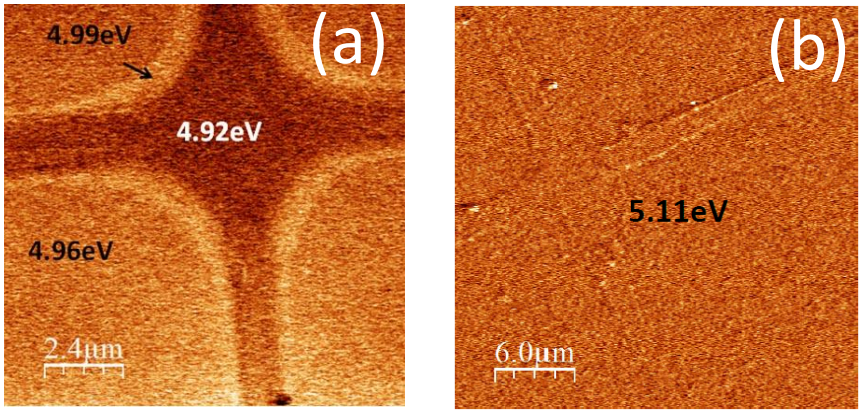

Figure 4-XII: Kelvin probe measurements of a BNCD/Cr:Au electrode under different conditions: (a) without the application of a PEDOT:PSS layer, (b) with the application of a PEDOT:PSS layer.

4.3.7. Optimal solar cell conditions

Based on the set of experiments, carried out in section 4.3.1-6 we can determine optimal parameters for fabricating highly efficiency OBHJ solar cells with BNCD electrodes. In the following section we show how BNCD:Cr/Au electrodes can be applied for charge carrier extraction and -injection in respective organic solar cells. We also compare device characteristics with those of ITO-based reference devices prepared under similar conditions.

4.3.7.1. Optimal solar cell preparation conditions

P3HT:PCBM solar cell devices were prepared on BNCD electrodes with a 36 µm spaced embedded Cr/Au grid and compared to reference devices with an ITO electrode. A standard reference procedure for organic solar cell fabrication using commercial chemical components to fabricate P3HT:PCBM bulk heterojunction cells was used as an active layer. A PEDOT:PSS layer (~40 nm) was deposited on top of the transparent electrode. This layer is used for blocking of back diffused photo generated electrons towards the transparent electrode. An active layer of P3HT:PCBM (thickness ~250 nm) was deposited followed by the deposition of a counter electrode of Ca/Al (~30/~80 nm) (Figure 4-XIII (a)). The JV-characteristics in Figure 4-XIII (b) and the solar cell parameters in Figure 4-XIII show that the power conversion efficiency (η) of the BNCD-Cr/Au electrode (black line) is comparable to the device performance of ITO reference devices (red line) prepared in the same way. The device parameters (J_{sc}, V_{oc}, FFand PCE η_P) are listed in Table 4-1.

4.3.7.2. Solar cell characterization

P3HT- PCBM solar cells prepared according to optimal methodology (See Figure 4-XIII) were characterized by JV measurements.

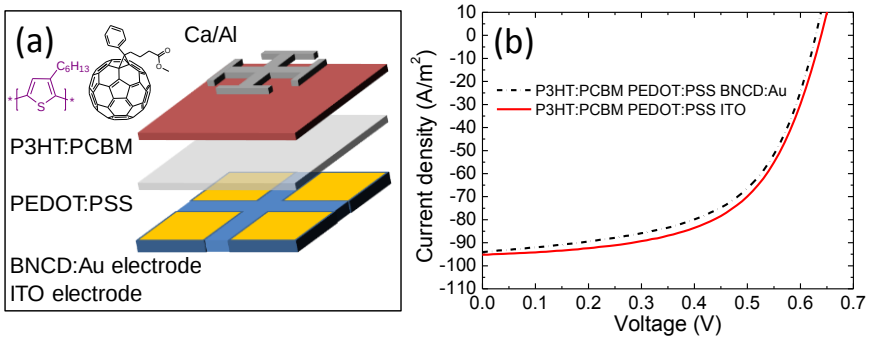

Figure 4-XIII: (a) Schematic layout of an organic solar cell. (b) JV-characteristics of solar cell devices with ITO (red) and BNCD-Cr/Au (black) as a reference electrode. Solar cell parameters are shown in Table 4-1.

From Figure 4-XIV it can be established that the current density is higher for a BNCD layer than for ITO in the measured voltage range. We attribute this fact to increased photo generated hole injection in BNCD compared with ITO due to improved band matching and p-type conduction of BNCD [29]. By comparing device parameters of both devices, it is shown that similar photovoltaic parameters are reached (3.54% ITO reference and 3.38% for the BNCD-Cr/Au device). In fact, taking into account that the metallic grids absorb ~20 % light, theoretically BNCD – P3HT/PCBM devices perform better, with an extrapolated efficiency of 3.9 % compared to 3.54 % of ITO P3HT/PCBM cells.

Table 4-1: Overview of solar cell parameters with short circuit current density J_{sc}, maximal power point current density J_{max}, open circuit voltage V_{oc}, maximal power point voltage V_{max}, fill factor FF and efficiency η. The average values of 4 devices are given with their standard deviations. The values of the best performing cells are given between brackets.

Device setup	***J_{sc} (A/m²)***	***V_{oc} (V)***	***FF***	***η_p***
ITO reference	92.62±1.75 (95.16)	0.64±0.0034 (0.63)	0.5752±0.009 (0.58)	**3.413595±0.094 (3.54)**
BNCD-Cr/Au	94.29±6.02 (93.86)	0.62±0.0045 (0.62)	0.5619±0.014 9 (0.57)	**3.30±0.152 (3.38)**

Although devices based on BNCD/Cr:Au electrodes showed comparable device efficiencies compared to ITO, devices were still affected by significant recombination. Based on the presented measurements we can conclude that boron-doped nanocrystalline diamond (BNCD) can be used as a viable alternative to ITO as a transparent conductive electrode for thin film solar cells and LEDs. We established production methodology for BNCD diamond films with embedded metal (gold) grids, prepared by the use of solution processing, vacuum deposition and photolithography steps. The final electrodes have a transparency of ~70% and a sheet resistance of 20 Ωs/sqr. The BNCD electrode transparency can be further increased by optimizing the collecting grid layout. Organic P3HT:PCBM solar cells on the BNCD/Cr:Au electrodes were prepared with comparable efficiencies.

4.4. Conclusion

To conclude, our BNCD/Cr:Au electrodes exhibit a few short circuit resistance spots compared to ITO-reference devices. Kelvin probe measurements confirmed the electron blocking abilities of PEDOT:PSS. At positions where dark leakage currents are higher, the PEDOT:PSS layers might be damaged, causing increased local electron leakage from the Au electrode in the hole extraction region near the transparent electrode. Due to bimolecular recombination, also the charge transfer energy, as measured with FTPS at short circuit current, is affected by this process. At open circuit voltage conditions, leakage electron current lead to supply of electrons to trap states at the cell interface causing trap assisted recombination. We conclude that performance of our BNCD/Cr:Au hybrid electrodes, can be improved by an electrode coated with a material with high electron blocking characteristics and high adhesion. Use of such a material will reduce electron leakage from the Au-grid in the hole extraction region of the active layer. Although some leakage currents are still present, devices can compete with ITO-devices. By solving leakage current issues, BNCD/Cr:Au devices even have the potential to outperform ITO. The highest obtained efficiency of BNCD/Cr:Au electrodes was (3.38%) compared to ITO (3.54%).

References

[1] K. Vandewal, A. Gadisa, W. D. Oosterbaan, S. Bertho, F. Banishoeib, I. Van Severen, L. Lutsen, T. J. Cleij, D. Vanderzande, and J. V. Manca, "The Relation Between Open Circuit Voltage and the Onset of Photocurrent Generation by Charge Transfer Absorption in Polymer : Fullerene Bulk Heterojunction Solar Cells," *Adv. Funct. Mater.*, vol. 18, no. 14, pp. 2064–2070, Jul. 2008.

[2] K. Vandewal, W. D. Oosterbaan, S. Bertho, V. Vrindts, A. Gadisa, L. Lutsen, D. Vanderzande, and J. V. Manca, "Varying polymer crystallinity in nanofiber poly(3-alkylthiophene): PCBM solar cells: Influence on charge-transfer state energy and open-circuit voltage," *Appl. Phys. Lett.*, vol. 95, no. 12, p. 123303, Sep. 2009.

[3] F. Piersimoni, S. Chambon, K. Vandewal, R. Mens, T. Boonen, A. Gadisa, M. Izquierdo, S. Filippone, B. Ruttens, J. D'haen, N. Martin, L. Lutsen, D. Vanderzande, P. Adriaensens, and J. V. Manca, "Influence of fullerene ordering on the energy of the charge-transfer state and open-circuit voltage in polymer:fullerene solar cells," *J. Phys. Chem. C*, vol. 115, pp. 10873–10880, 2011.

[4] K. Vandewal, K. Tvingstedt, A. Gadisa, O. Inganäs, and J. V Manca, "On the origin of the open-circuit voltage of polymer-fullerene solar cells.," *Nat. Mater.*, vol. 8, no. 11, pp. 904–909, 2009.

[5] S. R. Cowan, A. Roy, and A. J. Heeger, "Recombination in polymer-fullerene bulk heterojunction solar cells," no. July, pp. 1–10, 2010.

[6] S. R. Cowan, J. V. Li, D. C. Olson, and E. L. Ratcliff, "Contact-induced mechanisms in organic photovoltaics: A steady-state and transient study," *Adv. Energy Mater.*, 2014.

[7] C. Voz, J. Puigdollers, J. M. Asensi, S. Galindo, S. Cheylan, R. Pacios, P. Ortega, and R. Alcubilla, "Analysis of the dynamic short-circuit resistance in organic bulk-heterojunction solar cells: Relation to the charge carrier collection efficiency," *Org. Electron. physics, Mater. Appl.*, vol. 14, no. 6, pp. 1643–1648, 2013.

[8] O. J. Sandberg, M. Nyman, and R. Österbacka, "Effect of Contacts in Organic Bulk Heterojunction Solar Cells," *Phys. Rev. Appl.*, vol. 1, p. 024003, 2014.

[9] O. I. Bulk-, P. Sehati, S. Braun, L. Lindell, X. Liu, L. M. Andersson, M. Fahlman, and L. M. Andersson, "Energy-Level Alignment at Metal-Organic and Heterojunction Solar Cells Energy level alignment at metal-organic and organic-organic interfaces in bulk heterojunction solar cells," *Linköping Univ.*, no. 16, pp. 1718–1724, 2011.

[10] V. D. Mihailetchi, P. W. M. Blom, J. C. Hummelen, and M. T. Rispens, "Cathode dependence of the open-circuit voltage of polymer:fullerene bulk heterojunction solar cells," *J. Appl. Phys.*, vol. 94, no. 10, pp. 6849–6854, 2003.

[11] Q. Bao, O. Sandberg, D. Dagnelund, S. Sandén, S. Braun, H. Aarnio, X. Liu, W. M. Chen, R. Österbacka, and M. Fahlman, "Trap-assisted recombination via integer charge transfer states in organic bulk heterojunction photovoltaics," *Adv. Funct. Mater.*, pp. 1–8, 2014.

[12] K. Vandewal, K. Tvingstedt, A. Gadisa, O. Inganäs, and J. V Manca, "On the origin of the open-circuit voltage of polymer–fullerene solar cells," *Nat. Mater.*, vol. 8, no. 11, pp. 904–909, Nov. 2009.

[13] R. Turton, *The Physics of Solids*. 2000.

[14] P. Baruch, A. De Vos, P. T. Landsberg, and J. E. Parrott, "On some thermodynamic aspects of photovoltaic solar energy conversion," *Sol. Energy Mater. Sol. Cells*, vol. 36, no. 2, pp. 201–222, Feb. 1995.

[15] R. a. Street, M. Schoendorf, a. Roy, and J. H. Lee, "Interface state recombination in organic solar cells," *Phys. Rev. B*, vol. 81, no. 20, p. 205307, May 2010.

[16] *Physics of Solar Cells: From Basic Principles to Advanced Concepts*. 2009.

[17] T. Kirchartz and J. Nelson, "Meaning of reaction orders in polymer:fullerene solar cells," *Phys. Rev. B - Condens. Matter Mater. Phys.*, vol. 86, pp. 1–12, 2012.

[18] J. C. Blakesley and D. Neher, "Relationship between energetic disorder and open-circuit voltage in bulk heterojunction organic solar cells," *Phys. Rev. B - Condens. Matter Mater. Phys.*, vol. 84, 2011.

[19] K. Vandewal, L. Goris, I. Haeldermans, M. Nesládek, K. Haenen, P. Wagner, and J. V Manca, "Fourier-Transform Photocurrent Spectroscopy for a fast and highly sensitive spectral characterization of organic and hybrid solar cells," *Thin Solid Films*, vol. 516, no. 20, pp. 7135–7138, Aug. 2008.

[20] J. Merten, J. M. Asensi, C. Voz, a. V. Shah, R. Platz, and J. Andreu, "Improved equivalent circuit and analytical model for amorphous silicon solar cells and modules," *IEEE Trans. Electron Devices*, vol. 45, no. 2, pp. 423–429, 1998.

[21] R. S. Crandall, "Modeling of thin film solar cells: Uniform field approximation," *J. Appl. Phys.*, vol. 54, no. 1983, pp. 7176–7186, 1983.

[22] V. D. Mihailetchi, L. J. A. Koster, J. C. Hummelen, and P. W. M. Blom, "Photocurrent Generation in Polymer-Fullerene Bulk Heterojunctions J ph [A / m]," no. November, pp. 19–22, 2004.

[23] L. J. A. Koster, M. Kemerink, M. M. Wienk, K. Maturová, and R. a J. Janssen, "Quantifying bimolecular recombination losses in organic bulk heterojunction solar cells," *Adv. Mater.*, vol. 23, pp. 1670–1674, 2011.

[24] V. Mihailetchi, J. Wildeman, and P. Blom, "Space-Charge Limited Photocurrent," *Phys. Rev. Lett.*, vol. 94, no. 12, p. 126602, Apr. 2005.

[25] A. Wagenpfahl, D. Rauh, M. Binder, C. Deibel, and V. Dyakonov, "S-shaped current-voltage characteristics of organic solar devices," May 2010.

[26] J. Wagner, M. Gruber, A. Wilke, Y. Tanaka, K. Topczak, A. Steindamm, U. Hörmann, A. Opitz, Y. Nakayama, H. Ishii, J. Pflaum, N. Koch, and W. Brütting, "Identification of different origins for s-shaped current voltage characteristics in planar heterojunction organic solar cells," *J. Appl. Phys.*, vol. 111, no. 5, p. 054509, Mar. 2012.

[27] K. R. Graham, P. Erwin, D. Nordlund, K. Vandewal, R. Li, G. O. Ngongang Ndjawa, E. T. Hoke, A. Salleo, M. E. Thompson, M. D. McGehee, and A. Amassian, "Re-evaluating the role of sterics and electronic coupling in determining the open-circuit voltage of organic solar cells," *Adv. Mater.*, vol. 25, pp. 6076–6082, 2013.

[28] T. Kirchartz, F. Deledalle, P. S. Tuladhar, J. R. Durrant, and J. Nelson, "On the differences between dark and light ideality factor in polymer:Fullerene solar cells," *J. Phys. Chem. Lett.*, vol. 4, pp. 2371–2376, 2013.

[29] Y. L. Zhong, A. Midya, Z. Ng, Z.-K. Chen, M. Daenen, M. Nesladek, and K. P. Loh, "Diamond-based molecular platform for photoelectrochemistry.," *J. Am. Chem. Soc.*, vol. 130, no. 51, pp. 17218–9, Dec. 2008.

Chapter 5 General conclusions and future work

The key motivation for this work was the investigation of the interfacial behavior of carbon-based materials, in particular graphene and diamond along with polymers and how these carbon materials can be utilized for organic photovoltaic applications. Understanding of the fundamental properties of these materials is necessary for further commercialization of such devices.

The following research questions were investigated in this work:

1. *What effect will graphene have on thin polymer:fullerene solar cell devices when graphene is used as a ternary component in the active layer at densities below percolation densities?*
2. *Is it possible to construct transparent electrodes based on diamond, replacing Indium Tin oxide (ITO) and what are the physical characteristics of the diamond electrodes?*
3. *Is it possible to use these diamond based electrodes for Polymer Light Emitting Diodes (PLED) and Organic Photovoltaic (OPV) devices?*

5.1. General conclusions

5.1.1. Graphene as a third component in donor:acceptor organic solar cells

In organic solar cells, a combination of two components are normally used in the photo-active layer: an electron donating material (e.g. conjugated polymer) and an electron accepting material (e.g. a fullerene derivate). In this work, the influence of the addition of a third component, graphene, was investigated. In particular, the effect of graphene on the regulation of the charge transport is studied.
In Chapter 2 we identified the threshold concentration for graphene in thin film solar cells to form conductive percolations and investigate the effects of graphene below this threshold value. When graphene is used above the threshold fraction, the graphene flakes start to cluster. The addition of low concentrations of graphene in P3HT:PCBM solar cell devices induces a balance of hole- and electron transport mobilities. This leads to more efficient photocurrent devices. The enhancement of hole mobility results from the enhanced P3HT crystallinity in the active layer after graphene addition. These two effects result in the electron and hole mobilities balancing out. This result demonstrates improved charge extraction efficiencies and ultimately in higher efficiency and improved solar cell device performance.

5.1.2. BNCD:Cr/Au as a transparent electrode for organic electrical applications

An important challenge for future opto-electronic applications is the replacement of expensive and scarce Indium Tin Oxide (ITO) by new highly stable and transparent electrodes. In chapter 3, we have developed a BNCD electrode as an alternative to ITO. A gold metal grid is integrated in transparent BNCD layers. This is achieved using procedures involving lithography, metal depositions and wet and dry etching. This procedure results in thin, highly transparent electrodes with sheet resistance values below 20 Ω/sqr. These new electrodes are usable in

applications involving charge injection, such as PLEDs or solar cells. They show improved hole injection and transport performance compared to ITO.

Charge extraction properties in solar cell are further investigated in Chapter 4. We describe a procedure to analyze the effects of dark and light induced leakage currents from JV-characteristics. We see that higher leakage currents are present in the devices where BNCD/Cr:Au electrodes are used compared to ITO. Kelvin probe measurements on BNCD:Cr/Au electrodes, covered with PEDOT:PSS demonstrates how PEDOT:PSS can influence the surface work function when deposited on the underlying BNCD:Cr/Au layer. At positions where dark electrical leakage currents are high, the PEDOT:PSS layers might be damaged. This causes increased local electron leakage from the Au electrode to the active layer. Under high internal electrical fields or high current, the leaking electrons from the Cr/Au grid are recombining with the photo generated free holes in a bimolecular fashion. Therefore, the drift lengths and the related collection efficiency of photo generated charge carriers are reduced. The charge transfer energy, as measured by FTPS at short circuit current, is altered when using BNCD:Cr/Au electrodes. Therefore, we must emphasize that for the development of hybrid transparent electrodes, the effects of leakage currents should be reduced as much as possible. Also, an electron blocking material with a good suture to the metal grid of the electrode should be used in order to reduce electron leakage from the Au-grid, enhancing the open circuit voltage and device efficiency.

5.2. Future work

Since this work consists of an investigation of the possible use of BNCD and graphene in organic electronic applications, both subjects handled in this work highlight questions for further investigation.

5.2.1. Graphene as a charge transport mediator

Although we showed in this work that graphene-polymer composites can be utilized in the active layer of solar cells, only a minority of many possibilities have been addressed. Electrical properties can be further optimized by doping and chemical functionalization. In addition other 2D material systems could be used.

Currently, graphene has only been used in polymer-solutions, but other less viscous alternatives such as monomer solutions can be used. Graphene can be studied by in situ polymerization which can enhance its solubility in the resulting polymer matrix.

Also further study toward graphene flake orientation and charge selectivity in the film is important to modulate the electrical properties of the composite. This could further enhance the electrical properties of the composite in the active layer of solar cells.

5.2.2. BNCD:Cr/Au as a transparent electrode for organic electrical applications

Further investigation necessary for BNCD:Cr/Au electrodes for OLEDS, should focus on improvement of the out-coupling of the light from BNCD, which has a

high refractive index, towards the environment. For now a squared metal pattern is used. When working towards large area application of the electrode, other metal structures can give more advantages. Also the line width of the grid can be reduced leading to higher transparency. Other glass materials can also be used as an alternative for expensive fused silica substrates. Thermal conductivity properties of electrodes (which is anticipated to be high) should be investigated in more detail. Thermal transport is easier through thicker high purity diamond layers, while the surface roughness can increase, therefore a balance between the two must be found. Also the electrical charge carrier mobility in the BNCD layer should be further investigated and increased to reduce the resistance of the layer. In order to reduce interfacial charge recombination, surface polishing and surface modification could be further investigated to enhance electron blocking.

Appendix 1 Materials and methods

In this chapter we describe the materials and methods used during this thesis. First we would like to explain briefly the material preparation and processing in the following subchapters:

- Diamond growth
- Graphene solution preparation
- Photolithography
- Solar cell preparation

The characterization techniques section consists out of

- Optical characterization
- Sheet resistance measurements
- JV-characterization
- Mobility measurements using field effect transistors
- Additional techniques
    - Mobility measurements using CELIV
    - Raman spectroscopy
    - Atomic force microscopy and Kelvin probe microscopy
    - Scanning- and transmission electron microscopy

1.1. Materials

1.1.1. Diamond growth

For BNCD diamond growth, fused silica substrates were cleaned using RCA1 and RCA2 cleaning techniques. Afterwards, samples were immersed in a suspension of 4 nm -Bucky Diamond diluted to 0.33 g/L for 1 min and then spin coated at 4000 rpm with water sprayed on top in order to achieve uniform surface coverage. Samples were grown in an Astex AX6550 microwave plasma enhanced chemical vapor deposition system with the conditions as follows: base pressure was less than 2.6E-8 Bar, working pressure was 2.6E-2 Bar, microwave power was 3500 W, stage was heated by plenum on underside of the puck. Growth time lasted approximately 2 hours. Flow rates were 380 sccm H_2, 20 sccm CH_4, 100 sccm TMB (TMB is diluted with H_2), so the methane composition was 4%, and the boron to carbon ratio was 5000 ppm.

The samples were then treated using an oxygen plasma (150 W 50% valve 50 sccm) for 2.5 min. Afterwards, the sample was dipped in Al etchant A to under etch the W layer for making a lift off structure. In the end, Cr/Au was deposited using the Cu negative as a mold. Afterwards the places where the Cu resided were etched away by Al etchant A and the Cr/Au structure remained.

1.1.2. Graphene solution preparation

The aim of this work was to prepare graphene flakes of ultra-small sizes that can be further used in dispersion for BHJ preparation. Centrifugation is an important tool in order to separate the graphite particles form the dispersed graphene flakes. Centrifugation is a process that involves the use of the centrifugal force for the sedimentation of heterogeneous mixtures with a centrifuge. This process

is used to separate two immiscible materials in a blend. Components with higher density of the mixture migrate away from the axis of the centrifuge, while less dense components of the mixture migrate towards the axis. The effective gravitational force on a test tube can be raised to increase the efficiency and speed of pellet formation on the bottom of the tube.

In this work, 100 mg of graphite flakes (Sigma Aldrich Ltd.) were dispersed in 10 ml of 1.2-dichlorobenzene. The solvent was chosen for its compatibility with P3HT:PCBM [1]. Moreover, 1.2-dichlorobenzene (ODCB) has a surface tension~37 mN/m [2], close to that o(to extend f ideal solvents for the dispersion of the exfoliated flakes, such as N-Methyl-2-Pyrrolidone [3], that minimize the interfacial tension between the liquid and graphene flakes [4]. The dispersion was then ultrasonicated for 10 hours and subsequently ultracentrifuged, exploiting sedimentation-based separation [4]–[7], using a TH-641 swinging bucket rotor in a Sorvall WX-100 ultracentrifuge at 15000-, 25000 and 35000 rpm (~151000g) for 30 min. After ultracentrifugation, the supernatant was extracted by pipetting. The concentration of graphitic flakes was determined from the optical absorption coefficient at 660 nm, as described in Refs. [4]–[6].

1.1.3. Photolithography

Contact lithography is used to prepare the transparent electrodes. This technique was applied in this work in order to develop BNCD/Cr:Au hybrid electrodes. Generally, there are two ways in order to generate patterns with photolithography: positive - and negative lithography. In both types, a photoresist layer is first deposited on top of the substrate. In order to perform a first solidification step, the substrates with the polymer are baked during a first baking step. After baking, the solidified layers are selectively exposed to UV-light to transform the resist material. Here, the positive photoresist gets cross-linked during UV-treatment, while negative photoresists gets degraded. After UV-exposure, sometimes, a second baking step is performed in order to further crosslink the samples. In the end, the samples are developed. This means that they are rinsed in a developer in order to remove non-cross-linked photoresist.

During, this work both negative and positive resists were used in order to prepare the samples. The negative resist used here is NR-9 from Futurex. Before starting the photoresist procedure, the substrates were cleaned using RCA1 and RCA2 cleaning steps. During this process organic and ionic contaminants are removed from the sample. RCA1 cleaning was performed using a mixture of H_2O:H_2O_2:NH_3 (5:1:1) at 70°C during 10 min. Hereafter, a RCA2 cleaning step was performed where the samples were treated again for 10 min at 70°C in a mixture of H_2O: H_2O_2:HCl (6:1:1). After cleaning, the samples were thoroughly rinsed with DI H_20 and dried using a N_2 gun.

For the NR9 photolithography, a layer of NR9 was spin coated on top of the substrate. This was performed for 40 s at 5000 rpm. The prebake was done for 3 min at 150°C, followed by 30 s of exposure by UV-light by the use of a Karl Suss ma 55. After the selective exposure of the photoresist, the layers were post-baked for 3 min at 100°C. This was followed by a development step 17 s. After patterning, a layer of 20 nm of Cr and 80 nm of Au was deposited on top of the patterned substrate. After metal deposition, the remaining photoresist

was removed by rinsing the sample with acetone for several minutes or even hours until all the photoresist was removed and the remaining pattern was the same as the one on the photolithographic mask.

For S1818 patterning the following procedure was used. A polymer mall for the metals was prepared by S1818 photolithography. The substrates were dehydrated at 195°C for 5 min. Afterwards a LOR-3B layer was deposited by spin coating at a speed of 2000 rpm for 45 s. The samples were baked at 195°C for 5 min. Afterwards a layer of S1818 was deposited by spin coating at 3000 rpm for 30 s. After a second baking step at 125°C for 1 min, the polymer layer was patterned using lithography. Then the sample was developed using a 1:10 water:TMAH solution.

After patterning, 20 nm of titanium was deposited by sputtering to act as an adhesion enhancer between the copper layer and the diamond. Afterwards a 400 nm copper layer was deposited. This was followed by the deposition of a tungsten layer of around 100 nm. After the tungsten deposition, the photoresist was removed from the substrate by rinsing the sample in acetone. To be sure that all the S1818/LOR-3B is removed, the sample was soaked in Remover PG at 60°C for 20 min.

1.1.4. Solar cell preparation

1.1.4.1. Graphene section

The P3HT:PCBM solar cells tested in this work consist of an active layer formed by an electron donating polymer Poly(3-hexylthiophene-2,5-diyl) (P3HT), and a well-known electron acceptor [35], (6,6)-Phenyl C61 butyric acid methyl ester (PCBM), a fullerene derivative [35]. The P3HT:PCBM dispersion was prepared with 10 mg/ml P3HT (Rieke) and 8 mg/ml PCBM (Solenne B.V.) and stirred under nitrogen atmosphere for 24 h at 50°C.

Glass substrates with a 100 nm indium tin oxide (ITO) coating were cleaned for 20 min by ultrasonic treatment in aqueous surfactant (BUEHLER ultramet 2 sonic cleaning) solution (surfactant:water, 1:20). Afterwards they were ultrasonicated in acetone for 15 min, boiled (~82°C) in isopropanol for 15 minutes and finally dried under a nitrogen flow. After cleaning, an ozone treatment was performed for 15 min in order to remove further carbon-based trace elements.

A layer of PEDOT:PSS (Stark) was deposited by spin coating at 3000 rpm for 40 s. The layers were then annealed for 20 min at 120°C. After cooling, a 100 nm layer of the active blend (P3HT: PCBM: graphene) was deposited on the PEDOT:PSS by spin coating for 40 s at 750 rpm in N_2 atmosphere. After this procedure, the layers were slowly dried for~1 h. Finally, a counter electrode of 20 nm Ca and 60 nm Al was deposited by evaporation.

1.1.4.2. BNCD/Cr:Au electrode section

The P3HT:PCBM solar cells tested in this work consist of an active layer formed by an electron donating polymer Poly(3-hexylthiophene-2,5-diyl) (P3HT), and a well-known electron acceptor, (6,6)-Phenyl C61 butyric acid methyl ester (PCBM), a fullerene derivative. The P3HT:PCBM dispersion was prepared with 20

mg/ml P3HT (Rieke) and 16 mg/ml PCBM (Solenne B.V.) and stirred under nitrogen atmosphere for 24 h at 50°C.

A similar cleaning procedure was used in order to clean the BNCD/Cr:Au electrodes. Importantly, any type of manual mechanical cleaning was avoided during this work in order to preserve the integrity of the Au-grid in the BNCD-layer. In order to remove macroscopic organic remains, samples were soaked in water in order to dissolve PEDOT:PSS layers, causing the lift off of the active layer and counter electrodes. When no PEDOT:PSS was used, the samples were soaked in ODCB until the active layer was removed. Abundant rinsing with acetone was applied in order to remove further remains of ODCB. Furthermore, samples were cleaned for 20 min by ultrasonic treatment in aqueous surfactant (BUEHLER ultramet 2 sonic cleaning) solution (surfactant:water, 1:20). Afterwards they were ultrasonicated in acetone for 15 min, boiled (~82°C) in isopropanol for 15 min and finally dried under a nitrogen flow. After cleaning, an ozone treatment was performed for 15 min in order to remove further carbon-based trace elements.

A layer of PEDOT:PSS (Stark) was deposited by spin coating at 3000 rpm for 40 s. The layers were then annealed for 20 min at 120°C. After spin coating, the samples were baked in nitrogen atmosphere in order to dehydrate the PEDOT:PSS layer. After cooling, a 250 nm thick layer of the active blend (P3HT:PCBM) was deposited on the PEDOT:PSS by spin coating for 40 s at 800 rpm in N_2 atmosphere. After this process the layers were slowly dried for~1 h followed by a thermal annealing step at 130°C for 10 min. The annealing was always done before counter electrode deposition. The electrode deposition was done by thermal evaporation at base pressure of 10E-7 mBar. Ca (30 nm)/Al (100 nm) electrodes were evaporated on top of the active layer in order to complete the device.

1.2. Measurement methods

1.2.1. Optical measurements

After a short introduction to the use of light to characterize materials, two ways used in this work to characterize samples are described.

The position dependent property that describes the interaction of light with the material is the refractive index. In a simple representation of a light ray, light is represented by a line that can bounce back or be transmitted at any interface with changing refractive indices. This behavior is mainly described by Snells law as given below.

$$n_1 \sin(\theta_1) = n_2 \sin(\theta_2)$$

Here, n_1 and n_2 are the real parts of the refractive index of the material and the incoming and outgoing angles are denoted resp. θ_1, θ_2. The critical angle is the incident light angle where the refracted light angle becomes 90° with respect to the normal distribution, in other words total internal reflection. According to Snell's law, this critical angle is given by:

$$\theta_{cryt} = a\sin\left(\frac{n_{electrode}}{n_{activelayer}}\right)$$

This law is useful in many thin film applications ranging from anti-reflective coatings to fiber optics. Also in OLED devices it is important in order to determine the output efficiency of the devices. The relation between the critical angle and the light output in light emitting diodes is thoroughly investigated. Analytically, a simple approximating expression is derived in [8], [9] and is given by:

$$\frac{\eta_{encapsulated}}{\eta_{unencapsulated}} = \frac{1-\cos\left(\theta_{cryt,encapsulation}\right)}{1-\cos\left(\theta_{cryt,air}\right)}$$

Where η is the light out coupling efficiency between encapsulated and un-encapsulated conditions. θ is the critical angle between the polymer layer and air (air) and between the polymer layer and the encapsulation system (encapsulated). A better approximation of this relation can be obtained by numeric calculations [10].

In the beginning of 20th century, the wavelike character of light became more and more understood. Every wavelike function can by described by 2 goniometric fields, orthogonal to each other and oscillating in the direction of the ray. These two goniometric fields are the magnetic and electrical field. Since the electrical field is most important for the description of light-matter interactions, we will focus on this here. The goniometric function describing the electrical field of light rays is given by:

$$E = E_0 \cos(\omega t + \delta - kr)$$

Where ω described the time (t) dependent part, k represents the position (r) dependent part and δ, the phase shifting occurring during interface transitions. Since every goniometric function can be described in complex form according to Eulers law, the electrical field has the same possibility since $\cos(x) = \mathrm{Re}(\exp(ix))$. Thus the electrical field can be described by:

$$E = E_0 \, Re(exp(i(\omega t + \delta - kr))) = E_0 \, Re(exp(i\omega t)\, exp(i\delta)\, exp(-ikr))$$

The positional term k, which is of main importance in this work, can be expressed in terms of a wavelength as:

$$k = \frac{2\pi}{\lambda}$$

When light from a vacuum travels with a speed of c_0 (~300000km/s) meets a denser medium, it has to slow down its speed to c_1 due to the electrical polarization induced by the medium. The refractive index n change is

represented as $n_0/n_1 = c_1/c_0$. Since the frequency of the light ν should remain constant, the following relation holds:

$$\nu = \frac{c_0}{\lambda_0} = \frac{c_1}{\lambda_1}$$

Or

$$\lambda_1 = \lambda_0 \frac{c_1}{c_0} = \lambda_0 \frac{n_0}{n_1}$$

For vacuum n_0 is equal to 1. λ_0 is the vacuum wavelength of the light and λ_1 is the wavelength in the medium with refractive index n_1. The expression for k can thus be modified to:

$$k = \frac{2\pi n_1}{\lambda_0}$$

Where n_1 is a complex number $(n + i\kappa)$. The last part of the electrical field expression can be expressed as:

$$exp(-ikr) = exp\left(-i \cdot \left(\frac{2\pi n_1}{\lambda_0}\right) r\right) = exp\left(-i \cdot \left(\frac{2\pi(n + i\kappa)}{\lambda_0}\right) r\right)$$
$$= exp\left(-i \cdot \left(\frac{2\pi n r}{\lambda_0}\right) - \left(\frac{2\pi\kappa}{\lambda_0}\right) r\right) = exp\left(-i \cdot \left(\frac{2\pi n r}{\lambda_0}\right)\right) exp\left(-\left(\frac{2\pi\kappa}{\lambda_0}\right) r\right)$$

A photodetector measures light intensity I equal to $I = |E|^2$. The distance part of the electrical field as discussed in the previous expression is thus equal to:

$$\frac{I(r)}{I(0)} = exp\left(-\left(\frac{4\pi\kappa}{\lambda_0}\right) r\right) = exp(-\alpha r)$$

Here, $I(0)$ represents the light intensity falling on the sample and $I(r)$ is the light intensity that remains at position r inside the sample. This law is also known as Lambert-Beer. n represents the refractive index as described above.

Films can thus reflect, transmit, absorb or scatter light. These properties are a function of the light energy expressed in wavelength or eV. All of the light rays falling on the sample will undergo one of these four processes. Reflected and scattered light rays are measured by the light intensity returned at the specular angle and at non-specular angles. Scattering increases with surface roughness, sample contamination and bulk inhomogeneity in transparent materials. Absorption and transmission from the infrared to the ultraviolet can be determined by appropriate spectroscopy techniques.

Light transmittance by a material can be defined as the intensity that can be detected after transmission through a material compared to the intensity falling on the sample. Transmittance measurements are an important property for the development of transparent electrodes as discussed in the introduction. In this work a hybrid electrode consisting out of a low transparent and high conductive Au grid and a high transparent and more resistive BNCD layer was developed. Based on Lambert-beer law the absorbance (A) is determined from the transmittance (T) by $A = -log(T)$. Since the absorbance of materials are additive, the hyrbrid transmittance can be given by:

$$T(d) = 10^{-\left(A_{Au}\left(\frac{b^2-(b-d)^2}{b^2}\right)+A_{BNCD}\left(\frac{(b-d)^2}{b^2}\right)\right)}$$

Where b is the size of the unit cell and d is the size of the BNCD square. $A_{BNCD} = -log(T_{BNCD})$ is the absorbance of the BNCD layer on top of a fused silica substrate. T_{BNCD} is the transmittance of BNCD. $A_{Au} = -log(T_{Au})$ is the absorbance of a pure Cr/Au layer on top of the fused silica substrate. T_{Au} is the transmittance of a pure Cr/Au layer on top of the fused silica substrate. The transmittance of pure diamond is around 80% and of the Cr/Au layer is around 10%.

Transparency measurements are performed using a measurement setup where the solar simulator Newport Oriel class A, equipped with a Xenon Short Arc lamp with 150 W power (1 sun at 1.5 air mass density, *i.e.* 100 mW/cm^2) is used as a light source. A photodiode covered by a non-transparent sheet with a pinhole with 1 mm diameter is used in order to detect the amount of transmitted light. In order to prevent saturation of the photodiode, a neutral density filter is applied just above the photodiode. The electrical current generated in the diode is detected using a Keithley 2400 multimeter. The light transmission through the transparent electrode material is defined as:

$$T_{tot} = \frac{I_{with\ sample}}{I_{without\ sample}}$$

Where $I_{with\ sample}$ represents the measured current ~~represents~~ in the presence of a sample and $I_{without\ sample}$, the measured current in absence of a sample.

As shown before, the analysis of the optical properties expressed by the dielectric function or the complex index of refraction n+ik has been a subject of detailed studies for decades[11], [12]. Among the widely used methods to investigate the optical properties of thin films on transparent substrates belong the optical transmittance T, reflectance R and absorptance A spectroscopy [13]. The salient feature of the low-absorbing thin film with thickness d is the presence of the interference fringes in the optical spectra which depend on d(n+ik) product and via $n(\lambda)+ik(\lambda)$ are related to the wavelength λ of the incident light. Thicker films give more maxima and minima in a given wavelength range

than thinner films, and the maxima and minima are closer than for thinner films. On the other hand ultrathin films are unique in the absence of the interferences.

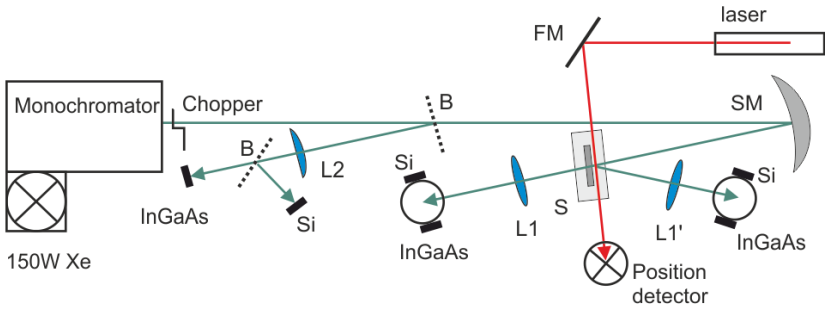

Figure 1-I: The photo thermal deflection spectroscopy (PDS) setup. 150 W Xe lamp and monochromator as a monochromatic light source, mechanical chopper (Ch), He-Ne laser as a probe beam source, beamsplitter (B), spherical mirror (SM), flat mirror (FM), detectors Si and InGaAs attached to the integrating sphere, focusing lenses (L1-4), position detector (PD) and sample (S) immersed in liquid.

The photothermal deflection spectroscopy (PDS) setup is shown in Figure 1-I. The sample is immersed in the transparent liquid (Florinert FC72) and periodically illuminated by the monochromatic light from the 150 W Xe lamp equipped by the monochromator with ultraviolet, visible and infrared gratings and a chopper operating on low frequency 13Hz. About 8% of the light is deflected by the beamsplitter into the integrating sphere equipped with Si and InGaAs photodiodes to monitor the light intensity. This compound detector can detect the spectrum in the broad spectral range from UV to near infrared region from 250 to 1700 nm. The signal from the detectors is coupled via the multiplexer Signal Recovery 3830 to the current preamplifier and a lock-in amplifier referenced to the chopper frequency. The compound detectors are also placed in front and behind the sample S to detect the reflectance and transmittance spectra, whereas the relative absorbance spectra are detected by the position detector monitoring the laser beam parallel to the sample surface. The absorbed heat in the thin film on glass substrate generates the periodical thermal waves in the liquid surrounding the sample causing the periodical deflection of the laser beam. The amplitude of the deflection normalized on the black sample (such as carbon nanotubes thin film on glass) spectra gives the optical absorption of thin film.

The dielectric function of thin film is evaluated from the reflectance and absorptance spectra using the commercial software FilmWizard (http://www.sci-soft.com/). First, the parameters of a suitable model describing the real and complex index of refraction are fitted together with the film thickness. In the case of B-doped NCD the Lorentz Oscillator and Drude model were applied to describe both bandgap absorption and the absorption on free carriers. The surface scattering is modeled by effective media approximation [14].

Once the index of refraction, the thin film thickness and the surface roughness are known, the optical absorption coefficient is calculated from the absorptance spectrum (A) or in the case of smooth film from A/T using Ritter-Weiser model [15].

1.2.2. Sheet resistance measurements

For metals and metallic like materials, the resistivity (Ω/cm) is one of the most important electrical properties, since it is the material dependent property that defines the bulk resistance R (Ω) of the material.

When using thin films, it is more convenient to think in terms of the resistance of a square film between the edges. This resistance is known as the 'sheet resistivity' (Ω/sqr) and for a squared electrode with a length b, width b and height h it is obtained by:

$$R = \rho \frac{b}{A} = \rho \frac{b}{bh} = \frac{\rho}{h} = R_{sh}$$

R_{sh} is thus independent of the cross sectional path and thus mainly affected by the film thickness.

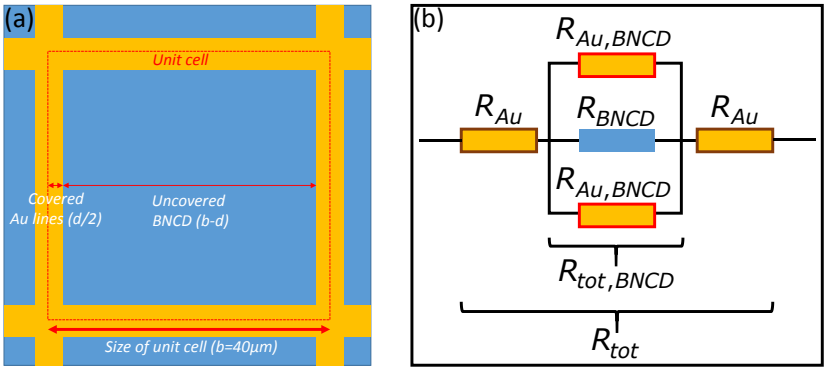

Figure 1-II: (a) Parameter schematization for transmission and sheet resistance modelling. (b) Equivalent resistance scheme for sheet resistance calculation from scheme in (a).

The sheet resistance of our hybrid transparent electrodes, as schematized in Figure 1-II, is theorized as follows:

$$R_{tot} = 2R_{Au} + R_{tot,BNCD}$$

Where R_{Au} is given by:

$$R_{Au} = \rho_{Au} \frac{\left(\frac{d}{2}\right)}{bh} = R_{sh(Au)} \frac{d}{2b}$$

With ρ_{Au} is the resistivity of gold. $R_{tot,BNCD}$ is given by

$$\frac{1}{R_{tot,BNCD}} = 2\frac{1}{R_{Au,BNCD}} + \frac{1}{R_{BNCD}}$$

With

$$R_{Au,BNCD} = \rho_{Au} \frac{b-d}{\frac{d}{2}h} = 2R_{sh,Au} \frac{b-d}{d}$$

And

$$R_{BNCD} = \rho_{BNCD} \frac{b-d}{(b-d)h} = R_{sh,BNCD}$$

Where ρ_{BNCD} is the resistivity of BNCD. For the total resistance, this gives,

$$R_{tot} = \frac{R_{sh}^{Au}\left(b^2R_{sh}^{BNCD} + bdR_{sh}^{Au} - b^2R_{sh}^{BNCD} - bdR_{sh}^{BNCD}\right)}{d\left(bR_{sh}^{BNCD} + dR_{sh}^{Au} - bR_{sh}^{Au}\right)}$$

The total sheet resistance in the transparent electrode can be obtained from the total resistance of the unit cell by:

$$R_{tot} = \rho_{tot} \frac{b}{bh} = R_{sh,tot} = \frac{R_{sh}^{Au}\left(b^2R_{sh}^{BNCD} + bdR_{sh}^{Au} - b^2R_{sh}^{BNCD} - bdR_{sh}^{BNCD}\right)}{d\left(bR_{sh}^{BNCD} + dR_{sh}^{Au} - bR_{sh}^{Au}\right)}$$

Here b is the length and the broadness of the transparent electrode. This leads to an expression for the total sheet resistance as:

$$R_{sh,tot} = \frac{R_{sh}^{Au}\left(b^2R_{sh}^{BNCD} + bdR_{sh}^{Au} - b^2R_{sh}^{BNCD} - bdR_{sh}^{BNCD}\right)}{d\left(bR_{sh}^{BNCD} + dR_{sh}^{Au} - bR_{sh}^{Au}\right)}$$

In this work, the sheet resistance is determined by the use of a four probe measurement, known as a Van der Pauw-, or 4 point probe procedure. In this procedure, 4 probes are put at distance S from each other. Then a constant current is injected through 2 electrodes and the potential difference is measured

between the two others. Due to this arrangement, the sheet resistance is independent of the contact resistance between the tips and the layer under investigation.

One can assume that a constant current $2i$ flows away from its originating contact with a radial symmetry into infinity. The volume in which the current flows is given by hA where h is the thickness of the layer and A the radial area. The current density at a position r can thus be provided by:

$$J = \frac{2i}{2\pi rh} = \frac{i}{\pi rh}$$

The electrical field strength can be determined by Ohm's law

$$U = RI = \rho \frac{L}{A} I$$

$$\frac{U}{L} = \rho \frac{I}{A} = \rho J = E$$

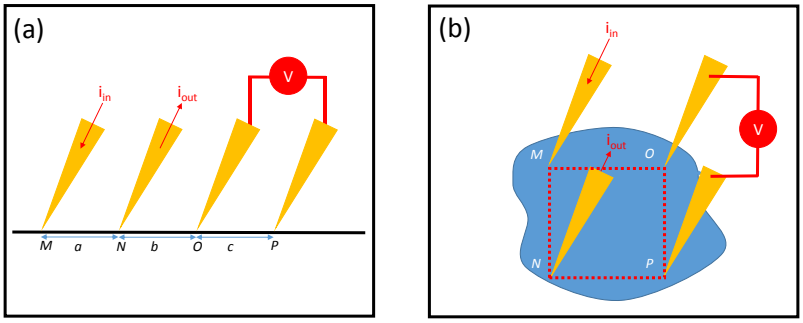

Figure 1-III: Schematic representation of (a) linear and (b) squared 4-probe measurement setup.

The principle of 4-point measurements is based on the determination of the potential differences at two points on the surface (on positions O and P on a distance c from each other) when current is supplied to the system on a third point (on position M on a distance of a+b from O and a+b+c from P) and the current is extracted from the system on a fourth point (N on distance b from O and b+c from P) (Figure 1-III (a)) [16].

When current is added to the system in M, and no current is extracted and the voltage difference is measured between O and P, the voltage difference between the points is given by:

$$V_{M,OP} = V_P - V_O = \int_P^O E dr = \int_P^O \rho \frac{i}{\pi rh} dr = \rho \frac{i}{\pi h} \int_P^O \frac{1}{r} dr = \rho \frac{i}{\pi h} \left[ln(a+b) - ln(a+b+c) \right] = -\rho \frac{i}{\pi h} \left[ln\left(\frac{a+b+c}{a+b} \right) \right]$$

When current is added from the system in point N, the potential difference will change to:

$$V_{N,OP} = V_P - V_O = \int_P^O E dr = \int_P^O \rho \frac{i}{\pi r h} dr = \rho \frac{i}{\pi h} \int_P^O \frac{1}{r} dr = \rho \frac{i}{\pi h} \left[In(b) - In(b+c) \right] = -\rho \frac{i}{\pi h} \left[In\left(\frac{b+c}{b} \right) \right]$$

The resistance that is measured between points O and P in the system when the current is added at point M and extracted from point N is equal to:

$$R_{MN,OP} = \frac{V_{M,OP} - V_{N,OP}}{i} = -\frac{\rho}{\pi h} \left[In\left(\frac{a+b+c}{a+b} \right) - In\left(\frac{b+c}{b} \right) \right] = -\frac{\rho}{\pi h} In\left(\frac{(a+b+c)b}{(a+b)(b+c)} \right)$$

Similarly, the voltage difference can be determined between M and P, while the current is added to the system in point N and extracted from point O, giving the following relations

When current is added from point N, the potential difference between M and P is given by

$$V_{N,MP} = V_P - V_M = \rho \frac{i}{\pi h} \int_P^M \frac{1}{r} dr = \rho \frac{i}{\pi h} \left[In(b+c) - In(a) \right] = -\rho \frac{i}{\pi h} \left[In\left(\frac{a}{b+c} \right) \right]$$

When current is added from point O, the potential difference between M and P is given by

$$V_{O,MP} = V_P - V_M = \rho \frac{i}{\pi h} \int_P^M \frac{1}{r} dr = \rho \frac{i}{\pi h} \left[In(c) - In(a+b) \right] = -\rho \frac{i}{\pi h} \left[In\left(\frac{a+b}{c} \right) \right]$$

The resistance that is measured in the system between point M and P when the current is added at point N and extracted from point O is equal to:

$$R_{NO,MP} = \frac{V_{N,MP} - V_{O,MP}}{i} = -\frac{\rho}{\pi h} \left[In\left(\frac{a}{b+c} \right) - In\left(\frac{a+b}{c} \right) \right] = -\frac{\rho}{\pi h} In\left(\frac{ac}{(b+c)(a+b)} \right)$$

The two resistance equations can be transformed towards the distance parameters as follows:

$$\frac{(a+b+c)b}{(a+b)(b+c)} = exp\left(-R_{MN,OP} \frac{\pi h}{\rho} \right)$$

And

$$\frac{ac}{(b+c)(a+b)} = exp\left(-R_{NO,MP} \frac{\pi h}{\rho} \right)$$

Summing the last two equations leads to:

$$1 = exp\left(-R_{MN,OP} \frac{\pi h}{\rho} \right) + exp\left(-R_{NO,MP} \frac{\pi h}{\rho} \right)$$

In order to extract the resistivity of the system one and $R_{NO,MP} = R_{MN,OP}$, the resistivity and sheet resistance are determined as follows:

$$1 = exp\left(-R_{MN,OP}\frac{\pi h}{\rho}\right) + exp\left(-R_{MN,OP}\frac{\pi h}{\rho}\right) = 2\,exp\left(-R_{MN,OP}\frac{\pi h}{\rho}\right)$$

$$\rho = \frac{-R_{MN,OP}\pi h}{In(0.5)} = \frac{R_{MN,OP}\pi h}{In(2)}$$

If the probe positions are not linear or symmetrical, this expression is not true and an adapted form should be used where:

$$\frac{In(2)}{f} = \frac{\left(\frac{R_{MN,OP} + R_{NO,MP}}{2}\right)\pi h}{\rho}$$

With f as a correction factor. Also R_f can be defined as:

$$R_f = \frac{R_{MN,OP}}{R_{NO,MP}}$$

f can be expressed in function of R_f as

$$cosh\left(\left(\frac{R_f - 1}{R_f + 1}\right)\frac{In(2)}{f}\right) = \frac{1}{2}\frac{In(2)}{f}$$

An iterative method can be used in order to calculate f in function of R_f by importing different results for R_f and solving the equation for f. In our self-made system, a built-in function is present, that calculates this f value and calculates the corrected sheet resistance for the film.

During the measurements, the sheet resistance is measured 10 times and an averaged value is used as effective sheet resistance.

1.2.3. JV-characterization

JV-characterization was performed by the use of a keithley 2400 multimeter. Solar cells were swept between -0.5 V up to 1.5 V in order to obtain the information necessary to extract the solar cell parameters. Illumination of solar cell devices was performed by a solar simulator Newport Oriel class A, equipped with a Xenon Short Arc lamp with 150 W power (1 sun at 1.5 air mass density, *i.e.* 100 mW/cm^2). Neutral density filters were used in order to regulate the light intensity, and with it the short circuit current during the JV-sweep.

The general solar cell expression, as described in the introduction is described by:

$$J = -J_{sc} + J_0\left(\exp\left(\frac{e(V - IR_s)}{n_{ideal}kT}\right) - 1\right) - \frac{(V - IR_s)}{R_{sc}}$$

Where R_{sc} and R_s are the shortcut or short circuit resistance and series resistance respectively, n_{ideal} is the ideality factor, J_o the dark saturation factor and J_{sc} the short circuit current. kT is the thermal energy, consisting out of the product of the Boltzmann factor k and the absolute temperature T.

At voltages below 0 V and voltages above 1 V, the effects of drift related parasitic short circuit resistances (V<0 V) and series resistance (V>1 V) start becoming more important compared to the other factors which are mainly determined in the diffusion region of the JV-curve. In these regions the JV-curves are quasi linear. The resistance is obtained from the slopes in these quasi-linear regions as $\left(slope = 1/R_{parasitic}\right)$.

From the light intensity dependent JV-curves, the light intensity dependency of the parasitic resistances can be obtained. Furthermore, information about the ideality factor and dark saturation current can be acquired from the light dependency of the open circuit voltage in the diffusion region. Information about bimolecular recombination and space charge limited photocurrents can be obtained from the light power dependency of the short circuit current. These objects are further discussed in the introduction chapter of this thesis.

1.2.4. Mobility measurements using Field Effect Transistors

Transistor measurements allow us to extract mobility values for negative electrons and positive holes in organic semiconductors and their blends.

In field effect transistors, two distinct voltages can be applied: The source gate voltage and the source drain voltage. The sign of the applied source gate voltage can regulate selectively the density of electrons or holes in the doped silicon layer near the insulating SiO_2 layer. Due to capacitive effects, a channel of countercharge carriers will form in the active organic material. The higher the source-gate voltage the more charge carriers are attracted in the channel and the higher the charge density.

On the other hand a source drain voltage can be used to regulate the drift velocity of the charge carriers in the channel. The drift velocity has two distinct definitions. For one thing, it can be used as a measure of the transport velocity and it is dependent on the time that charge carriers would need in order to be transported through the channel with a length L, with L defined as the space between source and drain. For another, the drift velocity is also a measure for the mobility of a charge when it is present in an electrical field. The electrical field that is influencing the charge is defined as $E = V_{DS}/L$.

The current flowing through the channel can be expressed as the charge density flowing through the channel per unit time. The charge density is determined by

the number of charge carriers, and the volume of the channel determined by the length L between source and drain, and the channel width W. The transition time is again the time needed in order to cross the channel as described in the previous paragraph.

$$I_{SD} = \frac{\rho \frac{W}{L}}{t_{tr}} = \rho \frac{W}{L} \frac{L}{v} = \rho \frac{W}{\mu E} = \rho \frac{WL}{\mu V_{DS}}$$

The charge carrier density is determined from the capacitance of the layer, defined as the charge density of a layer at a certain applied voltage. An important property of semiconductors is that a threshold voltage V_T should be overcome in order to generate transportable charge carriers, and should thus be taken into account in the determination of the charge carrier density. The capacitance can thus be written as:

$$C = \frac{\rho}{V_{SG} - V_T}$$

and the charge carrier density as

$$\rho = C(V_{SG} - V_T)$$

The expression of the source drain current can be transformed to:

$$I_{SD} = \frac{C(V_{SG} - V_T)WL}{\mu V_{SD}}$$

Here, μ is the mobility of the majority charge carrier in the organic channel material.

The substrates used in this work consisted out of a highly doped n-type silicon substrate. On top of the doped silicon substrate, an insulating SiO_2 layer at the surface giving a base capacitance per unit area of 16.9 nF/cm^2. Gold source and drain electrodes were deposited on top of the insulating SiO_2 layer with a spacing of 30 µm and a length of 10 mm. In order to investigate the mobility effects of the active layer of the P3HT:PCBM reference devices and P3HT:PCBM:Graphene devices, these layers were deposited on top of the substrates under the same processing conditions as was done for the solar cell devices described in the graphene based solar cell section.

1.2.5. Fourier Transform Photocurrent Spectroscopy (FTPS)

Fourier transform photocurrent spectroscopy is a highly sensitive opto-electronic spectral technique used to determine the optical properties of materials which are occurring below the bandgap of materials. It is intensively used to study the effects of defect states in inorganic materials, but recently also sub-bandgap properties of organic materials are studied by this technique.

The general principle is to use a Fourier-transform infrared spectrometer with an external beam exit as beam source system, and an operational solar cell as external detector. The signal recorded by the solar cell is amplified by a current to voltage amplifier and coupled back to the interferometer. The system uses a fast Fourier transform algorithm to convert the amplified signal of the solar cell from the time domain into the spectral domain. The comparison between a measurement with the solar cell as detector and a measurement with a reference detector reveals the spectral sensitivity of the solar cell. A detailed description of the process is given in the thesis of Vandewal et al [17].

The FTPS- setup in this work was based on a Thermo Electron Nicolet 8700 FTIR with an external detector system of Thermo-fisher and a Stanford Research System low-noise current pre-amplifier. The processing and analysis software used in this work was OPUS, which was provided with the FTIR-spectrometer system. The light source used in this work was a halogen lamp, which is called the near-infrared source by the software. It provided white light from which the range between 27000 and 2800 cm^{-1} was used during the experiments. The measurements where performed using a quartz beam splitter, since the region of interest is mainly located in the visual and near infrared part of the electromagnetic spectrum. In order to enhance the color sensitivity of the measurements, color filters were used.

Although the Fourier transformation is a fast way in order to determine the spectral response of a material, the response is influenced by the mirror speed in the interferometer. Mirror speed correction of the signal can be obtained using spectra measured at different mirror speeds. The signal can be related to the mirror speed by:

$$f = 2v\sigma$$

Here f is the frequency, v the mirror speed, and σ the photocurrent signal. For a fixed signal $\sigma = \sigma_1$, a frequency response can be obtained multiplied by a constant $a(\sigma_1)$ in n points where n is the number of different mirror speeds used to characterize the spectrum.

This can be done for m wavenumbers or energies, each giving the modulation frequency response in n points. The shape of the frequency response over the whole spectral region can be obtained by matching the frequency response curves in their overlapping frequency region.

Once the frequency response is known, the modulation independent spectral response can be obtained by [17]:

$$a(\sigma) = \frac{d_{pc}(\sigma, f)}{b(f)}$$

References

[1] S. Günes, H. Neugebauer, and N. S. Sariciftci, "Conjugated Polymer-Based Organic Solar Cells," *Chem. Rev.*, vol. 107, no. 4, pp. 1324–1338, Apr. 2007.

[2] "Datasheet Dichlorobenzene." http://pubchem.ncbi.nlm.nih.gov/compound/1_2-dichlorobenzene#section=Top

[3] Y. Hernandez, V. Nicolosi, M. Lotya, F. M. Blighe, Z. Sun, S. De, I. T. McGovern, B. Holland M. Byrne, Y. K. Gun'Ko, J. J. Boland P. Niraj, G. Duesberg, S. Krishnamurthy, R. Goodhue, J. Hutchison, V. Scardaci, A. C. Ferrari, and J. N. Coleman, "High-yield production of graphene by liquid-phase exfoliation of graphite," *Nat. Nanotechnol.*, vol. 3, no. 9, pp. 563–568, Sep. 2008.

[4] F. Bonaccorso, A. Lombardo, T. Hasan, Z. Sun, L. Colombo, and A. C. Ferrari, "Production and processing of graphene and 2d crystals," *Mater. Today*, vol. 15, no. 12, pp. 564–589, Dec. 2012.

[5] T. Hasan, F. Torrisi, Z. Sun, D. Popa, V. Nicolosi, G. Privitera, F. Bonaccorso, and a. C. Ferrari, "Solution-phase exfoliation of graphite for ultrafast photonics," *Phys. Status Solidi Basic Res.*, vol. 247, pp. 2953–2957, 2010.

[6] F. Torrisi, T. Hasan, W. Wu, Z. Sun, A. Lombardo, T. S. Kulmala, G.-W. Hsieh, S. Jung, F. Bonaccorso, P. J. Paul, D. Chu, and A. C. Ferrari, "Inkjet-Printed Graphene Electronics," *{ACS} Nano*, vol. 6, no. 4, pp. 2992–3006, Apr. 2012.

[7] O. M. Maragó, F. Bonaccorso, R. Saija, G. Privitera, P. G. Gucciardi, M. A. Iatì, G. Calogero, P. H. Jones, F. Borghese, P. Denti, V. Nicolosi, and A. C. Ferrari, "Brownian Motion of Graphene," *{ACS} Nano*, vol. 4, no. 12, pp. 7515–7523, Dec. 2010.

[8] E. F. Schubert, "Light Emitting Diodes History of LEDs."

[9] "Light-Emitting Diodes: E. Fred Schubert: 9780521865388: Amazon.com: Books.".

[10] M. Ma, F. W. Mont, X. Yan, J. Cho, E. F. Schubert, G. B. Kim, and C. Sone, "Effects of the refractive index of the encapsulant on the light-extraction efficiency of light-emitting diodes.," *Opt. Express*, vol. 19 Suppl 5, no. S5, pp. A1135–40, Sep. 2011.

[11] "Principles of Optics: Electromagnetic Theory of Propagation, Interference and Diffraction of Light: Max Born, Emil Wolf, A. B. Bhatia, P. C. Clemmow, D. Gabor, A. R. Stokes, A. M. Taylor, P. A. Wayman, W. L. Wilcock: 9780521642224: Amazon.com: Books.".

[12] W. L. W. Born Max, Wolf Emil, A. B. Bhatia, P. C. Clemmow, D. Gabor, A. R. Stokes, A. M. Taylor, P. A. Wayman, "Principles of Optics: Electromagnetic Theory of Propagation, Interference and Diffraction of Light: : 9780521642224: Amazon.com: Books.".

[13] "Spectroscopic Ellipsometry and Reflectometry: A User's Guide: Harland G. Tompkins, William A. McGahan: 9780471181729: Amazon.com: Books.".

[14] Z. Remes, R. Vasudevan, K. Jarolimek, A. H. M. Smets, and M. Zeman, "The Optical Spectra of a-Si:H and a-SiC:H Thin Films Measured by the Absolute Photothermal Deflection Spectroscopy (PDS)," in *Solid State Phenomena*, 2014, vol. 213, pp. 19–28.

[15] D. Ritter and K. Weiser, "Suppression of interference fringes in absorption measurements on thin films," *Opt. Commun.*, vol. 57, no. 5, pp. 336–338, Apr. 1986.

[16] L. J. van der Pauw, "A method of measuring the resistivity and Hall coefficient on lamellae of arbitrary shape," *Philips Tech. Rev.*, vol. 20, pp. 220–224, 1958.

[17] K. Vandewal, "Doctoraatsproefschrift 2009 | Faculteit Wetenschappen," 2009.